Jet Formation and Eddy Tilts in Barotropic Geostrophic Turbulence

A thesis submitted to the School of Mathematics at the University of East Anglia in partial fulfilment of the requirements for the degree of Doctor of Philosophy

Natasha Senior

Oct 2019

University of East Anglia

Abstract

Turbulent two-dimensional fluids support an inverse cascade of energy, in which eddies transfer energy to successively larger scales. Systems experiencing differential rotation also admit a class of plane-wave solutions called Rossby waves. The excitation of Rossby waves leads to an anisotropisation of the energy cascade such that most of the turbulent energy is funnelled towards zonal modes. This manifests as alternating zonal jets with meridional widths that scale according to the Rhines scale. It is this phenomenon that is thought to be the origin of spontaneous jet formation that has been observed in many systems of geophysical interest, such as the World Ocean and Jovian atmospheres. In this thesis, we study jets using a barotropic channel model on the β-plane. Jets are known to be supported by the divergence of Reynolds stresses in the underlying eddy fields. This relationship can be visualised using the geometric eddy ellipse formulation, in which the average direction of momentum flux is given by the tilt angle of these ellipses. This formulation is introduced by studying the interaction of shear instabilities with a barotropically unstable jet profile. We demonstrate how, in more turbulent systems, we can filter the flow fields to recover ellipse patterns of the most dominant modes. We then study jet formation in β-plane turbulence from physical and spectral perspectives and show that these may be unified by finding the location an energy front in wavenumber space and studying how it propagates. Then, using the geometric eddy ellipse formulation, we show how the underlying eddy field is arranged by the anisotropisation process. We find that there are strong momentum fluxes at low-wavenumber, occupying the most energetic scales. These mask a regular underlying pattern of momentum fluxes at intermediate scales that correlate with the jet structure. To reveal this structure we develop a formulation for evaluating two-point correlations in which the energy spectrum is expanded on a series of angular Fourier modes. We show that the zeroth and second angular modes contain all of the eddy ellipse information. In particular, we find that the tilt angle can be recovered from the quotient of the real and imaginary parts of the second mode.

Contents

Acknowledgements

The conception of this thesis has followed a labyrinthian learning curve and I would like to thank my supervisors for helping me navigate it. Hayder Salman for helping me strive to do my best, David Stevens for always encouraging and Xiaoming Zhai for always inspiring. I would like to thank NERC and the EnvEast DTP for supporting this research and members of the wider research community whose work this thesis draws from, in particular Talia Tamarin for the helpful discussions. I am also grateful to Vanessa Miemietz for their support during the final push.

This thesis would never have materialised without the support from my community. Thanks to Nathan Hutton for their enduring encouragement, to whom I am forever indebted; my parents who championed me along the way; my sister for believing that I am "the pinnacle of everything" and Annie Hutton, whose kindness will never be forgotten. I thank all my siblings in arms who were on this journey with me: David Pascall for sharing the frustrations; the maths PGRs, old and new, who have made the office a pleasant place to be, in particular Julia Docampo whose post-work pub trips are sorely missed. I thank honorary housemate Phil Lamb for championing the hours I sunk into playing Mass Effect, Claire Armstrong for subsequently confiscating it and Daisy Orme with whom I would share my morning inertia. I thank those who stepped up during the hard times: Jodie Cullum for always checking in and getting me out the house; Jessie Gardner for all the words (and actions) of encouragement; Kris Sales for going the extra mile to make sure I am okay; my cosmic twin Sara Skarp for navigating the multiverse and finding me; David Litchfield for the Buddhist teachings and Alberto Villois, for believing in me, inspiring me and dragging me over the finish line. And finally, Clifford, my furry feline housemate, for always greeting me with cuddles after the long difficult days. I thank the random acts of kindness, the tough life lessons, the good and the bad and every nudge, murmur and fluctuation that brings this chapter to a close and opens up a new one.

Dedications

For the sensitive souls still on their PhD journeys: just keep going.

1

Introduction

1.1 Motivation

The majority of fluid motions in the Earth's oceans and atmosphere exhibit turbulence, a flow regime characterised by a high Reynolds number, in which inertial forces dominate over viscous forces. Turbulent fluids are a rich tapestry of churning eddies that exist across many spatial and temporal scales. Constantly evolving under strongly non-linear dynamics, these eddies do not just coexist with larger scale coherent flows, such as the world's major ocean currents, but readily interact with them. One of the most turbulent regions of the Earth's ocean is found in the latitude of the Drake Passage. There are no continental barriers in this region, allowing for the presence of the most important current in the global ocean conveyor belt: the Antarctic Circumpolar Current (ACC) (Thompson, 2008). Encircling the Earth and connecting three ocean basins, the ACC serves as an important juncture where the world's oceans meet and exchange heat, salinity and other key tracers. The ACC is driven by strong westerlies and travels clockwise around Antarctica transporting phenomenal volumes of water, around 130×10^6 m^{3}s^{-1}, in the zonal (east-west) direction (Rintoul and Garabato, 2013). In the meridional (north-south) direction however, the mechanisms by which water may be transported are severely constrained. In basin currents, meridional transport in the ocean's interior is facilitated by geostrophic flow, a flow regime which arises when an approximate balance is struck between the Coriolis force and the pressure gradient force. However this picture is very different for the ACC where significant geostrophic balance cannot be achieved for the meridional currents since the zonal pressure gradients must integrate to zero in the latitudes of the Drake Passage. Instead, lateral transport is achieved primarily through eddies which are generated by the strong baroclinic instability processes that exist in the region (Rintoul, 2018). Though the extent to which this facilitates transport is poorly understood due to limited data on the vertical structure of these eddies (Marshall et al., 2006).

One way to address this gap in data is to approach the problem numerically.

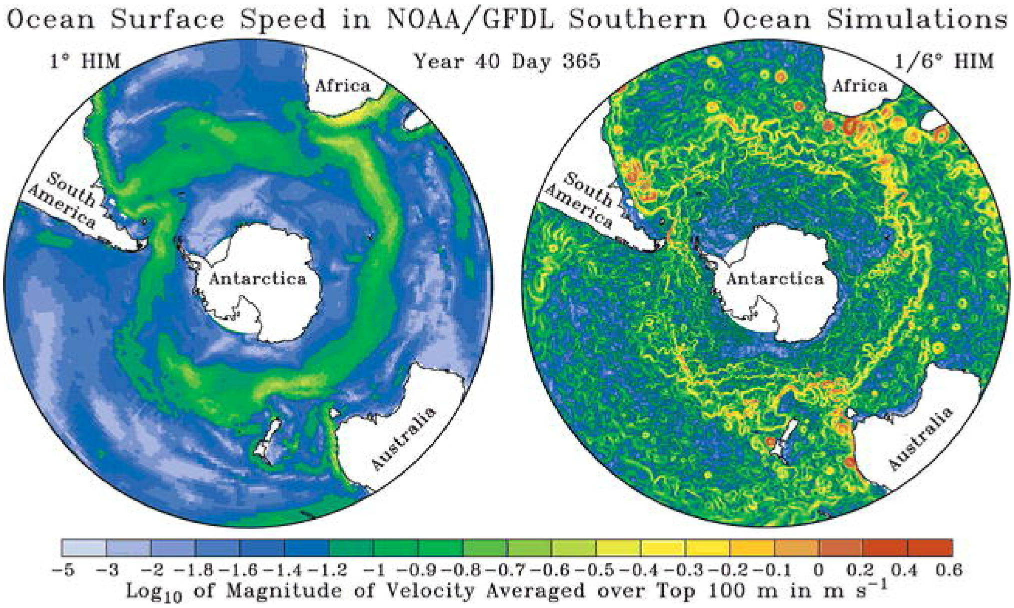

Figure 1.1.1: Two snapshots of the Southern Ocean surface speed from the MESO project, comparing coarse resolution and fine resolution (eddy-permitting) runs. The overall structure of the ACC in each plot is similar but at eddy-permitting resolutions, the flow is composed of eddies and fine zonal structures. Figure adapted from Hallberg and Gnanadesikan (2006)

Figure 1.1.1 compares model outputs from the Modelling Eddies in the Southern Ocean (MESO) project, of surface speeds of the Southern Ocean from a coarse resolution run and a fine resolution, eddy-permitting run (Hallberg and Gnanadesikan, 2006). The coarse resolution model shows the general circumpolar structure of the ACC, where as the high resolution model runs reveals fine filamentary structures, zonal jets and eddies associated with highly turbulent dynamics. Since mesoscale eddies are not currently resolvable in global ocean and climate models, they require a faithful parameterisation, in which their effect on the larger-scale processes are accounted for. The Gent-McWilliams scheme (Gent and Mcwilliams, 1990) was developed to represent the important vertical eddy momentum fluxes which drive net transport across the ACC and is now a staple of current global ocean and climate models. However, there has been less success in finding a suitable parameterisation for horizontal momentum fluxes (see Marshall et al. (2012) and Eden (2010) for some recent attempts). The impact on the climate system of horizontal eddy momentum fluxes is less pronounced then the vertical counterpart, but such a parameterisation would include effect of the inverse cascade, a phenomenon in which eddies not only interact with large-scale structures, but are responsible for their very existence.

The inverse energy cascade of Kraichnan (1967) and Batchelor (1969) is exhibited by highly turbulent systems in which the dynamics are two-dimensional, which is a fitting approximation for many systems of geophysical interest such as mesoscale oceanic processes. In these systems, eddies transfer energy successively upscale. Eddies which occupy the largest scales are also the longest lived and so coherent structures dominate these scales. When this system is subject to strong rotation, the flow is approximately geostrophic and exhibits geostrophic turbulence. These systems admit a class of plane-wave solutions called Rossby waves. Rhines (1975) theorised that the interaction between Rossby waves and turbulence would result in eddies elongating zonally. The manifesting coherent structures corresponding to these eddies are zonal banded structures, alternating east and west, known as zonal jets. These jets will be the focus of this thesis.

Spontaneous zonal jet formation is observed all over the world's oceans (Maximenko et al., 2005; Treguier et al., 2003; Treguier and Panetta, 1994) and is often attributed to geostrophic turbulence. This theory is further motivated by outputs from eddy-resolving ocean general circulation models, in which spontaneous zonal jet formation is observed (Nakano and Hasumi, 2005). The signature banded patterns of the Solar System's gas giants may also be attributed to geostrophic turbulence (Williams, 1978). Indeed, satellite altimetry data has revealed the inverse cascading process in the South Pacific Ocean (Scott and Wang, 2005) and recent analysis of data from Cassini's Jupiter flyby demonstrate the existence of geostrophic turbulence in the Jovian atmosphere (Choi and Showman, 2011; Galperin et al., 2014).

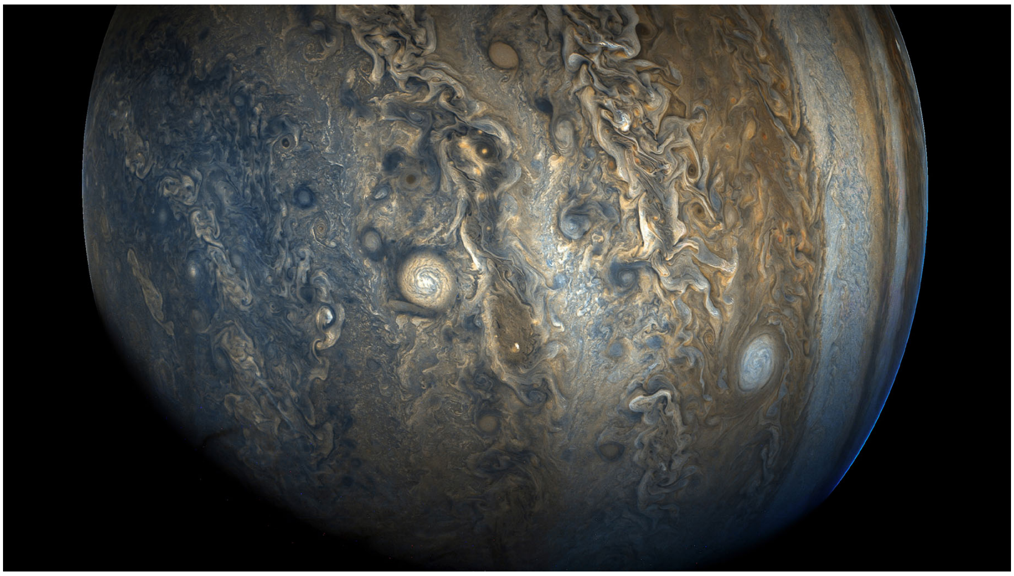

Figure 1.1.2: Jupiter's Southern Hemisphere captured by NASA's Juno space probe on its ninth close flyby. Jupiter's signature bands are composed of a rich pattern of swirling eddies and zonal jets (NASA et al., 2017).

Though there is no obvious demarcation between the underyling eddy fields and the coherent structures they develop into, it is useful to examine how eddies interact with the mean flow. A simple method of examining this interaction is to separate the dynamical equations into their mean components and departures there-from, this is the residual-mean approach. If flows reach a steady state, these so-called Reynolds averaged equations (Reynolds, 1895) demonstrate a balance between the regions of converging eddy momentum fluxes and the mean flow structures they support (Starr, 1968). Recent efforts to parameterise horizontal momentum fluxes have followed the residual-mean approach by describing eddy fluxes of potential vorticity as a divergence of the eddy stress tensor (Marshall et al., 2012). One way to visualise momentum fluxes is to cast eddy velocity correlations as an ellipse (Preisendorfer, 1988). The magnitude and tilt of the these ellipses provide information about strength and direction of the momentum fluxes of the underlying eddy field. This approach has been used to study eddy-mean flow interactions in western boundary jets (Waterman and Hoskins, 2013) and barotropically unstable jets (Tamarin et al., 2016). The broad aim of this thesis will be to apply the geometric eddy ellipse formulation to jet formation in geostrophic turbulence.

1.2 Theory of Geostrophic Turbulence

1.2.1 The Two-Dimensional Ocean

Many flows of geophysical significance have large horizontal scales L compared to their vertical scales D. For example, the wind-driven gyres have depths of $D \sim 1000$ m but can extend over many thousands of kilometres $L \sim 1 \times 10^3$ km parallel to the ocean's surface. So they have a large aspect ratio characterised by

$$L \gg D. \tag{1.2.1}$$

We introduce the continuity equation for incompressible fluids in which the density is a constant given by ρ_0. In this limit, the continuity equation is given by

$$\frac{\partial u}{\partial x} + \frac{\partial v}{\partial y} = -\frac{\partial w}{\partial z}, \tag{1.2.2}$$

where (u, v, w) are the fluid velocity components in the x (east-west), y (north-south) and z (vertical) directions respectively. Examining the size of the terms in this equation we see that they scale as

$$\frac{U}{L}, \quad \frac{U}{L}, \quad \frac{W}{D}, \tag{1.2.3}$$

where U and W are typical horizontal and vertical velocities respectively. If we assumed that the first two terms were small compared to the last, this would imply that $w =$ constant everywhere through the vertical extent of the fluid. However, this is not a realistic scenario since lateral transport must supply this fluid at the ocean floor or surface, for example, so the first two terms would not be negligible. If all three terms are equally significant then

$$W \sim \frac{D}{L} U, \tag{1.2.4}$$

and by Eq. (1.2.1) we find that

$$W \ll U, \tag{1.2.5}$$

and vertical advection may be neglected in the dynamical equations. We also can assume that the pressure gradient forces and gravity are dominant forces that balance each other in the vertical acceleration equations such that the fluid is in hydrostatic balance. Another important scaling consideration for flows on the surface of a rotating sphere are for those that experience rapid rotation. These are characterised by the Rossby number given by

$$R_o = \frac{U}{Lf} \ll 1, \tag{1.2.6}$$

where

$$f = 2\omega \sin \theta_R \tag{1.2.7}$$

is the Coriolis parameter. This is the component of Earth's rotation vector felt by a fluid parcel on its surface at some latitude θ_R. Here ω is the Earth's rotation rate. On the Earth $f \sim 10^{-4}$ s^{-1} to an order of magnitude. The Rossby number is a ratio comparing the magnitude of inertial forces and Coriolis force. In this thesis we consider timescales of a few months to a few years; this gives $R_o \ll 1$. To leading order, the assumption of a large aspect ratio gives Eq. (1.2.5), hydrostatic balance and strong rotation given by Eq. (1.2.6) reduces the steady frictionless Navier-Stokes equations in a rotating frame of reference to

$$\frac{\partial p}{\partial x} = \rho_0 f v, \tag{1.2.8a}$$
$$\frac{\partial p}{\partial y} = -\rho_0 f u, \tag{1.2.8b}$$
$$\frac{\partial p}{\partial z} = -\rho_0 g, \tag{1.2.8c}$$

where p is the pressure and g is the acceleration due to gravity. The first two equations given by Eq. (1.2.8a) and Eq. (1.2.8a) demonstrate a balance between the pressure gradient and the Coriolis force: this is geostrophic flow where the fluid travels along lines of constant pressure. The last equation is the hydrostatic balance, in which the weight of the fluid balances its vertical pressure. Taking ∂_z of either Eq. (1.2.8a) or Eq. (1.2.8b) leads us to conclude that

$$\frac{\partial v}{\partial z} = \frac{\partial u}{\partial z} = 0, \tag{1.2.9}$$

That is, if fluids are hydrostatic and geostrophic, the horizontal velocities are independent of z. Note that Eq. (1.2.9) is a limiting case of thermal wind balance where we have assumed that the density is constant. This is the Taylor-Proudman theorem (Proudman and Lamb, 1916; Taylor, 1923) in which motions are confined to the horizontal plane under rapid rotation and flows move as vertical columns. In this thesis we will consider the dynamics of flows that are hydrostatic and are close to geostrophic.

Flows that are hydrostatic but not necessarily geostrophic are governed by the shallow water equations which will be discussed in detail in §2. Importantly, these equations conserve the potential vorticity following the fluid motion:

$$\frac{Dq}{Dt} = 0, \tag{1.2.10}$$

where the potential vorticity (PV) is given by

$$q = \frac{\zeta + f}{h}. \tag{1.2.11}$$

Here the relative vorticity is $\zeta = (\partial_x v - \partial_y u)$ and h is the fluid depth. We have also introduced the horizontal material derivative

$$\frac{D}{Dt} \equiv \frac{\partial}{\partial t} + \mathbf{u} \cdot \boldsymbol{\nabla}. \tag{1.2.12}$$

where the horizontal velocity vector is $\mathbf{u} \equiv (u, v)$ and the horizontal gradient operator is $\boldsymbol{\nabla} \equiv (\partial_x, \partial_y)$. Conservation of q is none other than a statement that fluid columns conserve their mass and their angular momentum. Consider a fluid column moving east such that f is constant, if the topography is such that the fluid column depth h increases then the fluid column will have to increase ζ to obey Eq. (1.2.10). Consider now a vortex moving in an anti-clockwise sense in the northern hemisphere, in a cyclonic flow and fluid columns flowing in this vortex. At the east of the vortex, fluid columns flow northward and f increases. If h is constant, then these fluid columns must have $\zeta < 0$. At the west of the vortex, fluid columns flow southward and f decreases so the fluid column must have $\zeta > 0$. This leads to the vortex propagating to the west. This is the mechanism by which

Rossby waves propagate where the planetary vorticity f acts a restoring force.

In the nearly geostrophic limit of the shallow water regime, conservation of PV reduces to the quasi-geostrophic equation. This is an equation in a single dependent variable $\psi(x, y, t)$, the geostrophic streamfunction:

$$\frac{\partial q}{\partial t} + J(\psi, q) = 0 \tag{1.2.13}$$

where the non-linear terms are written as a Jacobian

$$J(A, B) = \frac{\partial A}{\partial x}\frac{\partial B}{\partial y} - \frac{\partial B}{\partial x}\frac{\partial A}{\partial y} \tag{1.2.14}$$

and the quasi-geostrophic potential vorticity q is given by

$$q \equiv \nabla^2\psi + f - \frac{\psi}{L_D^2} + f_0\frac{H_0 - H}{H_0}, \tag{1.2.15}$$

where $f = f_0 + \beta y$ is the Coriolis parameter approximated for a small variation in θ_R under the β-plane approximation where f_0 and $\beta = \partial_y f$ are evaluated at a particular latitude. Here we have introduced the external Rossby deformation radius

$$L_D \equiv \frac{\sqrt{gH_0}}{f_0} \tag{1.2.16}$$

and the last term gives the fractional change in the total depth where the depth is given by $H = H(x, y)$ and the average depth is H_0.

1.2.2 Two-Dimensional Turbulence

We have seen that flows with large aspect ratios experiencing rapid rotation follow approximately two-dimensional dynamics. It is easy then to be convinced that turbulent flows within these systems share more similarities with two-dimensional turbulent theory than that of its three-dimensional counterpart. The quasi-geostrophic equation Eq. (1.2.13) takes its simplest form when flow scales are small compared to the radius of deformation such that $L \ll L_D$, the bottom topography is smooth such that $H = H_0$ and the Coriolis parameter is constant. Under these assumptions Eq. (1.2.13) reduces to

$$\frac{\partial}{\partial t}\nabla^2\psi + J\left(\psi, \nabla^2\psi\right) = 0. \tag{1.2.17}$$

Here we have recovered the two-dimensional vorticity equation underpinning two-dimensional turbulent theory. Two-dimensional turbulence is itself a fascinating phenomenon with the development of its theory accredited to Kraichnan (1967) and Batchelor (1969). In the absence of vortex stretching and tilting—central mechanisms for evolving three-dimensional turbulent flows (Kolmogorov, 1941)—two-dimensional turbulence exhibits exotic traits that cannot be visualised as simple projections of the full three-dimensional theory. A more complete overview of two-dimensional turbulence may be found in Boffetta and Ecke (2012), but here our discussion will be limited to some of the interesting features of the phenomenon. We will omit the full statistical treatment—whilst acknowledging its necessity—and content ourselves with some intuitive arguments gleaned from conservation laws.

Like its inviscid unforced three-dimensional counterpart, the two-dimensional vorticity equation conserves energy:

$$\frac{dE_m}{dt} = \frac{d}{dt}\frac{1}{2}\iint_{\Omega} \left(\boldsymbol{\nabla}\psi \cdot \boldsymbol{\nabla}\psi\right)\, dx\, dy = 0, \tag{1.2.18}$$

where the kinetic energy is given by E_m and Ω is a doubly periodic domain where $(x, y) \in \Omega$. Another important flow invariant of two-dimensional flows, which is absent in three-dimensional flows, is a quantity called the enstrophy, $\mathcal{Z} \equiv \frac{1}{2}\left(\nabla^2\psi\right)^2$. The total enstrophy is conserved:

$$\frac{d\mathcal{Z}_\zeta}{dt} = \frac{1}{2}\iint_{\Omega} \left(\nabla^2\psi\right)^2\, dx\, dy = 0, \tag{1.2.19}$$

where $\mathcal{Z}_\zeta$ is the total enstrophy. The total energy and total enstrophy may be written as the zeroth and second moments of the energy spectrum $E(k)$,

$$E_m = \int_0^\infty E(k)dk, \tag{1.2.20a}$$

$$\mathcal{Z}_\zeta = \int_0^\infty k^2 E(k)dk, \tag{1.2.20b}$$

where $E(k)$ is the energy contained at a specific scale k. Following arguments presented in Salmon (1998b), if energy is provided through a scale-specific forcing mechanism then it would initially be concentrated at some wavenumber $k = k_f$. We expect that after some time, the energy would spread out to adjacent wavenumbers through localised non-linear interactions. During this process, both Eq. (1.2.20a) and Eq. (1.2.20b) must be conserved. If (say) the energy has now spread to two wavenumbers, one smaller and one larger, $k_1 = \frac{k_f}{2}$ and $k_2 = 2k_f$, then by conservation of energy and enstrophy

$$E(k_1) + E(k_2) = E(k_f), \tag{1.2.21a}$$

$$\left(\frac{k_f}{2}\right)^2 E(k_1) + (2k_f)^2 E(k_2) = k_f^2 E(k_f). \tag{1.2.21b}$$

This gives $E(k_1) = \frac{4}{5}E(k_f)$ and $E(k_2) = \frac{1}{5}E(k_f)$ and the smaller wavenumber receives most of the energy. On the other hand, the enstrophy at the smaller wavenumber is $\mathcal{Z}_\zeta(k_1) = \frac{1}{5}\mathcal{Z}_\zeta(k_f)$, so the enstrophy is transported in the opposite direction. This simple demonstration shows how these conservation laws favour energy transfer towards larger scales and simultaneously, favours enstrophy transfers to smaller scales.

If the flow is continuously forced with constant energy injection rate ϵ and enstrophy injection rate ξ at wavenumber k_f, dissipated at a small scale near some high wavenumber k_D and energy is sharply removed at the largest scale k_0, then the two-dimensional system can reach statistical equilibrium. When this happens the flow will support two inertial ranges in which the dynamics are governed entirely by non-linear interactions and do not feel the forcing and dissipation mechanisms. If we first consider the inertial range that lies between the forcing scale k_f and dissipation scale k_D, if there are a sufficiently large number of cascade steps then we can assume that the energy spectrum $E(k)$ depends only on ϵ and ξ. However, as $k_D \to \infty$, $\epsilon \to 0$ since energy is preferentially cascaded in the opposite direction and so the spectrum $E(k)$ depends only on k and ξ. The only form of $E(k)$ that is dimensionally consistent with this is given by

$$E(k) = C_\xi \xi^{\frac{2}{3}} k^{-3}, \tag{1.2.22}$$

where C_ξ is a universal dimensionless constant. This is known as the direct enstrophy cascade. The second inertial range is between k_f and k_0. If there is some large scale dissipation term removing energy from the system as $k \to k_0$ and there are a sufficiently large number of cascade steps, then the spectrum will depend on k and ϵ only. Then dimensional analysis shows that

$$E(k) = C_K \epsilon^{\frac{2}{3}} k^{-\frac{5}{3}}, \tag{1.2.23}$$

where C_K is the dimensionaless Kolmogorov constant. This is the inverse energy cascade that travels upscale, in stark contrast to the direct energy cascade of three-dimensional turbulence, in which energy follows a $k^{-5/3}$ scaling towards dissipation scales. So we can see that the energy will cascade in the direction $k < k_f$ according to $E(k) \propto k^{-5/3}$ and enstrophy will cascade in the direction $k > k_f$ according to $E(k) \propto k^{-3}$ (Batchelor, 1969; Kraichnan, 1967). A notable consequence of the inverse energy cascade is that if the domain is bounded, then in the absence of large scale dissipation, energy will condense at the largest allowable scale k_0 (Kraichnan, 1967). Note that the power law for the enstrophy cascade is steep which caused Kraichnan (1971) to suggest that this may violate the assumption that eddies only interact with eddies of similar scale and so they introduced a log-corrected power-law. However, whilst its realm of applicability is questioned, this k^{-3} has been observed in fully developed turbulence e.g. Brachet et al. (1988) and most authors will agree that there must be a steep power law of some sort governing the enstrophy cascade so the form presented here is generally accepted (Davidson, 2004). A k^{-3} spectrum has also been observed in the atmosphere though it is not clear if this can be attributed to two-dimensional turbulent phenomena (Nastrom and Gage, 1983).

Here we have discussed the two-dimensional vorticity equation given by Eq. (1.2.17) as a simplification of the quasi-geostrophic equation. In the unsimplified quasi-geostrophic equations given by Eq. (1.2.13), these scaling laws are applicable if we consider that the total potential enstrophy:

$$\mathcal{Z}_q = \frac{1}{2} \iint_\Omega q^2 \, dx \, dy, \tag{1.2.24}$$

is conserved instead of the total enstropy in Eq. (1.2.19). Charney (1971), based on proofs presented by Fjørtoft (1953), was the first to demonstrate the isomorphism between the two equations. However, this is not to say that two-dimensional and quasi-geostrophic turbulent fluids will always exhibit identical behaviours. Specifically, when we include the β-plane in Eq. (1.2.17), accounting for the effect of differential rotation, we permit Rossby waves. It is this effect that distinguishes turbulence in nearly geostrophic systems from its two-dimensional origins.

1.2.3 Rhines (1975) Theory

Here we discuss some of the main ideas presented by Rhines (1975) who identified a new phenomenon that arises as a consequence of Rossby wave excitation in a turbulent quasi-geostrophic flow. Assuming flat bottom topography and that $L \ll L_D$, Eq. (1.2.13) simplifies to the barotropic vorticity equation:

$$\frac{\partial}{\partial t} \nabla^2 \psi + J\left(\psi, \nabla^2 \psi\right) + \beta \frac{\partial \psi}{\partial x} = 0, \tag{1.2.25}$$

which will be the equation this thesis will focus on. We see that varying f according to the β-plane approximation, produces an extra linear term when compared to the two-dimensional vorticity equation Eq. (1.2.17). This introduces wave-like characteristics to the fluid in which the β-plane acts as the restoring force. Following e.g. Salmon (1998a), we consider the linear limit of Eq. (1.2.25). Scale analysis gives the β-Rossby number

$$R_\beta = \frac{U}{\beta L^2}. \tag{1.2.26}$$

When $R_\beta \ll 1$, we expect rotational effects to dominate over inertial ones. In this limit, the flow only exhibits small departures from rest and the non-linear terms in Eq. (1.2.25) are negligible. This results in the linearised equation,

$$\frac{\partial}{\partial t}\nabla^2\psi + \beta\frac{\partial\psi}{\partial x} = 0. \tag{1.2.27}$$

Plane-wave solutions of Eq. (1.2.27) are of the form

$$\psi(x, y, t) = A \exp i \left\{\mathbf{k}\cdot\mathbf{x} - \omega_R t\right\}, \tag{1.2.28}$$

where A is some coefficient, $\mathbf{k}$ is the wavevector and ω_R is the frequency of the wave. Substituting Eq. (1.2.28) into Eq. (1.2.27) gives the Rossby wave dispersion relation

$$\omega_R = -\frac{\beta\mathbf{k}\cdot\hat{\mathbf{i}}}{k^2}, \tag{1.2.29}$$

where $k = |\mathbf{k}| = \sqrt{k_x^2 + k_y^2}$ in which k_x and k_y are the zonal and meridional wavenumbers and, $\hat{\mathbf{i}}$ is the zonal unit vector. Now if we consider a system where energy is provided to the fluid at a small scale then, as we have argued, eddies will preferentially transfer this energy to larger scales. They will do so with a turnover frequency ω_T given by

$$\omega_T \approx Uk, \tag{1.2.30}$$

where U is the characteristic flow speed of eddies occupying scale k. In practice, U is taken to be the root mean square of the flow U_{rms}. As the flow progresses, characteristic scales become larger and the turnover frequency becomes smaller. When the turnover frequency is sufficiently small, Rossby waves become excited. If we assume $\omega_R = \beta/2k$ for Rossby waves with average orientation and equate the turbulent frequency to the Rossby wave frequency $\omega_T = \omega_R$ we obtain the Rhines scale:

$$k_R \equiv \sqrt{\frac{\beta}{2U}}. \tag{1.2.31}$$

This represents the largest possible scale to which energy can be carried before it is used to propagate Rossby waves. Eddies transfer energy and enstrophy between these scales through through stretching and shearing of vorticity. However, once the Rossby wave regime is approached, energy within these regions of vorticity are radiated away before significant distortion can occur and individual fluid parcels begin to oscillate around latitude lines. This results in the flow favouring zonal motion. Since the cascade to larger scales must still be obeyed, the transfer of energy between eddies of different scale becomes anisotropic and the flow favours zonally elongated structures. These zonally elongated structures are jets with spacing given by Eq. (1.2.31). Since meridional velocities would reduce to slight perturbations, Rhines argued that these jets were likely to represent a stable state as dictated by the Rayleigh-Kuo stability criterion where, for stability the quantity

$$\beta - \frac{\partial^2 U}{\partial y^2} \tag{1.2.32}$$

should not change sign anywhere in the domain. They argued that since the β-plane acts to stabilise the zonal structures, the jets' meridional spacing will not grow beyond the Rhines scale. This is often described as the "arrest" of the inverse cascade by the β-plane. The argument of Rhines (1975) was only discussed in terms of a freely evolving system, whereas the two-dimensional turbulent cascade theories we have introduced are based on forced-damped systems that reach a statistically stationary state. Maltrud and Vallis (1991) considered such systems, defining the turbulent turnover frequency in terms of the energy injection rate

$$\omega_t = \epsilon^{\frac{1}{3}} k^{-\frac{2}{3}} \tag{1.2.33}$$

to obtain an another characteristic scale

$$k_\beta = \left(\frac{\beta^3}{\epsilon}\right)^{\frac{1}{5}}. \tag{1.2.34}$$

which at the time, they reasoned was simply the continuously forced analogue of Eq. (1.2.31). However, later studies e.g. Sukoriansky et al. (2007) have found that both Eq. (1.2.31) and Eq. (1.2.34) have different roles to play in the theory of jet formation, which we will examine in detail in §5. Depending on how the turbulent frequency is defined, other characteristic scales corresponding to the onset of Rossby wave propagation have been obtained in the literature. For example, Holloway and Hendershott (1977) preferred to set $\omega_T = \zeta_{\rm rms}$ to obtain a scale $k = \beta/\zeta_{\rm rms}$ where $\zeta_{\rm rms}$ is the root mean square of ζ. Unlike Eq. (1.2.34) which considers a continuously forced system, this is simply an alternative version of Eq. (1.2.31).

The spectrum predicted by theories in geostrophic turbulence was initially thought to follow the two inertial ranges of two-dimensional turbulence which reach a peak at scales k_β. This is depicted in Fig. 1.2.1. The $k^{-5/3}$ scaling was observed by Maltrud and Vallis (1991) and in numerous other studies. However the k^{-3} law corresponding to the direct enstrophy cascade has always been elusive. Part of the reason the k^{-3} slope was thought to be difficult to observe was because long lived isolated structures act to steepen the slope, a topic that has garnered significant interest in the past (McWilliams, 1984). Maltrud and Vallis (1991) found that even weak β-planes stifle the formation of these

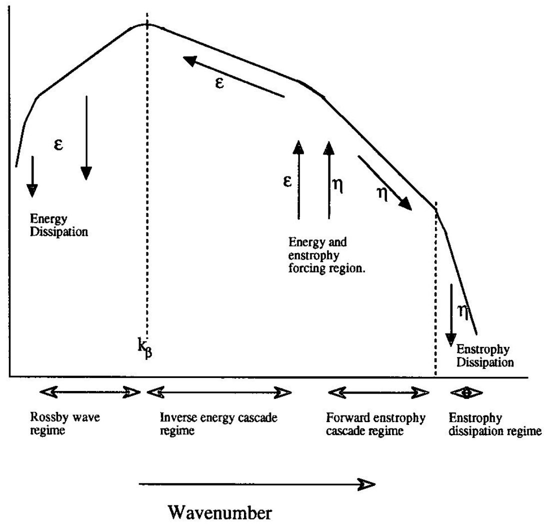

Figure 1.2.1: An idealised spectrum of the dual cascade exhibited by geostrophic turbulent flows. Here ϵ and η are the rates of energy and enstrophy transfer respectively. The spectrum shows the inertial ranges predicted by two-dimensional turbulent theory, the $k^{-\frac{5}{3}}$ slope where $k < k_f$ and the k^{-3} slope for $k > k_f$. When the flow reaches k_β, which at the time was associated the cascade arrest, the spectrum departs from its purely two-dimensional analogue and drops for lower wavenumbers as the cascade is inhibited. Figure adapted from Vallis and Maltrud (1993).

long-lived structures. The enstrophy cascade was still found to be steeper than k^{-3}, but shallower than cases where $\beta = 0$. Vallis and Maltrud (1993) found that the anisotropisation of energy transfer between scales revealed a "dumbbell" shape in the energy spectra which is depicted in Fig. 1.2.2. We see that as energy initially concentrated on a ring in wavenumber space where the energy is injected and later is funnelled towards zonal modes resulting in the appearance of a lobe or "dumbbell" structure. The anisotropisation process leads to another, less discussed power-law applicable to geostrophic turbulence given by

$$E_\beta(k) = C_\beta \beta^2 k^{-5}, \tag{1.2.35}$$

where there is a rapid increase of energy with scale (Rhines, 1975). In this thesis, we will refer to this as the Rhines spectrum with Rhines constant C_β. This is found dimensionally by considering that at the largest scales, the energy spectrum should be dominated by Rossby-wave mechanisms (introduced by the β-plane) and the scale k only (Chekhlov et al., 1996). We are tempted to think of this as another inertial range which results from geostrophic turbulence when flows approach $k = k_R$. Rhines cast doubt on this interpretation. Firstly, because the steepness of slope was at odds with the assumption that interactions between eddies

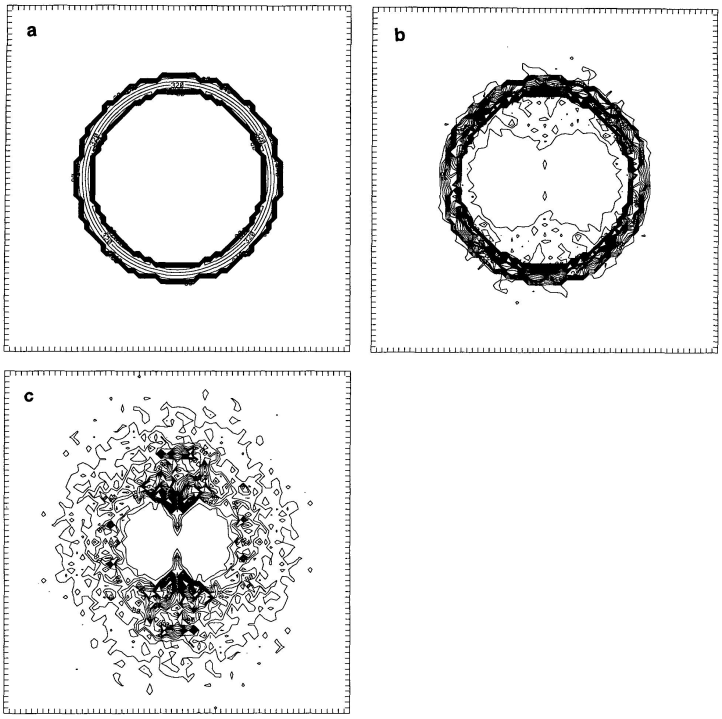

Figure 1.2.2: The spread of spectral energy $E(k_x, k_y)$ of freely evolving β-plane turbulence. Here, the axes are k_x and k_y, the zonal and meridional wavevectors respectively, with the origin at the centre of the plots. Wavevectors initially concentrated at some high wavenumber cascade anisotropically towards $k = 0$ resulting in the dumbbell shape in the energy spectrum (Vallis and Maltrud, 1993).

of different scales, must be local. Secondly, though this power law is dimensionally consistent, it would need to apply to all scales, including those much smaller than k_R, in which Rossby wave dynamics are thought to be absent. The first objection is easy to overcome, since the problem of non-locality also applies to the steep power law of the enstrophy cascade which, despite some controversy, is generally accepted. The second objection can be addressed by considering the anisotropy of the energy spectrum. We can see from Fig. 1.2.2 that as energy is funnelled towards zonal modes, energy concentrates along the k_y-axis which is consistent with a steep power-law developing there.

The first numerical study to reveal the existence of the k^{-5} slope in the energy spectrum was conducted by Chekhlov et al. (1996) whilst studying scales $k < k_R$, using a forced-dissipative doubly periodic model. They observed that spectral evolution slowed down significantly with the introduction of the β-plane and spectral anisotropy developed quickly. When they isolated each spectral axes, they found that modes near $k_y = 0$ scaled as $k^{-\frac{5}{3}}$ but modes near $k_x = 0$ scaled as k^{-5}, the law predicted by Rhines (1975) [see Eq. (1.2.35)]. In fact, all other modes away from $k_x = 0$ seemed to follow the traditional Kolmogorov-like scaling law given by Eq. (1.2.23) albeit with the reduced constant. There are several striking implications bought about by this study. First, this scaling law is found at $k_x = 0$, which is the only region in the energy spectrum where the Rossby wave dispersion relation given by Eq. (1.2.29) has no component, yet $k_x = 0$ seems to be the only region in which the β-term explicitly enters the spectral evolution. This is a consequence of the strong non-linearity of the flow. Secondly, Chekhlov et al. (1996) found that energy transfer does not cease for any direction, nor is the cascade arrested, but k_β defined by Eq. (1.2.34) marks the point at which the spectrum begins to anisotropise.

These ideas have been reinforced by Huang et al. (2001), who studied β-plane turbulence in spherical geometry. They argued that the k^{-5} slope is inherent to formation of jets and that k_β does not represent any inhibition to the transfer of energy to small scales. They reasoned that the "dumbbell" shapes observed in previous simulations were transient features that resulted from the anisotropy, which reduced in size as flows progress. Furthermore, they suggested that zonal modes should eventually merge together according to the k^{-5} scaling law along the meridional wavenumber axis and the scale should eventually reach the largest possible mode allowed by the domain.

Collating results from further studies (Galperin et al., 2006, 2001; Sukoriansky et al., 2002), Sukoriansky et al. (2007) drew a distinction between Rhines' wavenumber Eq. (1.2.31) and that derived in Maltrud and Vallis (1991) given by Eq. (1.2.34). As discussed by Chekhlov et al. (1996), the latter marked the position in wavespace where the spectral slope steepens towards the Rhines spectrum given by Eq. (1.2.35). The former was the position of a time-dependent moving energy front that lies at the peak of the Rhines spectrum as the flow develops. Whilst Eq. (1.2.34) is a static feature provided the forcing is constant, the Rhines scale can penetrate to the small scales in the absence of large-scale dissipation. Sukoriansky et al. (2007) argued that between these two characteristic scales lies a new flow regime called "zonostrophic turbulence". It is in this flow regime, they argued, that jets are found. Sukoriansky et al. (2002) found that spectra of gas giants agree with the steep power law given by Eq. (5.4.1) and data from the Cassini mission even suggests that Jupiter supports this regime (Galperin et al., 2014). In this thesis we will examine these characteristic scales in detail.

1.2.4 Jets

Jet formation in geostrophic turbulence is distinct from many other types of jet formation in fluid dynamics because rather than relying on external injections of momentum, these jets are in-built into the dynamics of the system (Rhines, 1994). Motivated by the fact that Rhines' jets bore striking similarities to the characteristic band structures in Jupiter's atmosphere and those in other Jovian planets, Williams (1978) was the first to confirm their appearance in numerical simulations of free-decaying turbulence on a sphere. Strong jets alternating east and west were observed for parameters applicable to both terrestrial and Jovian atmospheres. Subsequent studies using two-dimensional stochastically forced fluids have generally followed the methodology presented in this work e.g. Nadiga (2006).

There have been a range of numerical studies investigating jet formation in different geometries. For instance Nadiga and Straub (2010) investigated jet formation in gyres and how they are affected by small and large scale forcing terms. There have also been barotropic models in closed basins e.g. Berloff (2005); Kramer et al. (2006). The full quasigeostrophic equations themselves have not been extensively used to investigate jet dynamics. For instance Scott and Dritschel (2013) investigated how the energy of jets becomes partitioned in flow regimes where $L \sim L_D$.

Layered quasi-geostrophic models have been developed to study geostrophic turbulence most notably in Panetta (1993); Salmon (1980); Treguier and Panetta (1994) and later Berloff et al. (2009a,b); Thompson and Young (2007). These experiments have sought to investigate the more realistic scenario where the fluid consists of stratified layers. These models are then able incorporate the underlying baroclinic instability process which produces small-scale forcing in oceans, and is the source of turbulent eddies in the ACC and jet evolution is altered by the presence of baroclinic modes.

Once jets have formed, they develop into persistent and stable structures with bands of fluid alternating in direction of propagation, east and west. Owing to stabilising property of the β-plane in Eq. (1.2.32), eastward jets tend to be sharper and more energetic than westward jets where the latter must remain broad for the mean flow to remain stable. Dritschel and McIntyre (2008) understood this in terms of the PV invertibility principle where, in the quasi-geostrophic equations given by Eq. (1.2.13), q may be inverted to recover the velocity components and so the shape of the PV profiles and velocity profiles are related. They argued that sharp eastward jet components should coincide with strong PV gradients and broad westward jets with weak potential vorticity gradients. In the extreme case, PV gradients might weaken so much that there may be large meridional regions where q is homogenised. These alternating regions of steep gradients and PV homogenisation result in a pattern known as a "PV-staircase". The accompanying zonal velocity profiles for ideal PV-staircases are shown in Fig. 1.2.3. To explain this process of PV-homogenisation, Dritschel and McIntyre (2008) argued that PV gradients act as the Rossby wave restoring force. PV gradients are strong

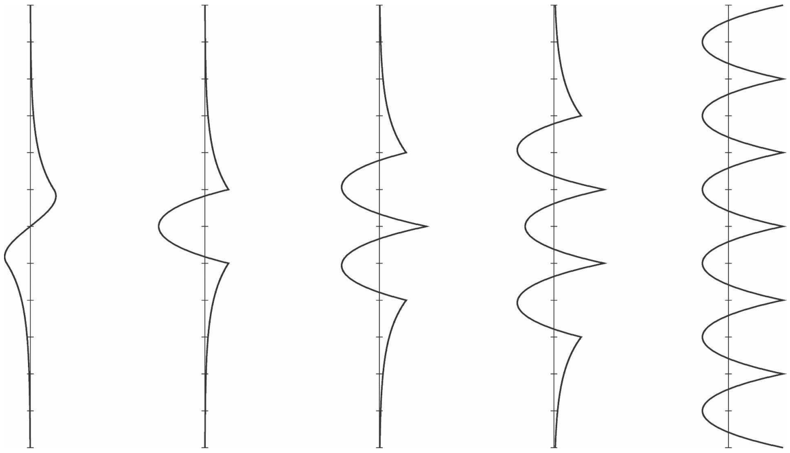

Figure 1.2.3: Zonally averaged velocity profiles corresponding to the ideal PV-staircase. The first two profiles are for one step, then two and three steps in the staircase. The last profile corresponds to part of a region where there are an infinite number of steps. Figure adapted from (Dritschel and McIntyre, 2008).

between adjacent mixed regions and weak within them. This creates a positive feedback effect where, between mixed regions, restoring forces become stronger, which steepens potential vorticity gradients and in turn weakens PV gradients in the mixed region, where restoring forces become weaker. Building on these ideas, Farrell and Ioannou (2009) sought a more formal statistical approach to explain the structure and stability of these jets.

Jets that develop spontaneously in geostrophic turbulence are meridionally inhomogeneous structures. In §4 we will discuss how we may apply Reynolds averaging (Reynolds, 1895) to decompose the shallow water momentum equations in terms of their zonal mean and fluctuating components, denoted by an overline and prime respectively. For doubly periodic and zonally periodic, meridionally bounded domains we may obtain the relationship

$$\overline{u} \propto -\frac{\partial \overline{u'v'}}{\partial y} \tag{1.2.36}$$

for a statistically stationary state, where the overline denotes a zonal average and the primes denote a departure therefrom. Here, the fluctuating components may be interpreted as any sort of transient motion, such as Rossby waves or eddies. From this relationship we see that steady zonal jets must be maintained by regions of momentum flux convergence and divergence (Starr, 1968). How this actually arises, or more specifically, how these fluxes are arranged by the anisotropisation process is not clear in the literature. The few works that have studied the inhomogeneity that develops in geostrophic turbulence have examined these eddy-mean flow interactions (Huang and Robinson, 1998; Shepherd, 1987a,b). Since the underlying eddy field involves many scales interacting non-linearly, it is not informative to describe these instabilities simply as departures from the zonal mean. These studies seeking to analyse eddy-mean flow interactions employed a stationary-transient decomposition to distinguish between persisting structures and transient features following the methodology of McWilliams (1984). These studies inferred that transient eddies near the Rhines scale were not responsible for maintaining the jet structure and instead intermediate-scale eddies provided the momentum flux pattern that gave rise to the relationship Eq. (1.2.36). In this thesis we will study jet formation and the eddy-mean flow relation given by Eq. (1.2.36) but will instead adopt a geometric approach for describing the momentum fluxes and identifying the scales responsible for supporting the jet structure. The averaged primed quantity in Eq. (1.2.36) is an eddy velocity correlation which we refer to as the shear stress. This together with other eddy velocity correlations in the Reynolds averaged equations are the Reynolds stresses. As we will discuss in §4, we may fit an ellipse to the Reynolds stresses Preisendorfer (1988). The geometric properties of such ellipses provide information about the direction and magnitude of the momentum fluxes and are a convenient tool for examining how momentum fluxes are arranged. This formulation was used by Tamarin et al. (2016) to study the interaction between shear instabilities and a barotropically unstable jet, in which eddies strengthening the mean-flow were associated with ellipses that tilted towards the jet and a weakening jet was associated with eddies tilting away from the jet. These variance ellipses have also been calculated for western boundary jets in Waterman and Hoskins (2013) and Waterman and Lilly (2015). In this thesis we will examine how eddy variance ellipses tilt to flux momentum towards jets that form spontaneously in geostrophic turbulence.

1.3 Thesis Outline

The broad aim of the work presented in this thesis is to examine the formation of zonal jets under β-plane turbulence, identify the characteristic scales following Sukoriansky et al. (2007) and to understand how stresses in the Reynolds averaged equations are arranged by the anisotropisation process in the energy spectra.

In §2 we will derive the quasi-geostrophic equation from the Navier-Stokes equations. We will then develop a mathematical model for the barotropic vorticity equation on a laterally bounded channel and discuss how two different sets of commonly employed boundary conditions affect conservation laws. In §3 we will present the numerical implementation of the barotropic channel model.

We will introduce the Reynolds averaged equations and the geometric eddy ellipse formulation in §4. We will discuss how this formulation may be used to examine eddy-mean flow interactions in zonal jets following analysis presented in Tamarin et al. (2016) for shear instabilities on a barotropically unstable zonal jet.

We will present results of continuously forced and forced dissipative turbulence in a barotropic channel model in §5. We will examine jet formation in geostrophic turbulence from a number of different complimentary perspectives. We will examine the scaling laws discussed in Sukoriansky et al. (2007) and identify some characteristic scales associated with the anisotropisation process. We will then apply the geometric eddy ellipse formulation, developed in §4 and discuss its limitations.

In §6 we will seek to connect the anisotropisation process in the energy spectra to the inhomogeneous Reynolds stress quantities in the geometric eddy ellipse formulation. We will do so by revisiting arguments from homogeoenous two-dimensional isotropic turbulence presented in Batchelor (1953) and generalise these for inhomogeneous anisotropic two-dimensional turbulence. We will then present some results from this new formulation.

2

Mathematical Model

2.1 Governing Equations

2.1.1 The Primitive Equations

We begin by deriving the primitive equations that are often used in geophysical fluid dynamics, from the Navier Stokes equations. We will go through the assumptions which lead to the shallow water equations and will derive the quasi-geostrophic equation given in Eq. (1.2.13). We will simplify this further to develop a barotropic channel model that is consistent with the shallow water equations; this will form the basis of our numerical studies.

In the absence of forcing and dissipation, the Navier-Stokes equations are given by

$$\frac{\partial \mathbf{v}}{\partial t} + \left(\mathbf{v} \cdot \boldsymbol{\nabla}^{\text{3D}}\right) \mathbf{v} = -\frac{1}{\rho} \boldsymbol{\nabla}^{\text{3D}} p + \boldsymbol{\nabla}^{\text{3D}} \phi_0, \tag{2.1.1}$$

where the 3D velocity vector is given by

$$\mathbf{v} \equiv (u, v, w) \tag{2.1.2}$$

and the 3D gradient operator is given by

$$\boldsymbol{\nabla}^{\text{3D}} \equiv \left(\frac{\partial}{\partial x}, \frac{\partial}{\partial y}, \frac{\partial}{\partial z} \right). \tag{2.1.3}$$

Here, ρ is the density of the fluid and the scalar fields p and ϕ_0 are respectively the pressure and the potential corresponding to a conservative body force (e.g. gravity). The Navier Stokes equations apply to fluids within inertial frames of reference. In geophysical problems, fluid motions occur within a rotating frame of reference. This requires us to perform a coordinate transformation.

Following e.g. Pedlosky (1987a), consider an inertial frame of reference I with a Cartesian coordinate system and basis vectors $\hat{\mathbf{i}}_I, \hat{\mathbf{j}}_I$ and $\hat{\mathbf{k}}_I$. Now consider another rotating frame of reference R with a Cartesian coordinate system and basis vectors $\hat{\mathbf{i}}_R, \hat{\mathbf{j}}_R$ and $\hat{\mathbf{k}}_R$. The origins of I and R are aligned and frame R rotates with angular velocity $\boldsymbol{\omega}$ with respect to I such that $\hat{\mathbf{k}}_I, \hat{\mathbf{k}}_R$ and $\boldsymbol{\omega}$ are parallel. The position vector $\mathbf{r}$ of an arbitrary fluid parcel may be written as

$$\mathbf{r} = x_I \hat{\mathbf{i}}_I + y_I \hat{\mathbf{j}}_I + z_I \hat{\mathbf{k}}_I = x_R \hat{\mathbf{i}}_R + y_R \hat{\mathbf{j}}_R + z_R \hat{\mathbf{k}}_R. \tag{2.1.4}$$

The form of spatial gradients and the gradient operator Eq. (2.1.3), in the rotating frame is left unchanged i.e.

$$\boldsymbol{\nabla}_R^{\mathrm{3D}} \equiv \left(\frac{\partial}{\partial x_R}, \frac{\partial}{\partial y_R}, \frac{\partial}{\partial z_R} \right). \tag{2.1.5}$$

If we now consider an arbitrary vector $\mathbf{A}$ in frame R. An observer in an inertial frame I will observe the rate of change of $\mathbf{A}$ with time to be

$$\left[\frac{d\mathbf{A}}{dt} \right]_I = \left[\frac{d\mathbf{A}}{dt} \right]_R + \boldsymbol{\omega} \times \mathbf{A}. \tag{2.1.6}$$

Using Eq. (2.1.6) we find an observer in frame I will observe the fluid velocity in frame R to be

$$\mathbf{v}_I = \mathbf{v}_R + \boldsymbol{\omega} \times \mathbf{r}, \tag{2.1.7}$$

where $\mathbf{v}_I$ is the velocity observed in the inertial frame of reference and $\mathbf{v}_R$ is the relative velocity observed in the rotating frame of reference. The rate of change in time of the fluid velocity is given by

$$\left[\frac{d\mathbf{v}_I}{dt} \right]_I = \left[\frac{d\mathbf{v}_I}{dt} \right]_R + \boldsymbol{\omega} \times \mathbf{v}_I. \tag{2.1.8}$$

We substitute Eq. (2.1.7) into Eq. (2.1.8) to obtain

$$\left[\frac{d\mathbf{v}_I}{dt} \right]_I = \left[\frac{d\mathbf{v}_R}{dt} \right]_R + 2\boldsymbol{\omega} \times \mathbf{v}_R + \boldsymbol{\omega} \times (\boldsymbol{\omega} \times \mathbf{r}) + \frac{d\boldsymbol{\omega}}{dt} \times \mathbf{r}. \tag{2.1.9}$$

So the difference between the acceleration observed in the inertial frame of reference and that in the rotating frame of reference is given by three fictitious accelerations. The first is the Coriois acceleration

$$2\boldsymbol{\omega} \times \mathbf{v}_R, \tag{2.1.10}$$

the second is the centrifugal acceleration

$$\boldsymbol{\omega} \times (\boldsymbol{\omega} \times \mathbf{r}) \tag{2.1.11}$$

and the third is due variations in $\boldsymbol{\omega}$ which is unimportant for most oceanographic and atmospheric purposes so we can assume $d\boldsymbol{\omega}/dt = 0$. The centrifugal acceleration may be rewritten as

$$\boldsymbol{\omega} \times (\boldsymbol{\omega} \times \mathbf{r}) = -\omega^2 \mathbf{r}_\perp = -\boldsymbol{\nabla}^{3D} \left(\omega^2 |\mathbf{r}_\perp|^2\right) = -\boldsymbol{\nabla}^{3D} \phi_c, \tag{2.1.12}$$

where $\mathbf{r}_\perp$ is the component of $\mathbf{r}$ that perpendicular to $\boldsymbol{\omega}$ and $\omega = |\boldsymbol{\omega}|$. In the last equality we have written the centrifugal acceleration in terms of a potential

$$\phi_c \equiv \frac{1}{2}\omega^2 |\mathbf{r}_\perp|^2. \tag{2.1.13}$$

We may combine this with the conservative body potential in Eq. (2.1.1) to obtain the geopotential:

$$\Phi_g = \phi_0 + \phi_c. \tag{2.1.14}$$

The geopotential surface that coincides with the surface of the Earth's ocean if it were at rest is known as the geoid.

Consider now a Cartesian coordinate system attached to the geoid where the xy-plane lies tangent to its surface such that x-direction points East, the y-direction points North and the z-direction points up. These have basis vectors $\hat{\mathbf{i}}$, $\hat{\mathbf{j}}$ and $\hat{\mathbf{k}}$ respectively. The latitude θ_R is measured between the direction perpendicular to the Earth's rotation vector and the z-direction. If we assume the geoid is approximately spherical, the Earth's rotation vector will be

$$\boldsymbol{\omega} = (0, \omega \cos\theta_R, \omega \sin\theta_R) \tag{2.1.15}$$

and, since $\hat{\mathbf{k}}$ is perpendicular to the geoid

$$\Phi_g \approx gz \tag{2.1.16}$$

where g is the acceleration due to gravity. So Eq. (2.1.1) observed in a frame of reference on the surface of the Earth's ocean at some latitude θ_R in a Cartesian coordinate system is given by

$$\frac{\partial \mathbf{v}}{\partial t} + \left(\mathbf{v} \cdot \boldsymbol{\nabla}^{3D}\right)\mathbf{v} - 2\boldsymbol{\omega} \times \mathbf{v} = -\frac{1}{\rho}\boldsymbol{\nabla}^{3D} p - g\hat{\mathbf{k}} \tag{2.1.17}$$

In the traditional approximation the y-component of Eq. (2.1.15) is neglected as it is considered dynamically insignificant. Introducing the Coriolis parameter

$$f \equiv 2\omega \sin\theta_R, \tag{2.1.18}$$

we obtain the primitive equations given by

$$\frac{\partial \mathbf{v}}{\partial t} + \left(\mathbf{v} \cdot \boldsymbol{\nabla}^{\scriptscriptstyle 3D}\right) \mathbf{v} - f\hat{\mathbf{k}} \times \mathbf{v} = -\frac{1}{\rho} \boldsymbol{\nabla}^{\scriptscriptstyle 3D} p - g\hat{\mathbf{k}}, \tag{2.1.19}$$

used widely in geophysical fluid dynamics.

In some circumstances it is appropriate to use the f-plane approximation in which Eq. (2.1.18) does not vary across the Cartesian grid system. For our purposes, we assume a small variation and let $\theta_R = \theta_R(y)$. Expanding f in a Taylor series about $y = 0$ gives:

$$f \approx f_0 + \beta y. \tag{2.1.20}$$

where $f_0 = 2\omega \sin \theta_R(0)$ and $\beta = 2\omega \cos \theta_R(0)$. This is a simple way for us to introduce differential rotation—important for the mesoscale processes we will be studying—without introducing extra non-linearity into the quasi-geostrophic equations.

Continuity of mass completes the description of our fluid which is given by

$$\frac{\partial \rho}{\partial t} + \boldsymbol{\nabla}^{\scriptscriptstyle 3D} \cdot (\rho \mathbf{v}) = 0. \tag{2.1.21}$$

We will simplify this by assuming our fluid has a constant density $\rho = \rho_0$. The continuity equation reduces to the incompressibility condition given by

$$\boldsymbol{\nabla}^{\scriptscriptstyle 3D} \cdot \mathbf{v} = 0. \tag{2.1.22}$$

2.1.2 The Shallow Water Equations

The shallow water equations are derived on the assumption that

$$\frac{D}{L} \ll 1 \tag{2.1.23}$$

i.e. horizontal scales L are large compared with vertical scales D. We have seen in §1 that this allows us to neglect the vertical component of acceleration in Eq. (2.1.19). The resulting flow will be in hydrostatic balance:

$$\frac{\partial p}{\partial z} = -\rho_0 g. \tag{2.1.24}$$

Having removed the vertical component of acceleration, it is useful to depth-integrate the hydrostatic relation between a free surface $z = \eta(x, y, t)$, such that η coincides with $z = 0$ when the fluid is at rest, and an arbitrary point

(x, y, z) in the fluid interior

$$p(x, y, z, t) = \rho_0 g \{\eta(x, y, t) - z\}. \tag{2.1.25}$$

Substituting this into the horizontal component of Eq. (2.1.19) and Eq. (2.1.21) the equations of motion become

$$\frac{D\mathbf{u}}{Dt} + \mathbf{f}_\mathrm{h} = -g\boldsymbol{\nabla}\eta \tag{2.1.26a}$$

$$\boldsymbol{\nabla} \cdot \mathbf{u} = -\frac{\partial w}{\partial z}. \tag{2.1.26b}$$

Here, we have defined the horizontal velocity vector,

$$\mathbf{u} \equiv (u, v) \tag{2.1.27}$$

the horizontal gradient operator

$$\boldsymbol{\nabla} \equiv \left(\frac{\partial}{\partial x}, \frac{\partial}{\partial y}\right). \tag{2.1.28}$$

the horizontal material derivative

$$\frac{D}{Dt} \equiv \frac{\partial}{\partial t} + \mathbf{u} \cdot \boldsymbol{\nabla}, \tag{2.1.29}$$

and the horizontal components of the Coriolis term in the β-plane approximation are given by

$$\mathbf{f}_\mathrm{h} = f(-v, u). \tag{2.1.30}$$

We have assumed that since η is independent of z, the horizontal accelerations are independent of z. So if $\mathbf{u}$ is also independent of z at $t = 0$, it will remain so. We also depth integrate the incompressibility condition Eq. (2.1.26b) using kinematic boundary conditions

$$w = \frac{D\eta}{Dt} \text{ at } z = \eta, \tag{2.1.31a}$$

$$w = -\frac{DH}{Dt} \text{ at } z = -H, \tag{2.1.31b}$$

where $H = H(x, y)$ is the bottom topography. From this we obtain the shallow water equations given by

$$\frac{D\mathbf{u}}{Dt} + \mathbf{f}_\mathrm{h} = -g\boldsymbol{\nabla}\eta \tag{2.1.32a}$$

$$\frac{\partial h}{\partial t} + \boldsymbol{\nabla} \cdot (\mathbf{u}h) = 0. \tag{2.1.32b}$$

Here, the fluid thickness is then given by

$$h = \eta + H \tag{2.1.33}$$

where according to our definition of η, we have that

$$\int \eta \, dx \, dy = 0, \tag{2.1.34}$$

and have defined the relative vorticity

$$\zeta \equiv \left(\frac{\partial v}{\partial x} - \frac{\partial u}{\partial y} \right). \tag{2.1.35}$$

We may eliminate the horizontal velocity divergence $\boldsymbol{\nabla} \cdot \mathbf{u}$ between ∂_y of the x-component of Eq. (2.1.32a) and ∂_x of the y-component of Eq. (2.1.32a), using Eq. (2.1.32b). From this we can show that the shallow water equations conserve potential vorticity

$$\frac{Dq}{Dt} = 0, \tag{2.1.36}$$

which we as we discussed §1, is essentially a statement that columns of fluid will conserve their mass and their angular momentum.

Since we will be working with turbulent systems which assume constant forcing, large scale drag and small scale dissipation, we introduce these into our system and our shallow water equations become

$$\frac{D\mathbf{u}}{Dt} + \mathbf{f}_{\mathrm{h}} + g\boldsymbol{\nabla}\eta = \mathbf{F} - \mathcal{D}_{\mathrm{H}}\nabla^2\mathbf{u} + \mathcal{D}_{\mathrm{B}}\nabla^4\mathbf{u} - r\mathbf{u}, \tag{2.1.37a}$$

$$\frac{\partial h}{\partial t} + \boldsymbol{\nabla} \cdot (\mathbf{u}h) = 0. \tag{2.1.37b}$$

Here $\mathbf{F}$ is the horizontal forcing term, the scale-selective horizontal harmonic and biharmonic diffusion terms have coefficients $\mathcal{D}_{\mathrm{H}}$ and $\mathcal{D}_{\mathrm{B}}$ respectively, and the Rayleigh friction has coefficient r.

2.1.3 The Quasi-geostrophic Equation

All numerical studies in this thesis will involve the barotropic vorticity equation, a simplified form of the quasi-geostrophic equation. We will derive the latter as an asymptotic approximation of the shallow-water equations Eq. (2.1.37). From here on we will assume flat bottom topography $H = H_0$, which is suitable for our purposes but is not necessary for the quasi-geostrophic formulation. Introducing

$$\psi \equiv \frac{g\eta}{f_0}, \tag{2.1.38}$$

we proceed to non-dimensionalise Eq. (2.1.37) using the following scaling

$$\begin{gathered}(x, y) = L\left(\tilde{x}, \tilde{y}\right), \quad t = \left(\frac{L}{U}\right)\tilde{t}, \quad \mathbf{u} = U\tilde{\mathbf{u}}, \quad \psi = UL\tilde{\psi}, \quad \beta = \frac{U}{L^2}\tilde{\beta}, \\ \mathbf{F} = \frac{U^2}{L}\tilde{\mathbf{F}}, \quad \mathcal{D}_{\mathrm{H}} = UL\tilde{\mathcal{D}}_{\mathrm{H}}, \quad \mathcal{D}_{\mathrm{B}} = UL^3\tilde{\mathcal{D}}_{\mathrm{B}}, \quad r = \frac{U}{L}\tilde{r},\end{gathered} \tag{2.1.39}$$

where tildes indicate non-dimensionalised quantities and U and L are the characteristic velocity and length-scale of the flow respectively. The non-dimensionalised shallow water equations for the horizontal momentum of a rotating fluid are then given by

$$R_{\mathrm{o}}\frac{D}{Dt}\mathbf{u} + \mathbf{f}_{\mathrm{h}} + \boldsymbol{\nabla}\psi = R_{\mathrm{o}}\left(\mathbf{F} + \mathcal{D}_{\mathrm{H}}\nabla^2\mathbf{u} - \mathcal{D}_{\mathrm{B}}\nabla^4\mathbf{u} - r\mathbf{u}\right), \tag{2.1.40a}$$

$$R_{\mathrm{o}}\left[\frac{\partial\psi}{\partial t} + \boldsymbol{\nabla}\cdot(\mathbf{u}\psi)\right] + \mathcal{B}\boldsymbol{\nabla}\cdot\mathbf{u} = 0. \tag{2.1.40b}$$

where all quantities are now assumed to be non-dimensionalised and we have dropped the tildes for brevity. The non-dimensonal Coriolis parameter is

$$f = (1 + R_{\mathrm{o}}\beta y) \tag{2.1.41}$$

and, we have introduced the Rossby number

$$R_{\mathrm{o}} = \frac{U}{f_0 L} \tag{2.1.42}$$

and the Burger number

$$\mathcal{B} = \frac{gH_0}{f_0^2 L^2}. \tag{2.1.43}$$

For typical mesoscale processes in oceanographic flows $f_0 \sim 10^{-4}$ s^{-1}, $L \sim 10^5$ m, $U \sim 10^{-1}$ ms^{-1} and we find $R_{\mathrm{o}} = 10^{-2} \ll 1$ in this case.

$R_o \ll 1$ and rotational effects dominate over inertial forces. At leading order the Coriolis force then balances the pressure gradient force and the flow is said to be in geostrophic balance with the geostrophic velocity $\mathbf{u}_{\mathrm{G}}$ defined by:

$$\mathbf{u}_{\mathrm{G}} \equiv \left(-\frac{\partial\psi}{\partial y}, \frac{\partial\psi}{\partial x}\right) \tag{2.1.44}$$

and

$$\boldsymbol{\nabla}\cdot\mathbf{u}_{\mathrm{G}} = 0. \tag{2.1.45}$$

Therefore we can identify ψ as the geostrophic streamfunction for the flow.

At the next leading order, given by $\mathcal{O}\left(R_{\mathrm{o}}\right)$, we substitute Eq. (2.1.44) into the previously neglected terms given in Eq. (2.1.40).

$$R_o \frac{\partial u_G}{\partial t} + (\mathbf{u}_G \cdot \boldsymbol{\nabla}) u_G - v - R_o \beta y v_G = \\ R_o \left(F_x + \mathcal{D}_H \nabla^2 u_G - \mathcal{D}_B \nabla^4 u_G - r u_G \right), \tag{2.1.46a}$$

$$R_o \frac{\partial v_G}{\partial t} + (\mathbf{u}_G \cdot \boldsymbol{\nabla}) v_G + u + R_o \beta y u_G = \\ R_o \left(F_y + \mathcal{D}_H \nabla^2 v_G - \mathcal{D}_B \nabla^4 v_G - r v_G \right), \tag{2.1.46b}$$

$$R_o \frac{\partial \psi}{\partial t} + \mathcal{B} \boldsymbol{\nabla} \cdot \mathbf{u} = 0, \tag{2.1.46c}$$

where F_x and F_y are the zonal and meridional components of $\mathbf{F}$. Taking ∂_y of Eq. (2.1.46a) and ∂_x of Eq. (2.1.46b) and using Eq. (2.1.45) to eliminate the ageostrophic component of the velocity with Eq. (2.1.46c), we obtain the non-dimensionalised quasi-geostrophic equation which is consistent at $\mathcal{O}(R_o)$:

$$R_o \left[\frac{\partial \zeta_G}{\partial t} + J(\psi, \zeta_G) + \beta v \right] - \frac{R_o}{\mathcal{B}} \left[\frac{\partial \psi}{\partial t} \right] = \\ R_o \left(\mathscr{F} + \mathcal{D}_H \nabla^2 \zeta_G - \mathcal{D}_B \nabla^4 \zeta_G - r \zeta_G \right), \tag{2.1.47}$$

where the Jacobian is defined as

$$J(A, B) \equiv \frac{\partial A}{\partial x}\frac{\partial B}{\partial y} - \frac{\partial A}{\partial y}\frac{\partial B}{\partial x}, \tag{2.1.48}$$

the geostrophic relative vorticity is given by

$$\zeta_G = \nabla^2 \psi, \tag{2.1.49}$$

and the external forcing is

$$\mathscr{F} = \frac{\partial F_x}{\partial y} - \frac{\partial F_y}{\partial x}. \tag{2.1.50}$$

In the absence of external forcing, this is a single equation for ζ from which we can recover ψ.

The Burger number may be written as

$$\mathcal{B} = \left(\frac{L_D}{L} \right)^2, \tag{2.1.51}$$

where $L_D = \sqrt{gH_0}/f_0$ is the external Rossby radius of deformation. For our purposes, we will assume that $L \ll L_D \implies \mathcal{B} \to \infty$ and Eq. (2.1.46c) will reduce to

$$\boldsymbol{\nabla} \cdot \mathbf{u} = \boldsymbol{\nabla} \cdot \mathbf{u}_G = 0. \tag{2.1.52}$$

This is the so-called rigid-lid approximation since it amounts to negligible variations in the free surface. This limit precludes the existence of inertia-gravity waves, which typically arise from perturbations associated with η.

One subtlety from Eq. (2.1.46c) is mass conservation which is trivially satisfied when $R_\mathrm{o} \ll 1$ and the flow is in geostrophic balance. However for the dynamics to conserve mass to $\mathcal{O}(R_\mathrm{o})$ we require that

$$\frac{d}{dt}\iint_\Omega \psi\, dx\, dy = 0 \implies \iint_\Omega \psi\, dx\, dy = C, \tag{2.1.53}$$

where C is a constant. Given Eq. (2.1.34) we can set $C = 0$.

2.2 Channel Model

The quasi-geostrophic equation with flat bottom topography and the rigid-lid approximation reduces to the barotropic vorticity equation on the β-plane. We will consider the barotropic vorticity equation in a rentrant channel model, representing a 2D cylindrical shell of incompressible fluid which is laterally bounded. This configuration is chosen because we will be interested in studying zonal structures. For the purposes of our discussion, we will work with the non-dimensional equations and our domain will be $\Omega = \{[0, 2\pi] \times [0, \pi]\}$, $(x, y) \in \Omega$. However, our results in subsequent chapters will be presented in dimensional units.

The final form of our barotropic vorticity equation is now given by

$$\frac{\partial \zeta}{\partial t} = -u\frac{\partial}{\partial x}\zeta - v\frac{\partial}{\partial y}\zeta - \beta v - \mathcal{D}_\mathrm{B}\nabla^4\zeta + \mathcal{D}_\mathrm{H}\nabla^2\zeta - r\zeta + \mathscr{F} \tag{2.2.1a}$$

where

$$\zeta = \nabla^2\psi \tag{2.2.1b}$$

and the quasi-geostrophic velocity field is given by

$$\mathbf{u} = (u, v) = \left(-\frac{\partial \psi}{\partial y}, \frac{\partial \psi}{\partial x}\right) \tag{2.2.2a}$$

$$\text{such that } \boldsymbol{\nabla}\cdot\mathbf{u} = 0, \tag{2.2.2b}$$

where we have dropped the G notation since we will only be working with the quasi-geostrophic velocity. We remark that we have returned to the non-conservation form of our vorticity equation since conservation is arbitrarily satisfied by working with a streamfunction representation of the flow. This is also found to improve the numerical consistency when numerically discretising the flow equations. Periodic conditions are imposed on the east and west boundaries. The north and south boundaries require the physical condition of no flow through the boundary wall. We will also need to consider some additional constraints to solve our system of equations when dealing with forcing and dissipation terms.

2.2.1 Boundary Conditions

We will need to find an appropriate set of boundary conditions on Eq. (2.2.1) such that the problem is well posed and is consistent with the shallow water equations Eq. (2.1.40) from which it is derived. We will then examine their affect on key conservation laws.

The physical boundary condition is no flow through the channel walls

$$v = \frac{\partial \psi}{\partial x} = 0 \tag{2.2.3}$$

when $y = 0$ or $y = \pi$, so

$$\psi = \psi_0 \tag{2.2.4}$$

on the lateral boundaries, where ψ_0 is a time-dependent coefficient that is, in general, different on each boundary. The east and west boundaries will be periodic. Together with an appropriate initial condition, these provides a unique solution to Eq. (2.1.40) and Eq. (2.2.1) when the flow is inviscid and unforced. Non-conservative terms will require us to consider extra boundary conditions and consistency relations. Increasing the order of the equation through the introduction of the biharmonic diffusion term requires four additional boundary conditions to be specified. If we neglect the advection and Coriolis terms we recover a high order heat equation of the type considered by Lee and Hill (1983). In their work they demonstrated that there are four sets of boundary conditions which provide a unique solution. Here, we will focus on the two commonly employed sets.

The Dirichlet conditions as employed in the works of Berloff et al. (2009b); McWilliams (1977); Pedlosky (1987a) are given by

$$\zeta_{\mathrm{D}} = \frac{\partial^2 \zeta_{\mathrm{D}}}{\partial y^2} = 0 \tag{2.2.5}$$

where we use the subscript D to denote this set of conditions. Because $\partial_x v = 0$ in Eq. (2.2.1b), by virtue of Eq. (2.2.3) the analogue of this for the shallow water equations are the free slip conditions given by

$$\frac{\partial u}{\partial y} = \frac{\partial^3 u}{\partial y^3} = 0. \tag{2.2.6}$$

Another choice is to impose a mixture of Neumann conditions on the zonal mean mode and Dirichlet conditions on the non-mean modes (e.g. Esler (2008); Williams et al. (2009)):

$$\begin{aligned} \overline{\frac{\partial \zeta_{\mathrm{ND}}}{\partial y}} &= \overline{\frac{\partial^3 \zeta_{\mathrm{ND}}}{\partial y^3}} = 0, \\ \zeta'_{\mathrm{ND}} &= \frac{\partial^2 \zeta'_{\mathrm{ND}}}{\partial y^2} = 0 \end{aligned} \tag{2.2.7}$$

in which the zonal mean mode is denoted by an overline, the non-mean modes with a prime and we denote this mixed basis with subscript ND[1]. The boundary conditions equivalent to Eq. (2.2.7) for the shallow water equations are

$$\overline{\frac{\partial^2 u}{\partial y^2}} = \overline{\frac{\partial^4 u}{\partial y^4}} = 0. \tag{2.2.8}$$

2.3 Consistency Conditions

In the previous section we have derived the quasi-geostrophic equation as an asymptotic approximation of the shallow water equations up to $\mathcal{O}\left(R_{\mathrm{o}}\right)$, and presented two sets of boundary conditions that results in a well-posed problem. We will now compare the effect of imposing either Dirichlet boundary conditions, or the mixed boundary conditions on the conservation laws of the flow. The task then is to ensure that solutions from our simplified quasi-geostrophic channel model will be consistent with the momentum equation. McWilliams (1977) dealt with this problem for a multiply connected domain with multiple layers in which they derived a set of general consistency conditions from integral constraints. In their work, they considered Dirichlet boundary conditions, which ensured that there was no diffusive flux of tangential momentum through the solid boundaries. Here we will present these consistency conditions in a form applicable to the barotropic channel model and discuss how they may be imposed using either set of boundary conditions.

2.3.1 Conservation of Circulation

The circulation around the closed contour $\partial\Omega$ bounding the domain is found by integrating ζ

$$\Gamma \equiv \iint_{\Omega} \zeta \, dx \, dy = \oint_{\partial\Omega} \mathbf{u} \cdot \mathbf{dr} = 2\pi \left(\overline{u}\big|_{y=0} - \overline{u}\big|_{y=\pi} \right). \tag{2.3.1}$$

[1]Motivation for this choice can be traced to the arbitrariness of the boundary condition on $\overline{\psi}$, since the physical boundary condition Eq. (2.2.3) requires only that $\psi' = 0$ on the boundaries.

Then integrating Eq. (2.2.1a) over the domain allows us to obtain an equation for the evolution equation for Γ given by

$$\frac{d\Gamma}{dt} = \int_0^{2\pi} \left[\mathcal{D}_{\mathrm{H}} \frac{\partial \zeta}{\partial y} - \mathcal{D}_{\mathrm{B}} \frac{\partial^3 \zeta}{\partial y^3} \right]_0^{\pi} dx - r\Gamma. \tag{2.3.2}$$

where convective and Coriolis terms vanish under periodicity and hard wall boundary conditions and we assume the forcing has zero zonal mean on the boundaries. We see immediately that the Dirichlet boundary conditions Eq. (2.2.5) cannot conserve circulation as odd-y derivatives of ζ neither vanish nor cancel. In contrast, the vanishing odd-y derivatives in the mixed boundary conditions of Eq. (2.2.7) necessarily leads to conservation of circulation. The solution to the circulation equation under mixed boundary conditions would then be

$$\Gamma_{\mathrm{ND}}(t) = \Gamma_{\mathrm{ND}}(0) e^{-rt}. \tag{2.3.3}$$

Hence, if $\Gamma_{\mathrm{ND}}(0) = 0$, circulation is conserved.

In either case, we must ensure consistency with the shallow water equations. Integrating the shallow water momentum equation given by Eq. (2.1.40a) along *either* the upper or lower channel boundaries gives

$$\frac{d\Gamma_i}{dt} = \int_0^{2\pi} \left(-D_{\mathrm{H}} \nabla^2 u + D_{\mathrm{B}} \nabla^4 u \right) dx - r\Gamma_i \tag{2.3.4}$$

for $y = 0$ or $y = \pi$, where the Coriolis force, the pressure gradient and the convective terms vanish under periodicity and no-normal flow. We observe that

$$\nabla^2 u = -\frac{\partial}{\partial y} \nabla^2 \psi = -\frac{\partial \zeta}{\partial y} \tag{2.3.5}$$

and similarly

$$\nabla^4 u = -\frac{\partial}{\partial y} \nabla^4 \psi = -\frac{\partial}{\partial y} \nabla^2 \zeta \tag{2.3.6}$$

so Eq. (2.3.4) may be written as

$$\frac{d\Gamma_i}{dt} = \int_0^{2\pi} \left(D_{\mathrm{H}} \frac{\partial \zeta}{\partial y} - D_B \frac{\partial^3 \zeta}{\partial y^3} \right) dx - r\Gamma_i \tag{2.3.7}$$

where $i = 1, 2$ corresponds to the boundaries at $y = 0$ and $y = \pi$. We can see that in the absence of dissipation, circulation would be conserved. In fact, as demonstrated in Pedlosky (1987b), in the inviscid case circulation is conserved for *any* contour in the domain that extends from one periodic boundary to the corresponding point on the other periodic boundary.

Comparing Eq. (2.3.7) with the circulation law obtained using the barotropic vorticity equation Eq. (2.3.2), we see that the momentum equation imposes more stringent conditions in requiring separate circulation equations on the boundaries. So although solving the total circulation equation given by Eq. (2.3.2) leads to a unique solution of Eq. (2.2.1), it is not consistent with Eq. (2.1.40a) (Graef and Müller, 1996). For Dirichlet boundary conditions given in Eq. (2.2.6), consistency is ensured if circulation equations are solved at each boundary according to Eq. (2.3.7), essentially dictating how $\overline{u}$ varies at each boundary. Mixed boundary conditions Eq. (2.2.8) may conserve circulation on each boundary separately in Eq. (2.3.4) and consistency is only ensured when the total circulation *and* the circulation on *each* boundary are conserved

$$\begin{aligned} \left.\frac{d\Gamma_{\mathrm{ND}}}{dt}\right|_{y=0} &= -\left.\frac{d\Gamma_{\mathrm{ND}}}{dt}\right|_{y=\pi} = 0 \\ \implies \left.\Gamma_{\mathrm{ND}}\right|_{y=0} &= -\left.\Gamma_{\mathrm{ND}}\right|_{y=\pi} = \text{constant}, \\ \text{so} \quad \left.\overline{u}_{\mathrm{ND}}\right|_{y=0} &= -\left.\overline{u}_{\mathrm{ND}}\right|_{y=\pi} = \text{constant}. \end{aligned} \tag{2.3.8}$$

If the flow evolves from rest, the constant is zero and so mixed boundary conditions require that $\overline{u} = 0$ on the boundaries.

In summary, for a flow evolving from rest we have

$$\frac{d\Gamma_{\mathrm{D}}}{dt} \neq 0, \; \frac{d\Gamma_{\mathrm{ND}}}{dt} = 0. \tag{2.3.9}$$

i.e. circulation is conserved under Dirichlet boundary conditions but not under mixed boundary conditions.

2.3.2 Conservation of Momentum and Impulse

McWilliams (1977) did not derive a momentum condition but we will do so here in order to motivate the choice of a Dirichlet boundary condition. Meridional momentum cannot contribute net momentum transport in this channel geometry. It follows that total momentum changes are governed only by the zonal component of the shallow water equation Eq. (2.1.40a):

$$\frac{\partial u}{\partial t} = -u\frac{\partial u}{\partial x} - v\frac{\partial u}{\partial y} - \frac{fv}{R_o} + F_x + D_H\nabla^2 u - D_B\nabla^4 u - ru - \frac{1}{R_o}\frac{\partial \psi}{\partial x}, \tag{2.3.10}$$

The total momentum is found by integrating the zonal velocity over the domain to obtain

$$P \equiv \iint_\Omega u \, dx \, dy = \iint_\Omega -\frac{\partial \psi}{\partial y} \, dx \, dy = 2\pi \left(\left.\overline{\psi}\right|_{y=0} - \left.\overline{\psi}\right|_{y=\pi} \right). \tag{2.3.11}$$

We know that in general $\overline{\psi}$ is equal to (different) time-dependent coefficients on the boundaries. The expression for P therefore shows that a difference between those values will determine the net zonal momentum in the system. To determine the rate of change of P with time to $\mathcal{O}(R_o)$, we integrate Eq. (2.3.10)

$$\begin{aligned} \frac{dP}{dt} &= \int_0^{2\pi} \left[D_{\mathrm{H}} \frac{\partial u}{\partial y} - D_{\mathrm{B}} \frac{\partial^3 u}{\partial y^3} \right]_0^{\pi} dx - rP \\ &= \int_0^{2\pi} \left[-D_{\mathrm{H}} \zeta + D_{\mathrm{B}} \frac{\partial^2 \zeta}{\partial y^2} \right]_0^{\pi} dx - rP. \end{aligned} \tag{2.3.12}$$

Here we have used the divergence theorem in the first line and made use of the relation

$$\zeta = -\frac{\partial u}{\partial y} \tag{2.3.13}$$

when $y = 0$ or $y = \pi$, and assumed that forcing does not contribute net momentum. Under Dirichlet boundary conditions of Eq. (2.2.6), the diffusion terms do not contribute net zonal momentum. The Rayleigh friction will decay momentum according to

$$P_{\mathrm{D}}(t) = P_{\mathrm{D}}(0)\, e^{-rt} \tag{2.3.14}$$

Hence, if the flow evolves from rest, momentum will be conserved and will be zero. In this case, the coefficients must satisfy

$$\psi_{0_{\mathrm{D}}}\big|_{y=0} = \psi_{0_{\mathrm{D}}}\big|_{y=\pi} \tag{2.3.15}$$

which, as we will see later, can be determined using mass conservation corresponding to Eq. (2.1.53). The mixed boundary conditions given in Eq. (2.2.8) will not conserve momentum since the diffusion terms may contribute momentum to the system.

In summary, we have established that

$$\frac{dP_{\mathrm{D}}}{dt} = 0, \frac{dP_{\mathrm{ND}}}{dt} \neq 0, \tag{2.3.16}$$

i.e. that momentum is conserved under Dirichlet boundary conditions but not under mixed boundary conditions.

The difficulty in working with the momentum conservation law is that the dynamics of our system are governed by a vorticity equation. The more relevant quantity to consider is then the total impulse of the system that is defined by

$$\mathbf{I} \equiv \iint_{\Omega} \mathbf{r} \times \zeta \hat{\mathbf{k}}\, dx\, dy. \tag{2.3.17}$$

As in the case for conservation of momentum, net changes in impulse can only arise in the zonal component due to the geometric constraints imposed by the channel model. It follows that

$$I = \mathbf{I} \cdot \mathbf{r} = \iint_{\Omega} y\zeta \, dx \, dy = -\int_0^{2\pi} [uy]_0^{\pi} \, dx + P. \tag{2.3.18}$$

Then the rate of change of zonal impulse is related to the rate of change of zonal momentum by

$$\frac{dI}{dt} = -\int_0^{2\pi} \frac{\partial}{\partial t} [uy]_0^{\pi} \, dx + \frac{dP}{dt}. \tag{2.3.19}$$

As we have seen, momentum is conserved for the Dirichlet boundary conditions but u on the boundaries may vary according to the circulation equation given by Eq. (2.3.7) so, in this case, impulse changes are given by

$$\frac{dI_{\mathrm{D}}}{dt} = -\int_0^{2\pi} \left[y \frac{\partial u}{\partial t} \right]_0^{\pi} dx. \tag{2.3.20}$$

In contrast, the mixed conditions require that $\overline{u} = 0$ on the boundaries when the flow evolves from rest. The rate of change of impulse with time is then given by

$$\frac{dI_{\mathrm{ND}}}{dt} = \frac{dP_{\mathrm{ND}}}{dt}. \tag{2.3.21}$$

and $I_{\mathrm{ND}}(t) = P_{\mathrm{ND}}(t)$.

The evolution equation for the impulse is found by multiplying Eq. (2.2.1a) by y and integrating over the domain. The Coriolis term vanishes under periodicity and the convective terms vanish under periodicity and no normal flow. Impulse evolution is then determined by forcing and dissipation terms

$$\begin{aligned} \frac{dI}{dt} &= \iint_{\Omega} y \left(\mathscr{F} + \mathcal{D}_{\mathrm{H}} \nabla^2 \zeta - \mathcal{D}_{\mathrm{B}} \nabla^4 \zeta \right) dx \, dy - rI \\ &= \iint_{\Omega} F_x \, dx \, dy + \int_0^{2\pi} \left[y \left(-F_x + D_H \frac{\partial \zeta}{\partial y} - D_B \frac{\partial^3 \zeta}{\partial y^3} \right) \right]_0^{\pi} dx \\ &\quad + \int_0^{2\pi} \left[-D_H \zeta + D_B \frac{\partial^2 \zeta}{\partial y^2} \right]_0^{\pi} dx - rI. \end{aligned} \tag{2.3.22}$$

As before, we assume the form of the forcing chosen will conserve impulse. We can now find a consistency condition on the momentum by subtracting Eq. (2.3.12) from Eq. (2.3.22), and making use of the relation Eq. (2.3.13) to obtain

$$\int_0^{2\pi} \left[y \frac{\partial u}{\partial t} \right]_0^{\pi} dx = \int_0^{2\pi} \left[y \left(D_H \frac{\partial^2 u}{\partial y^2} - D_B \frac{\partial^4 u}{\partial y^4} - ru \right) \right]_0^{\pi} dx. \tag{2.3.23}$$

As we have seen already, Dirichlet boundary conditions conserve momentum and so Eq. (2.3.23) provides an evolution equation for $\overline{u}$ on the boundaries which is the same as that obtained from the circulation given by Eq. (2.3.2). In this case, consistency in circulation ensures consistency in momentum. Where as, consistency with the momentum equation is automatically satisfied by the mixed boundary conditions. For these conditions, the zonal impulse evolution equation is equal to the zonal momentum evolution equation given by Eq. (2.3.12). In either case, impulse is not conserved

$$\frac{dI_D}{dt} \neq 0, \; \frac{dI_{ND}}{dt} \neq 0. \tag{2.3.24}$$

2.3.3 Conservation of Energy

The total energy of the system may be found by multiplying Eq. (2.2.1b) by $-\psi$ and integrating over the domain. The time evolution of this quantity may be written as

$$\frac{dE_\zeta}{dt} \equiv \iint_\Omega -\psi \frac{\partial \zeta}{\partial t}\, dx\, dy = \int_0^{2\pi} \left[\psi \frac{\partial u}{\partial t}\right]_0^\pi dx + \frac{dE_\mathrm{m}}{dt} \tag{2.3.25}$$

where we identify the total kinetic energy

$$E_\mathrm{m} \equiv \iint_\Omega \frac{1}{2} \boldsymbol{\nabla}\psi \cdot \boldsymbol{\nabla}\psi\, dx\, dy. \tag{2.3.26}$$

Multiplying Eq. (2.2.1a) by $-\psi$ and integrating over the domain allows us to determine the rate of change of energy of the system. Energy contributions from the Coriolis and convective terms vanish under periodicity and no-normal flow. The rate of change of energy is then controlled by the forcing and dissipation mechanisms according to

$$\begin{aligned} \frac{dE_\zeta}{dt} &= \iint_\Omega \left(\psi \mathscr{F} - \psi \mathcal{D}_\mathrm{H} \nabla^2 \zeta + \psi \mathcal{D}_\mathrm{B} \nabla^4 \zeta + \psi r \zeta\right) dx\, dy \\ &= \iint_\Omega \left(\mathbf{u}\cdot\mathbf{F} + \mathcal{D}_\mathrm{H} \mathbf{u}\cdot\nabla^2 \mathbf{u} - \mathcal{D}_\mathrm{B} \mathbf{u}\cdot\nabla^4 \mathbf{u}\right) dx\, dy \\ &\quad - \int_0^{2\pi} \left[\psi \left(\mathcal{D}_\mathrm{H} \frac{\partial^3 \zeta}{\partial y^3} - \mathcal{D}_\mathrm{B} \frac{\partial^3 \zeta}{\partial y^3} + -ru\right)\right]_0^\pi dx - 2rE_\mathrm{m}. \end{aligned} \tag{2.3.27}$$

We can also evaluate the corresponding equation for the rate of change of energy directly from the shallow water equations by taking the dot product of Eq. (2.1.40a) with $\mathbf{u}$ and integrating over the domain. Changes in energy are then determined by

$$\frac{dE_\mathrm{m}}{dt} = \iint_\Omega \left(\mathbf{u}\cdot\mathbf{F} + \mathcal{D}_\mathrm{H} \mathbf{u}\cdot\nabla^2 \mathbf{u} - \mathcal{D}_\mathrm{B} \mathbf{u}\cdot\nabla^4 \mathbf{u}\right) dx\, dy - 2rE_\mathrm{m}. \tag{2.3.28}$$

Subtracting Eq. (2.3.28) from Eq. (2.3.27) and assuming that forcing is zero on the boundaries, leads to the consistency condition

$$\int_0^{2\pi}\left[\psi\frac{\partial u}{\partial t}\right]_0^{\pi} dx = \int_0^{2\pi}\left[\psi\left(\mathcal{D}_{\mathrm{H}}\frac{\partial^2 u}{\partial y^2} - \mathcal{D}_{\mathrm{B}}\frac{\partial^4 u}{\partial y^4} - ru\right)\right]_0^{\pi} dx. \tag{2.3.29}$$

where we have made use of the relation Eq. (2.3.13). This shows that for Dirichlet boundary conditions the coefficients $\psi = \psi_0$ on each boundary must be constant and equal. We will argue that these can be set to zero, automatically satisfying this consistency condition. Had we chosen another constant, the consistency condition corresponding to Eq. (2.3.29) is satisfied provided the circulation condition given by Eq. (2.3.8) is imposed. In the case of mixed boundary conditions odd-y derivatives of $\overline{\zeta}$ are zero. Since ψ is constant along the boundaries, the line integrals will vanish and consistency is ensured.

2.3.4 Conservation of Enstrophy and Potential Enstrophy

As we have seen, the inviscid unforced shallow water equations conserve potential vorticity. If we multiply Eq. (2.1.36) by q, we find the rate of change of potential enstrophy q^2

$$q\frac{Dq}{Dt} = \frac{1}{2}\frac{Dq^2}{Dt} = 0. \tag{2.3.30}$$

We see that in the absence of forcing and dissipation, since q is conserved then so too is q^2. This is true in any domain geometry. Hence the total potential enstrophy will be conserved:

$$\mathcal{Z}_q \equiv \iint_\Omega q^2\,dx\,dy. \tag{2.3.31}$$

The total enstrophy of the system is defined by

$$\mathcal{Z}_\zeta \equiv \iint_\Omega \frac{1}{2}\zeta^2\,dx\,dy. \tag{2.3.32}$$

If we consider the inviscid, unforced form of Eq. (2.2.1a), multiply by ζ and integrate over the domain, we find that

$$\frac{d\mathcal{Z}_\zeta}{dt} = 0, \tag{2.3.33}$$

where the Coriolis and convective terms vanish under continuity, periodicity and no normal flow. In general, $\mathcal{Z}_\zeta$ is not a conserved quantity. However for the channel geometry we will be interested in, it turns out that simultaneous conservation of both $\mathcal{Z}_\zeta$ and $\mathcal{Z}_q$ is achieved in the absence of forcing and dissipation. Though it is now well established that potential enstrophy is the quasi-geostrophic analogue of enstrophy in the 2D vorticity equation, potential vorticity was not discussed by Rhines (1975). The advantage of making the connection with potential vorticity is that generic features of 2D turbulence such as the inverse cascade and the direct enstrophy cascade will persist in geophysical flows and will not be geometry dependent (i.e. cases where $\mathcal{Z}_q$ is conserved but $\mathcal{Z}_\zeta$ is not).

We find the rate of change of $\mathcal{Z}_\zeta$ by multiplying Eq. (2.2.1a) by ζ and integrating over the domain:

$$\begin{aligned} \frac{d\mathcal{Z}_\zeta}{dt} &= \iint_\Omega \left(\zeta\mathscr{F} + \mathcal{D}_H\zeta\nabla^2\zeta - \mathcal{D}_B\zeta\nabla^4\zeta - r\zeta^2\right)\, dx\, dy \\ &= \iint_\Omega \left(\mathbf{F}\cdot\nabla^2\mathbf{u} - \mathcal{D}_H\nabla^2\mathbf{u}\cdot\nabla^2\mathbf{u} + \mathcal{D}_B\nabla^2\mathbf{u}\cdot\nabla^4\mathbf{u}\right)\, dx\, dy \\ &\quad + \int_0^{2\pi}\left[\zeta\left(F_x + \mathcal{D}_H\frac{\partial\zeta}{\partial y} - \mathcal{D}_B\frac{\partial^3\zeta}{\partial y^3}\right)\right]_0^\pi dx - 2r\mathcal{Z}_\zeta \end{aligned} \tag{2.3.34}$$

The line integrals along the lateral boundaries vanish for both mixed and Dirichlet boundary conditions. It follows that neither set of boundary conditions presents any additional sources or sinks of enstrophy and the enstrophy evolves according to

$$\frac{d\mathcal{Z}_\zeta}{dt} = \iint_\Omega \left(\mathbf{F}\cdot\nabla^2\mathbf{u} - \mathcal{D}_H\nabla^2\mathbf{u}\cdot\nabla^2\mathbf{u} + \mathcal{D}_B\nabla^2\mathbf{u}\cdot\nabla^4\mathbf{u}\right)\, dx\, dy - 2r\mathcal{Z}_\zeta. \tag{2.3.35}$$

There is no analogue condition in the shallow water equations Eq. (2.1.37) since Eq. (2.3.32) is defined by a vorticity equation. For completeness we also calculate the rate of the change of $\mathcal{Z}_q$ when forcing and dissipation terms are included. To do this we recast Eq. (2.2.1a) in terms of q:

$$\frac{Dq}{Dt} = \mathscr{F} - \mathcal{D}_B\nabla^4\left(q-f\right) + \mathcal{D}_H\nabla^2\left(q-f\right) - r\left(q-f\right), \tag{2.3.36}$$

multiply by q and integrate over the domain, this gives:

$$\frac{d\mathcal{Z}_q}{dt} = \frac{d\mathcal{Z}_\zeta}{dt} + 2f_0\frac{d\Gamma}{dt} + 2\beta\frac{dI}{dt}. \tag{2.3.37}$$

2.4 Solution to Poisson's Equation

Now we seek a general solution to Eq. (2.2.1b) with the periodic boundary conditions

$$\psi|_{x=0} = \psi|_{x=2\pi}, \tag{2.4.1}$$

and no normal flow through lateral walls given by Eq. (2.2.4) where ψ is equal to (separate) time-dependent coefficients along each boundary. First we solve the homogeneous equation and assume solutions of a separable form

$\psi(x,y) = X(x)Y(y)$ such that Eq. (2.2.1b) becomes

$$\frac{X''}{X} = -\frac{Y''}{Y} = \gamma. \tag{2.4.2}$$

where γ is a constant. When $\gamma < 0$, solutions are of the form

$$\psi(x,y) = \left(A_k e^{ky} + B_k e^{-ky}\right) e^{ikx} \tag{2.4.3}$$

where $k = \sqrt{\gamma}$, which satisfies boundary conditions Eq. (2.4.1) but not Eq. (2.2.4). When $\gamma = 0$, solutions are of the form

$$\psi(x,y) = (c_1 + c_2 y)(c_3 + c_4 x). \tag{2.4.4}$$

This satisfies boundary conditions Eq. (2.4.1) and Eq. (2.2.4) when $c_4 = 0$. When $\gamma > 0$, the solutions are of the form

$$\psi(x,y) = \psi(x,y) = (D_k \cos ky + E_k \sin ky)\left(A_k e^{kx} + B_k e^{-kx}\right) \tag{2.4.5}$$

This satisfies boundary condition Eq. (2.2.4) when $D_k = 0$ but does not satisfy Eq. (2.4.1). Therefore the only solution the homogenous equation which satisfies the boundary conditions is

$$\psi_{\text{h}}(x,y) = c_1 + \frac{c_2 - c_1}{\pi} y. \tag{2.4.6}$$

where we have relabelled $c_1 c_3 \to c_1$ and $c_2 \to \frac{c_2 - c_1}{\pi}$. The coefficients $c_1(t)$ and $c_2(t)$ determine the time-dependent coefficients ψ_0 on each boundary:

$$\begin{aligned} \psi_0|_{y=0} &= c_1(t), \\ \psi_0|_{y=\pi} &= c_2(t), \end{aligned} \tag{2.4.7}$$

and the general solution is given by

$$\psi(x,y,t) = c_1(t) - \frac{c_2(t) - c_1(t)}{\pi} y + \psi_{\text{PI}}(x,y,t), \tag{2.4.8}$$

where ψ_{PI} is the particular integral which will be solved under the Dirichlet or mixed boundary conditions derived previously.

For Dirichlet conditions we know that the equations will conserve momentum and if the flow evolves from rest $\implies c_2 = c_1$. The remaining constant c_1 is fixed by appealing to mass conservation given by Eq. (2.1.53):

$$c_1 = -\frac{\iint_\Omega \psi_{\text{PI}}\, dx\, dy}{2\pi^2}. \tag{2.4.9}$$

Note that the effect of boundary Kelvin waves may be mimicked when c_1 is time-varying (Milliff and McWilliams, 1994) which is why Salmon (1998a) implies that choosing c_1 = constant, to suppress this effect, may simplify the dynamics. However, this is only a concern in systems with small Burger number given by Eq. (2.1.51), our choice to use a rigid-lid approximation suppresses all Kelvin waves.

For the mixed conditions we have found that, for flows evolving from rest, $\overline{u} = 0$ on each of the lateral boundaries. Using this, one of the constants may be determined by taking $-\partial_y$ of Eq. (2.4.8) to obtain u and evaluating its zonal mean mode at *one* of the boundaries:

$$\frac{c_2 - c_1}{\pi} = \left.\frac{\partial \overline{\psi}_{\mathrm{PI}}}{\partial y}\right|_{y=0 \text{ or } y=\pi}. \tag{2.4.10}$$

The other constant is determined using mass conservation in Eq. (2.1.53).

2.5 Choice in Boundary Conditions

In §2.2 we introduced the mathematical description of a zonally periodic, meriodinally bounded channel and examined how different boundary condition choices affect the conservation laws. Through this we have found that there are a number of consistency conditions we need to satisfy. Our choice is between the Dirichlet conditions given in Eq. (2.2.5) and a mixture of Neumann conditions on the zonal mean mode and Dirichlet on the non-mean modes given in Eq. (2.2.7). We summarise these, and the results we have obtained from the integral constraints discussed in §2.3, in Table 2.1.

The main virtue of the mixed boundary conditions is that the circulation is conserved and the consistency relation given by Eq. (2.3.8), is automatically satisfied. However, the mixed conditions also require that the mean flow modes and non-mean flow modes are treated separately, which increases the numerical complexity of the problem. For Dirichlet conditions, Eq. (2.3.8) is in principle required to be solved to determine the equal constants $\psi_0(t)$ on each boundary. However, we have seen that momentum conservation allows us to choose this constant such that mass is conserved. By-passing the use of the consistency condition to solve Eq. (2.2.1) using Dirichlet boundary conditions, is a unique feature of a single layer channel models. For models with multiple layers, we would need to solve the consistency condition given by Eq. (2.3.8), which in turn would require specifying the coefficients $\psi = \psi_0$ on the boundary (McWilliams, 1977). We will proceed using the mixed boundary condition choice in order to conserve the circulation.

Table 2.1: Summary of boundary conditions on the barotropic vorticity equation given in Eq. (2.2.1) and associated consistency conditions derived in this chapter. If Dirichlet boundary conditions given in Eq. (2.2.5) are imposed, the flow is not evolved on the boundary. If the mixed boundary conditions given in Eq. (2.2.7) are imposed, only the zonal mean mode is evolved on the boundary.

Variable	Dirichlet	Mixed Neumann and Dirichlet
ψ	$\psi_{\mathrm{D}} = c_1$	$\overline{\psi}_{\mathrm{ND}} = c_i \ (i = 1, 2), \ \psi'_{\mathrm{ND}} = 0$
u		$\overline{u}_{\mathrm{ND}} = 0$
v	$v_{\mathrm{D}} = 0$	$\overline{v}_{\mathrm{ND}} = 0, \ v'_{\mathrm{ND}} = 0$
ζ	$\zeta_{\mathrm{D}} = 0$	$\zeta'_{\mathrm{ND}} = 0$
$\frac{\partial \zeta}{\partial y}$		$\frac{\partial \overline{\zeta}}{\partial y}_{\mathrm{ND}} = 0$
$\nabla^2 \zeta$	$\nabla^2 \zeta_{\mathrm{D}} = 0$	$\nabla^2 \zeta'_{\mathrm{ND}} = 0$
$\frac{\partial^3 \zeta}{\partial y^3}$		$\frac{\partial^3 \overline{\zeta}}{\partial y^3}_{\mathrm{ND}} = 0$

2.6 Stochastic Forcing

So far we assumed that the following holds for the forcing term in Eq. (2.2.1):

1. The curl of the forcing contributes zero net circulation i.e. $\iint_\Omega \mathscr{F} \, dx \, dy = 0$.
2. The curl of the forcing is zero on the lateral boundaries i.e. $\mathscr{F} = 0$.
3. The forcing contributes zero net zonal impulse i.e. $\iint_\Omega y\mathscr{F} \, dx \, dy = 0$.

We now wish to construct a forcing which is random in time with which we can inject energy into our system at a chosen scale at a constant rate ϵ. This is achieved by employing a function that is white in time and, save for respecting the condition 2 above, is spatially homogeneous and isotropic (e.g. Chekhlov et al. (1996); Lilly (1969); Williams (1978)). This function has zero mean:

$$\langle \mathscr{F} (\mathbf{x}, t) \rangle = 0 \tag{2.6.1}$$

where the angled braces denote an ensemble average. This also satisfies item 1. Its autocorrelation function has the property:

$$\langle \mathscr{F} (\mathbf{x}, t) \, \mathscr{F} (\mathbf{x}, t') \rangle \propto \delta (t - t') \, . \tag{2.6.2}$$

The Fourier transform of $\mathscr{F}(\mathbf{x},t)$ is $F(\mathbf{k},t)$. This has an autocorrelation function of the following form:

$$\langle F(\mathbf{k},t)\, F(\mathbf{k}',t')\rangle = \frac{A}{\pi}\delta\left(k^2 - k_f^2\right)\delta\left(\mathbf{k}+\mathbf{k}'\right)\delta\left(k_y + k_y'\right)\delta\left(t-t'\right), \tag{2.6.3}$$

where A is some amplitude and $k = |\mathbf{k}|$. Because we have assumed $\mathscr{F}(\mathbf{x},t)$ is white in time, so too is $F(\mathbf{k},t)$. The form of this function also tells us that our forcing is isotropic and is concentrated on $k = k_f$ and has conjugate symmetry and is odd about k_y to satisfy item 2. Because the forcing is isotropic and homogeneous, this will also satisfy the assumption of no net zonal impulse (item 3). Integrating over $\mathbf{k}'$ and t' gives

$$\langle F(\mathbf{k},t)\, F(-\mathbf{k},t)\rangle = \frac{A}{\pi}\delta\left(k^2 - k_f^2\right). \tag{2.6.4}$$

We then obtain the enstrophy injection rate ξ by integrating Eq. (2.6.4) over $\mathbf{k}$:

$$\xi = \int \langle F(\mathbf{k},t)\, F(-\mathbf{k},t)\rangle\, d\mathbf{k} = \int_0^\infty A\delta\left(k^2 - k_f^2\right) 2k dk = A. \tag{2.6.5}$$

So we find enstrophy injection rate is given by the amplitude of the variance. The constant energy injection rate ϵ is found by dividing Eq. (2.6.4) by k^2 and integrating over the domain

$$\epsilon = \int \frac{1}{k^2}\langle F(\mathbf{k},t)\, F(-\mathbf{k},t)\rangle\, d\mathbf{k} = \int_0^\infty \frac{1}{k}\xi\delta\left(k^2 - k_f^2\right) 2dk = \frac{\xi}{k_f^2}. \tag{2.6.6}$$

Since our forcing function is stochastic in time, this will convert our barotropic vorticity equation Eq. (2.2.1) into a stochastic differential equation in time, given by the Wiener process

$$d\zeta(\mathbf{x},t) = g(\zeta(\mathbf{x},t))dt + dW(\mathbf{x},t), \tag{2.6.7}$$

where the deterministic part of the equation is given by the function

$$g(\zeta(\mathbf{x},t)) = -u\frac{\partial\zeta}{\partial y} - v\frac{\partial\zeta}{\partial x} - \beta v - D_{\mathrm{B}}\nabla^4\zeta + D_{\mathrm{H}}\nabla^2\zeta - r\zeta, \tag{2.6.8}$$

and the stochastic part is given by

$$dW = \mathscr{F} dt, \tag{2.6.9}$$

where, using Eq. (2.6.2), we have that

$$\langle dW(\mathbf{x},t)\, dW(\mathbf{x}',t')\rangle = dtdt'\langle \mathscr{F}(\mathbf{x},t)\,\mathscr{F}(\mathbf{x},t')\rangle \propto dtdt'\delta\left(t-t'\right). \tag{2.6.10}$$

So ζ is a random variable which evolves according to a deterministic part $g(\zeta)$ and the stochastic process dW. We will generally refer to the deterministic equations Eq. (2.2.1) but will need to consider the stochastic differential equation Eq. (2.6.7) when developing our numerical model.

2.7 Conclusion

In this chapter we have derived the quasi-geostrophic equation given by Eq. (2.1.47) as an asymptotic expansion of the shallow water equations given by Eq. (2.1.37). We have further simplified this by assuming flat bottom topography and a rigid lid approximation to the barotropic vorticity equation given in Eq. (2.2.1). This equation will form the basis of this thesis. We wish to solve Eq. (2.2.1) on a zonally periodic, laterally bounded channel. We have explored two commonly employed sets of boundary conditions which lead to unique solutions of the forced-dissipative equations and satisfy the physical boundary condition Eq. (2.2.3). These conditions are the Dirichlet boundary conditions and a mixture of Neumann conditions on the zonal mean modes and Dirichlet conditions on the non-mean modes. We then examined how these conditions effect key conservation laws of the system. These conservation laws were derived both for the shallow water equations Eq. (2.1.37) and the barotropic vorticity equation Eq. (2.2.1a) and we showed that consistency between the two equations' conservation laws may be achieved via a single integral constraint Eq. (2.3.8) (McWilliams, 1977). This constraint is satisfied by the mixed boundary conditions by setting $\overline{u} = 0$ on the boundaries. We then found the solution to the homogeneous equation for Eq. (2.2.1b) and through this, demonstrated that for this particular domain geometry, Eq. (2.3.8) need not be solved for the Dirichlet boundary conditions as mass conservation Eq. (2.1.53) may be used instead. Finally we introduced a stochastic forcing term so that we could inject energy into our system at a constant rate ϵ, thus converting our deterministic barotropic vorticity equation into a stochastic differential equation given by Eq. (2.6.7).

3

Numerical Model

3.1 Introduction

In the previous section we developed a mathematical model for the barotropic vorticity equation given by Eq. (2.2.1) on a zonally periodic, laterally bounded channel and motivated our choice to use a mixture of Neumann boundary conditions on zonal mean modes and Dirichlet boundary conditions on the non-zonal modes. These boundary conditions, along with the appropriate consistency conditions, required for the barotropic channel model to be consistent with the shallow water channel model, are summarised in Table 2.1. We also introduced a stochastic forcing term of the form Eq. (2.6.3) that injects energy into the system at a constant rate ϵ. We will then need to consider the stochastic differential equation given by Eq. (2.6.7) when evolving ζ in time. In this section we will discuss the model's numerical implementation. This will be dimensional and will span the domain

$$\Omega = \left\{ \left[-\frac{L_x}{2}, \frac{L_x}{2} \right] \times \left[-\frac{L_y}{2}, \frac{L_y}{2} \right] \right\}, \quad (x, y) \in \Omega, \tag{3.1.1}$$

where $L_y = L_x/2$. We will solve our equations of motion using finite differences and spectral methods and time-stepping will be performed using a leap-frog algorithm. Note that the numerical implementation presented here was developed originally by the author for the purposes of this study.

3.2 Spatial Discretisation

The model is spatially discretised with $N_x \times N_y$ grid points where $N_y = N_x/2 + 1$ and we chose N_x to be a power 2 for numerical efficiency when performing a fast Fourier transform (FFT). Here, the additional grid point in y represents the half-grid boxes at the lateral boundaries. So grid boxes in the interior are of size

$$\Delta x = \frac{L_\mathrm{x}}{N_x} = \frac{L_\mathrm{y}}{N_y - 1} = \Delta y, \tag{3.2.1}$$

and at the lateral boundaries the half-grid boxes are of size $\Delta x \times \Delta y/2$. We will also introduce an extra grid point in the x-direction, that is not part of the working domain, to represent the periodic boundary such that

$$f_{i=N_x+1,j} = f_{i=1,j} \tag{3.2.2}$$

where $f_{i,j}$ is some general function evaluated at grid point (i, j). Here, the first index labels grid points in the x-direction and the second index labels grid points in the y-direction. Derivatives are calculated using centred difference stencils and the ghost point method is used at the boundary (see Fig. 3.2.1).

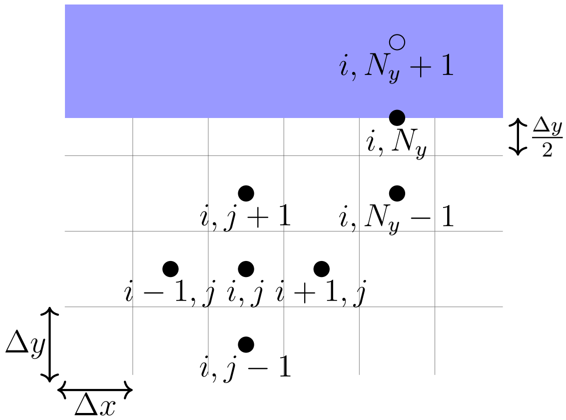

Figure 3.2.1: Labelling for finite difference stencils for calculating derivatives centred on the interior point (i, j) and y-derivatives on the meridional wall (i, N_y), where the grid box is size $\Delta y/2$. The unfilled point $(i, N_y + 1)$ lies outside of the domain but is used to calculate derivatives using the ghost point method.

3.2.1 Advection

To calculate the advective terms in Eq. (2.2.1a) at the grid points (i, j) we must first calculate the zonal and meridional velocities. These are calculated as derivatives of ψ in Eq. (2.2.2a). In the interior, we have

$$v = \frac{\partial \psi}{\partial x} \approx \frac{(\psi_{i+1,j} - \psi_{i-1,j})}{2\Delta x} \tag{3.2.3}$$

and the condition of no normal flow through the boundary walls gives

$$v_{i,J} = 0, \tag{3.2.4}$$

where we use the index J to indicate either the northern boundary $j = N_y$ or the southern boundary $j = 1$. The zonal velocity is given by

$$u = -\frac{\partial \psi}{\partial y} \approx -\frac{(\psi_{i,j+1} - \psi_{i,j-1})}{2\Delta y} = \frac{(\psi_{i,j-1} - \psi_{i,j+1})}{2\Delta y}. \tag{3.2.5}$$

At the boundary we will need to treat the zonal mean mode and non-zonal mean mode of the flow variables separately to obey the mixed boundary conditions summarised in Table 2.1. If we consider the northern boundary which lies at grid point (i, N_y), the centred difference stencil will include a ghost point at $(i, N_y + 1)$. The zonal mean mode $\overline{u}$ at the northern boundary is calculated as

$$\overline{u}_{i,N_y} = \frac{\overline{\psi}_{i,N_y-1} - \overline{\psi}_{i,N_y+1}}{2\Delta y} = 0, \tag{3.2.6}$$

where we have used $\overline{\psi}_{i,N_y+1} = \overline{\psi}_{i,N_y-1}$ in the ghost-point method to respect the Neumann condition $\partial_y \overline{\psi} = 0$. The non-zonal mean mode u' at the northern boundary is given by

$$u'_{i,N_y} = \frac{\psi'_{i,N_y-1} - \psi'_{i,N_y+1}}{2\Delta y} = \frac{\psi'_{i,N_y-1}}{\Delta y}, \tag{3.2.7}$$

where we have used $\psi'_{i,N_y+1} = -\psi'_{i,N_y-1}$ in the ghost-point method to respect the Dirichlet condition $\psi' = 0$. So at the northern boundary we have

$$u_{i,N_y} = \frac{\psi_{i,N_y-1} - \overline{\psi}_{i,N_y-1}}{\Delta y} \tag{3.2.8}$$

and similarly at the southern boundary

$$u_{i,1} = -\frac{\left(\psi_{i,2} - \overline{\psi}_{i,2}\right)}{\Delta y}. \tag{3.2.9}$$

We remark that it is not necessary to calculate the boundary points of u in the temporal evolution of ζ given by Eq. (2.6.7); however we will need these points for data analysis. The first advective term in Eq. (2.2.1) is calculated as

$$u\frac{\partial \zeta}{\partial x} \approx u_{i,j}\left(\frac{\zeta_{i+1,j} - \zeta_{i-1,j}}{2\Delta x}\right), \tag{3.2.10}$$

where $u_{i,j}$ is given by Eq. (3.2.5). At the boundaries, $\zeta' = 0 \implies \zeta_{i,J} = \overline{\zeta}$ for all i so

$$\left.\frac{\partial \zeta}{\partial x}\right|_{i,J} = \frac{\zeta_{i+1,J} - \zeta_{i-1,J}}{2\Delta x} = \frac{\overline{\zeta}_{i+1,J} - \overline{\zeta}_{i-1,J}}{2\Delta x} = 0. \tag{3.2.11}$$

The second advective term is calculated as

$$v\frac{\partial \zeta}{\partial y} \approx v_{i,j}\left(\frac{\zeta_{i,j+1}-\zeta_{i,j-1}}{2\Delta y}\right), \tag{3.2.12}$$

where $v_{i,j}$ is given by Eq. (3.2.3). This term is also zero on the boundaries since $v_{i,J} = 0$. It is not necessary to calculate the advective terms in Eq. (2.2.1) in conservative form because the continuity equation Eq. (2.2.2b) is already satisfied by constructing the velocity components as gradients of ψ. Discretising the advective terms in conservative form may inadvertently violate continuity in the discrete counterparts of the integral constraints outlined in §2.2 by introducing additional terms. For example, in this formulation, the discrete area integrals of Eq. (3.2.10) and Eq. (3.2.12) exactly cancel each other which leads to Eq. (2.3.2) being respected as a discrete level.

3.2.2 Harmonic and Biharmonic Boundary Dissipation

The gradients in the harmonic disspiation term in Eq. (2.2.1a) are calculated on interior points as

$$\nabla^2\zeta \approx \frac{\zeta_{i,j+1}+\zeta_{i,j-1}-2\zeta_{i,j}}{\Delta y^2} + \frac{\zeta_{i+1,j}+\zeta_{i-1,j}-2\zeta_{i,j}}{\Delta x^2}. \tag{3.2.13}$$

To calculate the gradients in the harmonic dissipation on the boundaries we need to consider the zonal mean modes and the non-zonal mean modes separately. The Neumann boundary condition $\partial_y\overline{\zeta} = 0$ is applied to the zonal mean modes at the lateral boundaries: this gives

$$\begin{aligned} \overline{\frac{\partial \zeta}{\partial y}} &\approx \frac{\overline{\zeta}_{i,J+1}-\overline{\zeta}_{i,J-1}}{2\Delta y} = 0, \\ \implies \overline{\zeta}_{i,J+1} &= \overline{\zeta}_{i,J-1} \end{aligned} \tag{3.2.14}$$

and non-zonal mean modes are not evolved on the boundary under Dirichlet boundary conditions, so at the northern boundary

$$\nabla^2\zeta\big|_{i,N_y} = \frac{\overline{\zeta}_{i,N_y+1}+\overline{\zeta}_{i,N_y-1}-2\overline{\zeta}_{i,N_y}}{\Delta y^2} = 2\frac{\overline{\zeta}_{i,N_y-1}-\overline{\zeta}_{i,N_y}}{\Delta y^2} \tag{3.2.15}$$

where $\overline{\zeta}_{i,N_y+1}$ lies outside of the domain. Here we have used that $\overline{\partial_{xx}\zeta}\big|_{i,J} = 0$ along the lateral boundaries. Similarly at the southern boundary

$$\nabla^2\zeta\big|_{i,1} = 2\frac{\overline{\zeta}_{i,2}-\overline{\zeta}_{i,1}}{\Delta y^2}. \tag{3.2.16}$$

The gradients in the biharmonic dissipation are calculated using

$$\nabla^4\zeta = \nabla^2\left(\nabla^2\zeta\right) = \nabla^2\chi, \tag{3.2.17}$$

where $\chi = \nabla^2\zeta$. Interior points are given by

$$\nabla^4\zeta \approx \frac{\chi_{i,j+1} + \chi_{i,j-1} - 2\chi_{i,j}}{\Delta y^2} + \frac{\chi_{i+1,j} + \chi_{i-1,j} - 2\chi_{i,j}}{\Delta x^2}, \tag{3.2.18}$$

where $\chi \approx \chi_{i,j}$ is calculated using Eq. (3.2.13), Eq. (3.2.21) and Eq. (3.2.16). The Neumann boundary condition on the zonal mean of χ is given by

$$\overline{\frac{\partial^3\zeta}{\partial y^3}} = \overline{\frac{\partial\chi}{\partial y}} = 0. \tag{3.2.19}$$

this gives $\overline{\chi}_{i,J+1} = \overline{\chi}_{i,J-1}$ on the lateral boundaries. Non-zonal mean modes are not evolved on the lateral boundaries, so on the northern boundary

$$\nabla^4\zeta\big|_{i,N_y} = \nabla^2\chi\big|_{i,N_y} = 2\frac{\overline{\chi}_{i,N_y-1} - \overline{\chi}_{i,N_y}}{\Delta y^2} \tag{3.2.20}$$

and on the southern boundary

$$\nabla^4\zeta\big|_{i,1} = \nabla^2\chi\big|_{i,1} = 2\frac{\overline{\chi}_{i,2} - \overline{\chi}_{i,1}}{\Delta y^2}, \tag{3.2.21}$$

where we have used $\overline{\partial_{xx}\chi}\big|_{i,J} = \overline{\partial_{xxxx}\zeta}\big|_{i,J} = 0$.

3.3 Poisson Solver

To obtain the streamfunction ψ we must invert the Poisson equation given in Eq. (2.2.1b) which has the general solution given by Eq. (2.4.8). Expanding Eq. (2.2.1b) gives

$$\frac{\partial^2\psi}{\partial x^2} + \frac{\partial^2\psi}{\partial y^2} = \zeta. \tag{3.3.1}$$

We note that in the zonal direction our flow is periodic so we can expand ψ on a Fourier basis. We may write the x-derivatives of ψ in Eq. (3.3.1) as

$$\frac{\partial^2}{\partial x^2}\psi = \frac{\partial^2}{\partial x^2}\left(\hat{\mathcal{F}}\left(\widetilde{\psi}\right)\right) = \hat{\mathcal{F}}\left(-\left(k_x^l\right)^2\widetilde{\psi}\right) \tag{3.3.2}$$

where k_x^l are the discrete Fourier wavenumbers in the x-direction labelled by l. Here, $\hat{\mathcal{F}}$ is the inverse Fourier transform operator in the zonal direction and $\widetilde{\psi}\left(k_x^l, y\right) = \mathcal{F}\left(\psi\right)$ where $\mathcal{F}$ is the forward Fourier transform operator in the zonal direction.

To solve in the meridional direction, we must separate the $k_x^{l=0}$ modes and the

$k_x^{l\neq 0}$ modes in order to obey the Neumann boundary conditions on the zonal mean modes and the Dirichlet boundary conditions on the non-zonal mean modes.

Solving in the y-direction at $k_x^{l=0}$ is most simply achieved using a cosine transform because a cosine basis inherently obeys the Neumann boundary conditions

$$\frac{\partial \overline{\psi}}{\partial y} = \left. \frac{\partial \widetilde{\psi}}{\partial y} \right|_{l=0} = 0. \tag{3.3.3}$$

We may write the y-derivatives of $\widetilde{\psi}$ as

$$\frac{\partial^2}{\partial y^2} \widetilde{\psi} = \frac{\partial^2}{\partial y^2} \left(\hat{\mathcal{C}} \left(\Psi \right) \right) = \hat{\mathcal{C}} \left(- \left(k_y^m \right)^2 \Psi \right) \tag{3.3.4}$$

where k_y^m are the discrete cosine wavenumbers labelled by m. Here, $\hat{\mathcal{C}}$ is the inverse cosine transform operator in the meridional direction and $\Psi \left(k_x^l, k_y^m \right) = \mathcal{C} \left(\mathcal{F} \left(\psi \right) \right)$ where $\mathcal{C}$ is the forward cosine transform operator in the meridional direction. So then taking both the Fourier transform in the x-direction and the cosine transform in the y-direction of Eq. (3.3.1) and rearranging for Ψ gives

$$\Psi = - \frac{Z}{\left(k_x^l \right)^2 + \left(k_y^m \right)^2}, \tag{3.3.5}$$

where $Z \left(k_x^l, k_y^m \right) = \mathcal{C} \left(\mathcal{F} \left(\zeta \right) \right)$.

For modes $k_x^{l\neq 0}$ we solve in the x-direction using the derivative property given by Eq. (3.3.2). We note that by taking the Fourier transform in x we have generated a system of ordinary differential equations for each k_x^l mode in the y-direction given by

$$\left(\frac{d^2}{dy^2} - \left(k_x^l \right)^2 \right) \tilde{\psi} = \tilde{\zeta} \tag{3.3.6}$$

which we solve for $\tilde{\psi}$ for each $k_x^{l\neq 0}$ mode. This, together with our solution at $k_x^{l=0}$ obtained using Eq. (3.3.5), completes our solution for ψ .

Now we implement these solution methods to solve Eq. (3.3.1) numerically as follows. We take an N_x-point fast Fourier transform (FFT) on $\zeta_{i,j}$ along the zonal direction to obtain $\widetilde{\zeta}_{l,j}$, where l labels the discrete Fourier mode in the x-direction. Because ζ is a real-valued function, the discrete Fourier coefficients have conjugate symmetry given by

$$\widetilde{\zeta}_{-l,j} = \widetilde{\zeta}^*_{l,j} \tag{3.3.7}$$

so we only require modes $l \geq 0$ to completely describe the system. Then we separate the $l = 0$ and $l > 0$ modes to solve in the y-direction.

At $l = 0$, the Neumann boundary condition on $\overline{\zeta}$ is given by

$$\frac{\partial \overline{\zeta}}{\partial y} = \frac{\partial}{\partial y} \widetilde{\zeta}_{0,j} = 0. \tag{3.3.8}$$

This allows us to expand $\widetilde{\zeta}_{0,j}$ on a cosine basis. Equivalently, we may use a Fourier basis if we reflect $\widetilde{\zeta}_{0,j}$ about the northern boundary $j = N_y$. In this way, we construct a periodic function $\widetilde{\zeta}^s_{0,j}$ which is 2-fold symmetric about $j = N_y$ and contains $2N_y - 1$ grid points in the y-direction. We can then perform a $2(N_y - 1)$-point FFT on $\widetilde{\zeta}^s_{0,j}$ in the y-direction to obtain $Z^s_{0,m}$ where m labels the Fourier modes in the y-direction. Here, the first $N_y - 1$ Fourier modes are equivalent to the $N_y - 1$ cosine modes in a $(N_y - 1)$-point discrete cosine transform (DCT) on $\widetilde{\zeta}_{0,j}$. We can then obtain $\Psi^s_{0,m}$ from $Z^s_{0,m}$ using the discrete form of Eq. (3.3.5) given by

$$\Psi^s_{0,m} = -\left(\frac{L_y}{\pi}\right)^2 \frac{Z^s_{0,m}}{m^2}. \tag{3.3.9}$$

Here we have used that the Fourier wavenumbers and mode number are related by $k^m_y = m\pi/L_y$ and that $k^{l=0}_x = 0$. We do not solve for $l = 0, m = 0$ but by mass conservation given in Eq. (2.1.53) we may set

$$\Psi_{0,0} = 0. \tag{3.3.10}$$

We then take the $2\,(N_y - 1)$ inverse fast Fourier transform (IFFT) in the y-direction to obtain $\psi^s_{l=0,j}$ which possesses 2-fold symmetry about $j = N_y$. From this we may recover $\psi_{l=0,j}$ by truncating our domain, keeping the first N_y grid points in the y-direction.

For each of the $l > 0$ modes, we solve using the Fourier derivative property in Eq. (3.3.2) in the x-direction. In the y-direction we can solve the remaining $N_x/2 - 1$ ordinary differential equations for $l > 0$ using Eq. (3.3.6). To do this we construct a tridiagonal matrix M that approximates the operator in Eq. (3.3.6) using finite differences:

$$M = \begin{pmatrix} -\left(2 + k_x^2 \Delta y^2\right) & 1 & 0 & \cdots & 0 \\ 1 & -\left(2 + k_x^2 \Delta y^2\right) & 1 & & \vdots \\ 0 & 1 & \ddots & \ddots & \\ \vdots & & \ddots & & 1 \\ 0 & \cdots & & 1 & -\left(2 + k_x^2 \Delta y^2\right) \end{pmatrix}, \tag{3.3.11}$$

where we have defined M only for grid points interior of the lateral boundaries i.e. for $j \neq J$. This is because we need not solve for $\widetilde{\psi}_{i,j\neq 0}$ as these are specified by the Dirichlet boundary conditions where $\psi'_{i,J} = \tilde{\psi}_{l\neq 0,j} = 0$. The resulting system of linear equations are solved as

$$\widetilde{\psi}^T_{l,j} = M^{-1}\left(\Delta y^2 \widetilde{\zeta}_{l,j}\right)^T \tag{3.3.12}$$

for each $l > 0, j \neq J$. From this and our solution at $l = 0$, we recover $\psi_{i,j}$ by taking the IFFT in the x-direction.

3.4 Stochastic Forcing

For forced simulations, we have discussed in §2.6 that we will employ an isotropic, small-scale stochastic forcing term $\mathscr{F}$ which in Fourier space has the form given by Eq. (2.6.3). We construct this forcing function on $N_x \times 2(N_y - 1)$ Fourier coefficients $F_{l,m}$ where l and m label the Fourier modes in the zonal and meridional directions respectively. Of these, the only non-zero coefficients are those that lie within $k_f - 0.5 < k < k_f + 0.5$ where $k = \sqrt{l^2 + m^2}$ and k_f is the forcing scale. We choose to expand our forcing function on a Fourier basis with odd-symmetry in y (or equivalently a sine basis in y) in order to respect our assumption that $\mathscr{F} = 0$ on the lateral boundaries so we are required to set $m = 0$ modes to zero. We also do not force at $l = 0$ which corresponds to the zonal mean mode in physical space because we do not want our forcing to contribute net circulation or impulse. The non-zero Fourier coefficients are assigned values

$$\begin{aligned} F_{l>0,m>0} &= \tilde{A}\exp\left(2\pi i\theta_g\right), \\ F_{-l,m} &= F^*_{l,m}, \\ F_{-l,-m} &= -F^*_{l,m}, \\ F_{l,-m} &= -F_{l,m}, \end{aligned} \tag{3.4.1}$$

where θ_g is a Gaussian random number of unit variance and $\tilde{A}$ is the forcing amplitude chosen such that

$$\iint_\Omega \left\langle \mathscr{F}(\mathbf{x},t)\, \mathscr{F}(\mathbf{x},t)\right\rangle\, dx\, dy \approx \sum_i \sum_j \left\langle \mathscr{F}^2_{ij}\right\rangle \Delta x \Delta y = \xi \tag{3.4.2}$$

where ξ is our chosen enstrophy injection rate. Here, we only assign random Fourier coefficients in the first quadrant as Fourier coefficients in the other quadrants are assigned using symmetry properties. In the x-direction we require that modes obey conjugate symmetry of the form Eq. (3.3.7) and in the y-direction, we require Fourier modes to be odd-symmetric. This ensures that, after performing a $2(N_y - 1)$-point IFFT in y and an N_x-point IFFT in x, the resulting function $\mathscr{F}^s_{ij}$ will be real, periodic in x and odd about $j = N_y$. Then after transforming into physical space, we truncate $\mathscr{F}^s_{ij}$ retaining the first N_y points in the y-direction to obtain our forcing function $\mathscr{F}_{ij}$ to be used in the stochastic differential equation Eq. (2.6.7).

3.5 Time-Stepping

When evolving the barotropic vorticity equation in time, we must consider the stochastic form of the equation given by Eq. (2.6.7). This is discretised in time using the leap-frog method:

$$\zeta_{ij}^{n+1} = \zeta_{ij}^{n-1} - 2\Delta t \left(G_{ij}^{n} - H_{ij}^{n-1}\right) + \sqrt{\Delta t}\left(\mathscr{F}_{ij}^{n-1} + \mathscr{F}_{ij}^{n}\right), \tag{3.5.1a}$$

$$G_{ij} = u_{ij} \left.\frac{\partial \zeta}{\partial x}\right|_{ij} + v_{ij} \left.\frac{\partial \zeta}{\partial y}\right|_{ij} + \beta v_{ij} + r\zeta_{ij}, \tag{3.5.1b}$$

$$H_{ij} = D_{\mathrm{H}}\, \nabla^2\zeta\big|_{ij} - D_{\mathrm{B}}\, \nabla^4\zeta\big|_{ij}, \tag{3.5.1c}$$

where the superscript n labels the n^{th} time-step and Δt is the time increment such that the time after n time-steps is given by $t^n = n\Delta t$. Here, G_{ij} are the terms evaluated at t^n and H_{ij} are the diffusive terms evaluated at t^{n-1}. These have been lagged because they are unconditionally unstable in the leapfrog scheme. $\mathscr{F}(\mathbf{x}, t)$ is non-integrable in time but we may discretise this using statistical considerations which introduce the $\sqrt{\Delta t}$ factor. We also use that in one iteration of the leapfrog scheme, the random variable ζ has been forced twice at t^n and t^{n+1}. The model is forward stepped at $n = 0$:

$$\zeta_{ij}^{n+1} = \zeta_{ij}^{n} - \Delta t \left(G_{ij}^{n} - H_{ij}^{n}\right) + \sqrt{\Delta t}\mathscr{F}_{ij}^{n}. \tag{3.5.2}$$

The model is also forward stepped when and when t^n is a multiple of 3 hrs to avoid coupling between time-steps and odd time-steps. A number of stability criteria apply to the discretisations Eq. (3.5.1) (Cushman-Roisin and Beckers, 2011). Since $\Delta x = \Delta y$ in our discretisation, the advection terms in the leapfrog method are stable subject to the Courant-Friedrichs-Lewy (CFL) conditions

$$c\frac{\Delta t}{\Delta x} \leq \frac{1}{2} \tag{3.5.3}$$

where c is the magnitude of the maximum velocity in the domain. Using the leapfrog scheme allows the CFL conditions to be respected up to the equality, such that the highest resolution possible may be used for a given time-step. The diffusive terms are stable in Eq. (3.5.1) if, following (Griffies and Hallberg, 2000),

$$\mathcal{D}_{\mathrm{H}}\frac{\Delta t}{\Delta x^2} \leq \frac{1}{8}, \tag{3.5.4a}$$

$$\mathcal{D}_{\mathrm{B}}\frac{\Delta t}{\Delta x^4} \leq \frac{1}{64}. \tag{3.5.4b}$$

3.6 Conclusion

In this chapter we have presented a numerical discretisation for the barotropic channel model developed in §2.2. We have discretised our equations spatially and have calculated derivatives using finite differences and have used a mixture of finite differences and spectral methods for inverting the Poisson equation given by Eq. (2.2.1b). Zonal mean modes of ζ have been treated at the boundaries using Neumann boundary conditions and non-mean modes have been treated at the boundaries using Dirichlet conditions. We have also presented the leapfrog and forward Euler method for evolving our model in time. All simulations in this thesis will be performed using this model.

4

Eddy Tilts

4.1 Introduction

Spontaneous jet formation is the hallmark of geostrophic turbulence and has been witnessed in numerous numerical studies (e.g. Chekhlov et al. (1996); Sukoriansky and Galperin (2005); Vallis and Maltrud (1993); Williams (1978)) confirming, at least broadly, the theory of jet formation set out in Rhines (1975). We know that the onset of Rossby wave propagation anisotropises the spectral evolution of the energy density such that zonal modes are favoured. In physical space, this manifests as eddies zonally elongating and forming into zonal jets. In the presence of large scale dissipation, the flow may reach statistical stationarity such that the zonal structure persists in the zonal and time mean and is supported by a flux of eddy momentum. What is unclear is how the excitation of Rossby-waves arranges the underlying eddy momentum stresses to support the mean flow structures.

To examine eddy momentum stresses, we Reynolds average our equations to describe the relationship between the Reynolds stresses and the mean flow. We then perform a principle component analysis of the eddy velocity correlation tensor, which allows us to define an eddy variance ellipse (Preisendorfer, 1988). The geometric properties of this ellipse encode the structure of the local eddy momentum stresses and is thus a useful tool for visualising Reynolds stress patterns and their interactions with the mean flow (Hoskins et al., 1983; Maddison and Marshall, 2013; Marshall et al., 2012; Wilkin and Morrow, 1994). Recently, this framework has been used to describe eddy-mean flow interactions in western boundary jets (Waterman and Hoskins, 2013; Waterman and Lilly, 2015) and to examine the growth and decay of shear instabilities in (Tamarin et al., 2016). We will delve further into the application of this formulation to the fully turbulent problem later in this thesis. In this chapter, we will begin by introducing the Reynolds averaged equations and the geometric eddy ellipse formulation. We will then illustrate its virtues in studying eddy-mean flow interactions by applying this to a perturbed barotropically unstable jet, reproducing analysis in Tamarin et al. (2016).

4.2 Reynolds Stresses

Reynolds averaging is a statistical approach formulated by Reynolds (1895) that has become a staple of turbulence studies. In this formulation, turbulence is described as a mean flow with a fluctuating component. In general, this mean is defined as the ensemble average of N individual flow realisations $f(\mathbf{x}, t)$

$$\langle f(\mathbf{x}, t)\rangle = \lim_{N\to\infty} \frac{1}{N} \sum_{n=1}^{N} f_n(\mathbf{x}, t), \tag{4.2.1}$$

where angled braces denote the ensemble mean. The ergodic hypothesis observes that systems exhibiting certain symmetries will result in an equivalence between the ensemble mean and some other mean property of the flow. For example, flows which are statistically stationary allow us to use the temporal average as the ensemble average or if the flow is spatially homogeneous we may wish to use a spatial average. For now we will continue our formulation using an ensemble average and later motivate our choice in averaging. We begin with the shallow water equations:

$$\frac{\partial \mathbf{u}}{\partial t} + (\mathbf{u}\cdot\boldsymbol{\nabla})\,\mathbf{u} + \mathbf{f}_{\mathrm{h}} = -g\boldsymbol{\nabla}\eta + \mathbf{D}, \tag{4.2.2a}$$

$$\boldsymbol{\nabla}\cdot\mathbf{u} = 0, \tag{4.2.2b}$$

where we have assumed that the fluid thickness $h =$ constant and here, $\mathbf{D}$ represents the linear non-conservative forcing and dissipation terms in Eq. (2.1.37). We now express flow variables as sums of their ensemble means and fluctuations which are defined as departures from the mean:

$$\mathbf{u} = \langle\mathbf{u}\rangle + \mathbf{u}', \quad \eta = \langle\eta\rangle + \eta', \quad \mathbf{f}_{\mathrm{h}} = \langle\mathbf{f}_{\mathrm{h}}\rangle + \mathbf{f}_{\mathrm{h}}' \quad \mathbf{D} = \langle\mathbf{D}\rangle + \mathbf{D}', \tag{4.2.3}$$

where angled brackets and primes denote the ensemble mean and fluctuating components respectively. We perform Reynolds' averaging by substituting Eq. (4.2.3) into Eq. (4.2.2) and taking the ensemble average of the resulting equations

$$\frac{\partial\langle\mathbf{u}\rangle}{\partial t} + (\langle\mathbf{u}\rangle\cdot\boldsymbol{\nabla})\langle\mathbf{u}\rangle + \langle(\mathbf{u}'\cdot\boldsymbol{\nabla})\,\mathbf{u}'\rangle + \langle\mathbf{f}_{\mathrm{h}}\rangle = -g\boldsymbol{\nabla}\langle\eta\rangle + \langle\mathbf{D}\rangle, \tag{4.2.4a}$$

$$\boldsymbol{\nabla}\cdot\langle\mathbf{u}\rangle = 0, \tag{4.2.4b}$$

where we have used that the differential operator and averaging operators are linear and hence commutable. We observe that the mean of the product of the two fluctuating velocity components is not necessarily zero. The x-components and

y-components of these fluctuating terms may be written

$$\langle (\mathbf{u}' \cdot \boldsymbol{\nabla})\, u' \rangle = \frac{\partial}{\partial x} \langle u'u' \rangle + \frac{\partial}{\partial y} \langle u'v' \rangle \,, \tag{4.2.5a}$$

$$\langle (\mathbf{u}' \cdot \boldsymbol{\nabla})\, v' \rangle = \frac{\partial}{\partial y} \langle v'v' \rangle + \frac{\partial}{\partial x} \langle u'v' \rangle \,, \tag{4.2.5b}$$

where we have used that $\boldsymbol{\nabla} \cdot \mathbf{u}' = 0$. The terms under the differentials are Reynolds stresses. They form the components of the eddy velocity correlation tensor:

$$\mathbf{Q}' \equiv \begin{pmatrix} \langle u'u' \rangle & \langle u'v' \rangle \\ \langle u'v' \rangle & \langle v'v' \rangle \end{pmatrix}. \tag{4.2.6}$$

The Reynolds' stresses describe the extent to which the eddy velocity component u_i' covaries with u_j'. When $\left\langle u_i' u_j' \right\rangle \neq 0$, these components are correlated whereas when $\left\langle u_i' u_j' \right\rangle = 0$ they are uncorrelated. Note that in obtaining the Reynolds' averaged equations given by Eq. (4.2.4), we have introduced additional unknowns given by Eq. (4.2.5) without introducing additional equations. Producing new equations by considering the higher moments of Eq. (4.2.4) in turn generates additional unknowns such that there are always more unknowns than equations. This is the closure problem of turbulence which, from a physical perspective is unsurprising since no additional physical constraints have been introduced in this process.

The divergence of the Reynolds stresses $\partial_i \left\langle u_i' u_j' \right\rangle$ given by Eq. (4.2.5) tell us how the i^{th} component of the momentum fluxes the j^{th}. Thus Eq. (4.2.4) describes the interactions between the eddy momentum fluxes given by the divergence of Eq. (4.2.6) and the mean flow. Finally, since we will be using a zonally periodic channel model, the natural choice for averaging will be in the zonal direction and the fluctuating quantities in this thesis will be those that are departures from the zonal mean.

4.3 Eddy Variance Ellipses

The Reynolds decomposed inviscid, unforced shallow water momentum equation is given by

$$\frac{\partial \overline{\mathbf{u}}}{\partial t} + \overline{\mathbf{f}_{\mathrm{h}}} = -\boldsymbol{\nabla} \cdot \mathbf{T} - g \boldsymbol{\nabla} \overline{\eta}, \tag{4.3.1}$$

where we have assumed that the ensemble average is equivalent to the zonal mean which is denoted by an overline. The advective terms vanish upon zonal averaging. We have found that eddies influence the mean-flow through the divergence of the eddy velocity correlation tensor:

$$\mathbf{T} = \mathbf{T}\,(y) = \begin{pmatrix} \overline{u'u'} & \overline{u'v'} \\ \overline{u'v'} & \overline{v'v'} \end{pmatrix}. \tag{4.3.2}$$

Eq. (4.3.2) maybe separated into isotropic (trace-only) and anisotropic (trace-free) parts:

$$\mathbf{T} = K\mathbf{I} + \mathbf{E}, \tag{4.3.3}$$

where $\mathbf{I}$ is the identity and the zonally averaged kinetic energy density associated with the eddying portion of the flow field is given by

$$K = K\,(y) = \frac{1}{2}\left(\overline{u'^2} + \overline{v'^2}\right), \tag{4.3.4}$$

and we have introduced the eddy momentum stress tensor

$$\mathbf{E} = \begin{pmatrix} M & N \\ N & -M \end{pmatrix}. \tag{4.3.5}$$

Here, we introduce the normal stress difference

$$M = M\,(y) = \frac{1}{2}\left(\overline{u'^2} - \overline{v'^2}\right). \tag{4.3.6}$$

If the eddying portion of the flow is mostly meridional then $M < 0$ whereas if it is mostly zonal then $M > 0$. The shear stress is given by

$$N = N\,(y) = \overline{u'v'}. \tag{4.3.7}$$

The Reynolds averaged inviscid unforced form of the barotropic vorticity equation given by Eq. (2.2.1) is:

$$\frac{\partial \overline{\zeta}}{\partial t} = -\boldsymbol{\nabla} \cdot \left(\overline{\mathbf{u}'\zeta'}\right), \tag{4.3.8}$$

where eddies influence the mean flow in the barotropic vorticity equation through the divergence of an eddy vorticity flux $\overline{\mathbf{u}'\zeta'}$. We can relate Eq. (4.3.2) to the zonal mean eddy vorticity flux in the barotropic vorticity equation Eq. (4.3.8). We obtain the zonal averaged Reynolds decomposed quasi-geostrophic equation by taking ∂_y of the zonal component of Eq. (4.3.1) and subtracting this from ∂_x of the meridional component. Comparing this to Eq. (4.3.8) we find

$$\boldsymbol{\nabla} \cdot \left(\overline{\mathbf{u}'\zeta'}\right) = -2\frac{\partial^2}{\partial x \partial y}M + \frac{\partial^2}{\partial x^2}N - \frac{\partial^2}{\partial y^2}N. \tag{4.3.9}$$

So we see that only the components of the eddy momentum stress tensor given by Eq. (4.3.5) explicitly appear in the eddy forcing of the mean barotropic vorticity equation. From this, it is straightforward to show that

$$\overline{\mathbf{u}'\zeta'} = \left(-\frac{\partial M}{\partial y}, -\frac{\partial N}{\partial y}\right), \tag{4.3.10}$$

which is the well known Taylor-Bretherton identity (Bretherton, 1966; Plumb, 1986; Taylor, 1915). We also note that since $\overline{v} = 0$, the dynamical evolution of Eq. (4.3.1) is governed by

$$\frac{\partial \overline{u}}{\partial t} = -\frac{\partial N}{\partial y}. \tag{4.3.11}$$

We have discussed that the Reynolds' stresses are correlations between eddy velocities u' and v'. If there are strong correlations, an ellipse pattern will be traced in the space $u' - v'$ and if no correlations exist the trace will be circular. We can recover these ellipse properties from the covariance tensor given by Eq. (4.3.2) by performing a principle axes decomposition (Preisendorfer, 1988). If a is the semimajor axis and b is the semiminor axes of the ellipse, we can rotate this ellipse through an angle θ so that a aligns with the x-direction and b aligns with the y-direction. This is achieved by diagonalising Eq. (4.3.5) under a rotation (Waterman and Lilly, 2015):

$$\begin{aligned}
\begin{pmatrix} \overline{u'u'} & \overline{u'v'} \\ \overline{u'v'} & \overline{v'v'} \end{pmatrix} &= \begin{pmatrix} \cos\theta & -\sin\theta \\ \sin\theta & \cos\theta \end{pmatrix} \begin{pmatrix} a^2 & 0 \\ 0 & b^2 \end{pmatrix} \begin{pmatrix} \cos\theta & -\sin\theta \\ \sin\theta & \cos\theta \end{pmatrix}^{\mathrm{T}}, \\
&= \begin{pmatrix} a^2\cos^2\theta + b^2\sin^2\theta & (a^2-b^2)\sin\theta\cos\theta \\ (a^2-b^2)\sin\theta\cos\theta & a^2\sin^2\theta + b^2\cos^2\theta \end{pmatrix}.
\end{aligned} \tag{4.3.12}$$

Comparing this to terms in Eq. (4.3.3), we find that

$$\begin{aligned}
K &= \frac{1}{2}\left(\overline{u'u'} + \overline{v'v'}\right) = \frac{1}{2}\left(a^2 + b^2\right), \\
M &= \frac{1}{2}\left(\overline{u'u'} - \overline{v'v'}\right) = \frac{1}{2}\left(a^2 - b^2\right)\cos 2\theta, \\
N &= \overline{u'v'} = \frac{1}{2}\left(a^2 - b^2\right)\sin 2\theta.
\end{aligned} \tag{4.3.13}$$

We can now rewrite Eq. (4.3.5) as

$$\mathbf{E} = L \begin{pmatrix} \cos 2\theta & \sin 2\theta \\ \sin 2\theta & -\cos 2\theta \end{pmatrix}, \tag{4.3.14}$$

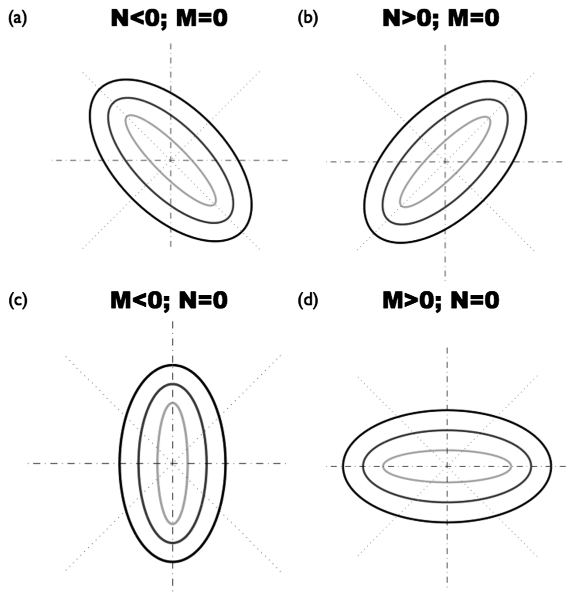

Figure 4.3.1: Eddy ellipse orientations corresponding to $\theta = -\frac{\pi}{4}$ (a), $\theta = \frac{\pi}{4}$ (b), $\theta = \frac{\pi}{2}$ (c) and $\theta = 0$. K determines the magnitude of the eddy ellipse and increases from light grey to black. Figure adapted from Waterman and Hoskins (2013).

where we have defined

$$L = L(y) = \frac{1}{2}\left(a^2 - b^2\right) = \sqrt{M^2 + N^2}. \tag{4.3.15}$$

Here L is the excess energy in the direction of the major axis of the ellipse compared to the minor and θ is given by:

$$\theta = \theta(y) = \frac{1}{2}\arctan\left(\frac{N}{M}\right), \tag{4.3.16}$$

which is the tilt of the ellipse with respect to the zonal direction. The geometric eddy ellipse is not a description of the shape of individual eddies themselves but a description of their average stresses. Through examining the distribution of eddy ellipses, and observing their patterns, we can determine the direction and magnitude of any resulting fluxes. Special cases of ellipse orientations are illustrated in Fig. 4.3.1. Flows may demonstrate significant anisotropy between the zonal and meridional component of their flow velocities such that $M \neq 0$, but this may not necessarily give rise to a zonal momentum tendency. This kind of behaviour corresponds to neutral ellipse tilts, where $N = 0$. Conversely, when $M = 0$ flow velocities do not demonstrate any significant anisotropy between the zonal and meridional components, but there may be a zonal momentum tendency where $N \neq 0$. An eddy ellipse tilted at $\theta = \pm\frac{\pi}{4}$ is achieved in this instance. By examining the eddy ellipse shapes, we can tell which eddy distributions give rise to momentum

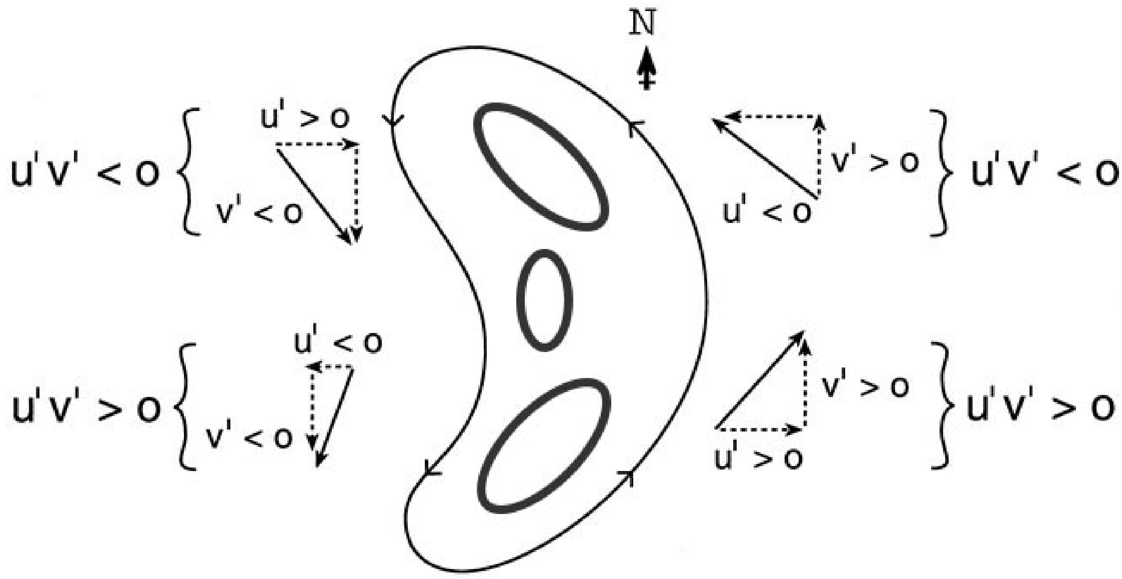

Figure 4.3.2: A banana shaped eddy in which momentum converges at the centre of the eddy, giving rise to an eastward momentum flux. The sign of $u'v'$ at the north and south of the eddy is also shown. These zonally average to give $N < 0$ and $N > 0$ at the northern and southern sides of the eddy respectively. We have also inferred the variance ellipse shapes at three meridional positions along the eddy. This distribution of variance ellipses visualises the convergence zone in the centre of the eddy. Figure adapted from Wardle and Marshall (2000).

fluxes and which do not. An example of an eddy shape that demonstrates a zonal momentum flux and these special cases of eddy ellipse shapes, is the banana shaped eddy depicted in Fig. 4.3.2 (Wardle and Marshall, 2000). Here the eddy shape is such that momentum is fluxed eastward. At the northward flank of the eddy, $M \approx 0$ and $N < 0$, this corresponds to an eddy ellipse with $\theta \approx -\pi/4$. In the middle of the eddy, $M < 0$ and $N = 0$, this corresponds to an eddy ellipse with $\theta \approx -\pi/2$. At the south of the eddy, $M \approx 0$ and $N > 0$, this corresponds to an eddy ellipse with $\theta \approx \pi/4$. Examining the distribution of the geometric ellipses visualises these flux directions more intuitively than examining the velocities. Circular eddy ellipse are only achieved when $M = 0$ and $N = 0$ and there is no significant anisotropy, either through correlations between u' and v' or where $\overline{u'u'} \neq \overline{v'v'}$. In this scenario, only the isotropic component of the tensor given by Eq. (4.3.3) remains. Examples of other eddy ellipse distributions that given rise to zonal momentum fluxes can be found in Fig. 3 and Fig. 4 of Tamarin et al. (2016).

4.4 Shear Instabilities on a Zonal Jet

To demonstrate how we might use the variance ellipse tool in order to elucidate the nature of eddy-mean flow interactions, we will follow the analysis in Tamarin et al. (2016) and examine the interactions between shear instabilities and a barotropically unstable jet.

4.4.1 Background

Consider a piece-wise linear shear consisting of two equal and opposite signed vorticity strips

$$\overline{\zeta}(y) = \begin{cases} 0,\ y \geq b, \\ \Lambda,\ 0 < y < b, \\ -\Lambda,\ -b < y < 0, \\ 0,\ y \leq b, \end{cases} \tag{4.4.1}$$

where Λ is the shear and b is the width of the shear strip. This profile satisfies the necessary condition for barotropic instability given by the Rayleigh-Kuo stability criterion, where the quantity

$$\beta - \frac{\partial \overline{\zeta}}{\partial y}, \tag{4.4.2}$$

is required to change sign somewhere within the domain, where we have used $\overline{\zeta} = \partial_y \overline{u}$. For our setup, this occurs at the shear interfaces $y = 0, \pm b$. Following the analysis in Heifetz et al. (1999) for the growth of instabilities of Eq. (4.4.1) in an infinite domain, Tamarin et al. (2016) demonstrated that on the f-plane the normal mode solutions to the perturbed system results in the growth of phase locked $n = 3$ solutions at each interface $y = 0, \pm b$ and that solutions on the β-plane were qualitatively similar. We will proceed by perturbing a jet with profile Eq. (4.4.1), examining the evolution of the instabilities and analysing their interactions with the mean flow using the geometric decomposition.

4.4.2 Model

The governing equation is the quasi-geostrophic equation, similar to that which we derived in §2.2 given by Eq. (2.2.1), without an external forcing term:

$$\frac{\partial \zeta}{\partial t} = -u\frac{\partial \zeta}{\partial x} - v\frac{\partial \zeta}{\partial y} - \beta v + D_{\mathrm{H}}\nabla^2\zeta - D_{\mathrm{B}}\nabla^4\zeta - r_0\left(\zeta - \zeta_{\mathrm{eq}}\right). \tag{4.4.3}$$

The parameters used here were $\beta = 2 \times 10^{-11}$ $(\mathrm{ms})^{-1}$, $D_{\mathrm{H}} = 1.06$ $\mathrm{m^2s^{-1}}$, $D_{\mathrm{B}} = 5 \times 10^7$ $\mathrm{m^4s^{-1}}$ and $r_0 = 3.48 \times 10^{-17}$ $\mathrm{s^{-1}}$, where r_0^{-1} is the relaxation time-scale. The background flow ζ_{eq} approximates the piece-wise linear jet given by Eq. (4.4.1) and is given by

$$\zeta_{\mathrm{eq}} = \frac{\Lambda}{2}\left[2\tanh\left(\frac{y}{d}\right) - 2\tanh\left(\frac{y+b}{d}\right) - 2\tanh\left(\frac{y-b}{d}\right)\right], \tag{4.4.4}$$

which is differentiable, where $\Lambda = \frac{U_{\max}}{b}$, $U_{\max} = 0.24$ ms^{-1} is the maximum velocity corresponding to the equilibrium jet profile and $b = 75$ km is the half-width of the shear and $d = 0.05b$ determines the smoothness of the transition region. The system is perturbed with random noise at 2.26% of the energy of the initial condition. The model[1] is solved on a 257×129 grid of points on a periodic channel with extent $L_x = 450$ km and $L_y = 900$ km in the zonal and meridional directions respectively giving a resolution of $\Delta x = \Delta y = 3.5156$ km. The model was evolved for $t = 10,000$ hrs with a time-step $\Delta t = 56.25$ s.

The relaxation term is the key difference between Eq. (4.4.3) and Eq. (2.2.1). A scaling analysis of the terms appearing in Eq. (4.4.3) reveals the relaxation term to be very small in comparison to other terms in the system

$$\begin{aligned} u\frac{\partial \zeta}{\partial x} \sim \ v\frac{\partial \zeta}{\partial y} \sim \frac{U_{\max}\Lambda}{b} &\sim 1 \times 10^{-11} \ \mathrm{s}^{-2}, \\ -\beta v \sim \beta U_{\max} &\sim 5 \times 10^{-12} \ \mathrm{s}^{-2}, \\ D_{\mathrm{H}}\nabla^2\zeta \sim \frac{D_{\mathrm{H}}\Lambda}{b^2} &\sim 1 \times 10^{-16} \ \mathrm{s}^{-2}, \\ D_{\mathrm{B}}\nabla^4\zeta \sim \frac{D_{\mathrm{B}}\Lambda}{b^4} &\sim 1 \times 10^{-17} \ \mathrm{s}^{-2}, \\ r_0\left(\zeta - \zeta_0\right) \sim r_0\Lambda &\sim 1 \times 10^{-22} \ \mathrm{s}^{-2}. \end{aligned} \tag{4.4.5}$$

However, a comparison of the flow fields evolved with $r_0 = 0$ shows that this term is necessary for linearising the flow. These order of magnitude estimates do not account for the steep gradients introduced by the jet profile given by Eq. (4.4.4) which may result in terms being of more comparable size. We will initially perform diagnostics for the case in which $r_0 \neq 0$, as was done in Tamarin et al. (2016) and then will switch off this term to examine a more turbulent case.

4.4.3 Results

Linearised System

Fig. 4.4.1 shows the zonal mean jet velocity and potential vorticity at different stages in the flow evolution when $r_0 \neq 0$ and the flow is kept (initially) linearised. At $t = 0$ hrs, the jet is sharp and has a profile that satisfies the instability criterion Eq. (4.4.2) at the interfaces $y = \pm b$. As the perturbations grow, the jet flattens coinciding with the weakening of the PV gradients and the jet begins to approach a more stable configuration. At later times the jet sharpens coinciding with stronger

[1]Initially the model was set up using the parameters reported in Tamarin et al. (2016) with $L_x = 436$ km, $D_{\mathrm{H}} = 106$ m^{2}s^{-1} and $r_0 = 5.2 \times 10^{-7}$ s^{-1}, however these produced highly diffusive runs in which instabilities did not evolve beyond their initial growth period. Following discussions with the lead author, we found that the parameters reported in Tamarin et al. (2016) were incorrect. Those presented here are correct.

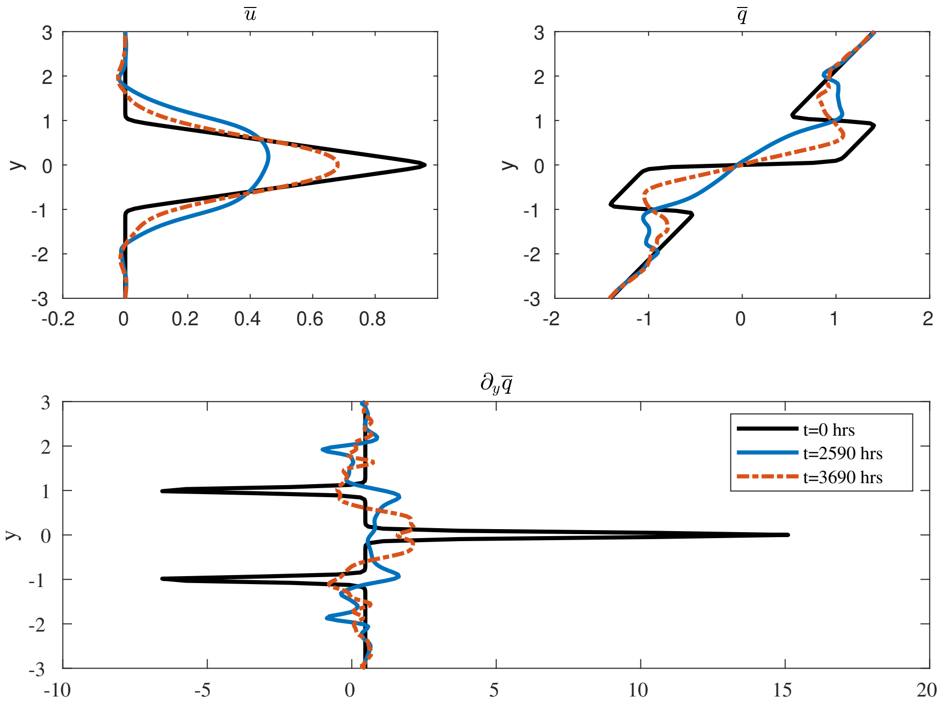

Figure 4.4.1: (Top left) zonal mean velocity normalised by $U_{\max}$, (top right) zonal mean potential vorticity normalised by Λ and (bottom) zonal mean potential vorticity gradient normalised by Λb^{-1} at different times over the flow evolution.

PV gradients and a more unstable configuration. To understand this behaviour we examine the PV-fields in Fig. 4.4.2 which shows how the instabilities develop prior to the system obtaining the profile at $t = 2590$ hrs which is consistent with the analytical normal mode solutions for a jet with shear as given by Eq. (4.4.1) on the f-plane. These illustrate that the system picks out the most unstable $n = 3$ normal mode solution which initially grows and is tilted against the shear. At $t = 2590$ hrs the instabilities cease to grow in Fig. 4.4.2b which coincides with the time at which the velocity profile of the jet has been minimised. This occurs because the instabilities are extracting momentum from the mean flow which causes the flattening of the jet profile. The jet then reaches a more stable configuration that cannot support the perturbations any longer and the instabilities must now begin to decay. The system achieves this by tilting the instabilities towards the shear as in Fig. 4.4.2c, this allows them to begin relinquishing their momentum to the mean flow. As this occurs, the jets sharpen again. The flow then becomes more barotropically unstable and the system, once again, favours the growth of instabilities. This process of oscillating between growth and decay appears to repeat until the perturbations die off.

We may obtain the implied eddy ellipses by producing scatterplots of $u' - v'$

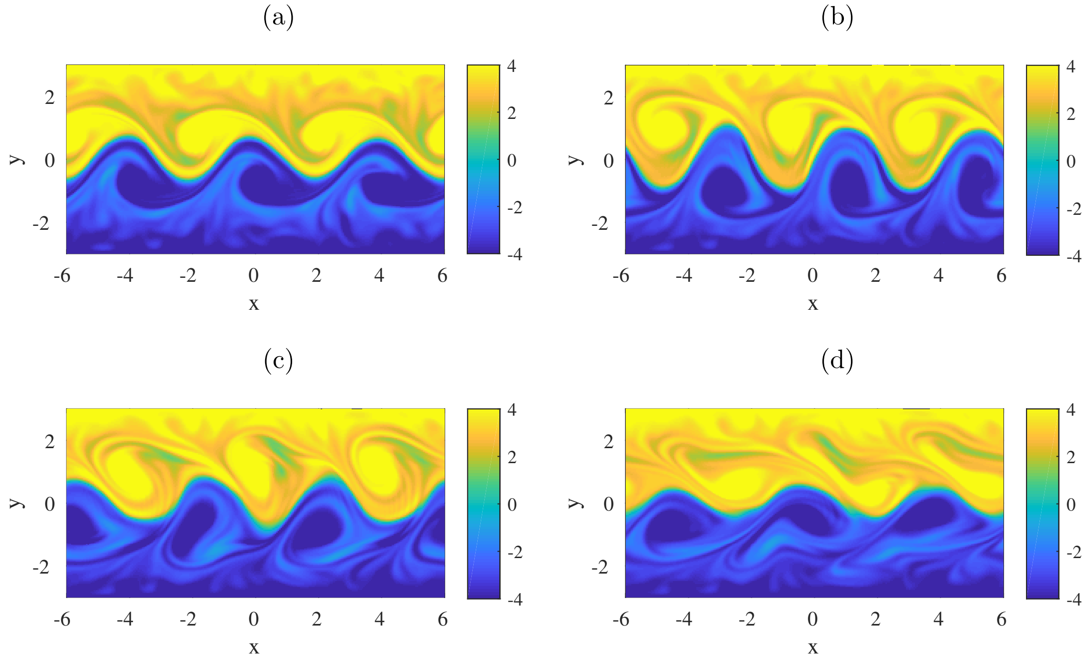

Figure 4.4.2: Snapshot of the potential vorticity $q/10^6$ s^{-1} at different stages of flow evolution. The flow picks out the most unstable mode, $n = 3$. At $t = 2040$ hrs (a), these instabilities are tilted towards the shear. At $t = 2590$ hrs (b) instabilities begin tilting in the opposite direction until at $t = 3140$ hrs (c) instabilities are tilted against the shear. At $t = 3690$ hrs (d) the instabilities are becoming more turbulent. The coordinates (x, y) are normalised by b.

at the shear interfaces $y = \pm b, 0$ as shown in Fig. 4.4.3, where the instabilities are present. At $t = 2040$ hrs the ellipses at $y = \pm b$ show tilt angles which are oriented against the shear whilst within the jet core at $y = 0$, the tilt is $\pi/2$, consistent with Fig. 4.4.2a. This eddy ellipse pattern suggests that momentum is being fluxed away from the jet core and is strengthening the eddies. When the jet profile reaches its first minimum at $t \approx 2590$ hrs, the ellipses on the jet flanks are tilted to $\pi/2$ indicative of there being no momentum flux and strong zonal motion. Later on at $t = 3140$ hrs the eddy ellipse tilts at $y = \pm b$ are oriented with the shear on the jet flanks which suggests that momentum is now being fluxed towards the jet core by the instabilities.

Hovmöller plots of eddy ellipse parameters N, M and θ are presented in Fig. 4.4.4, showing their evolution in time. Initially we see the growth of a positive flux of momentum N at $y = b$ and a negative flux of momentum at $y = -b$ in Fig. 4.4.4a, with no momentum flux at $y = 0$. A diverging momentum flux pattern like this indicates that momentum is being fluxed away from the mean flow. The corresponding Hovmoller plot of the tilt angles Fig. 4.4.4c shows slabs of $\theta = \pi/4$ and $\theta = -\pi/4$ on the northern and southern jet flanks

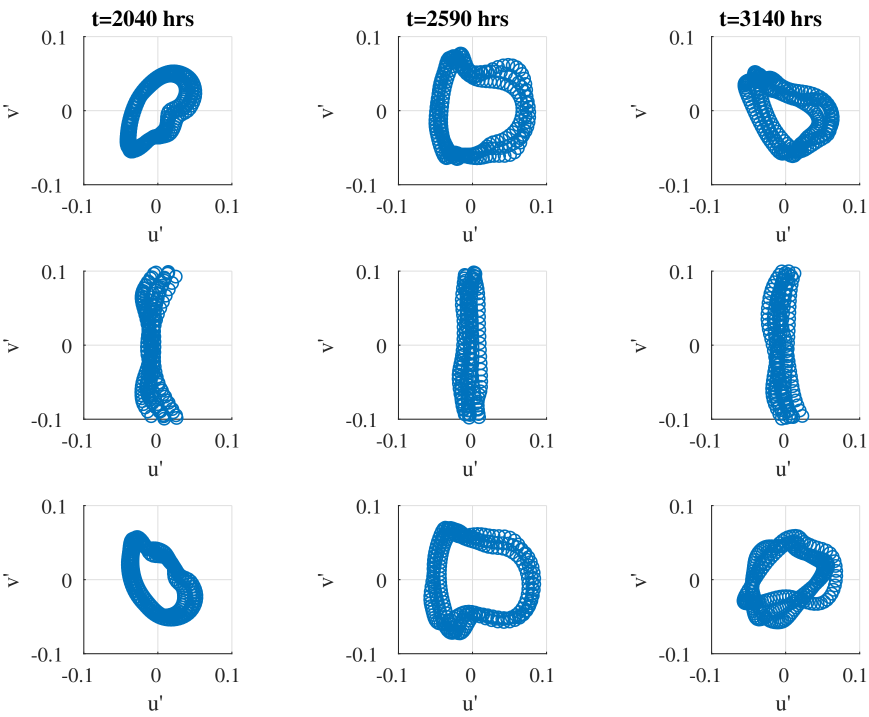

Figure 4.4.3: Scatter plots of (u', v') at different times and meridional locations, from top to bottom, at $y \approx b$, $y = 0$ and $y \approx -b$. Scatter plots of (u', v'), tracing the variance ellipses corresponding to Fig. 4.4.2a, Fig. 4.4.2b and Fig. 4.4.2d at meridional locations (top row) $y/b \approx 1$, (central row) $y/b = 0$ and (bottom row) $y/b \approx -1$.

respectively. This is consistent with the scatterplots of $u' - v'$ in Fig. 4.4.3 at $t \approx 2040$ hrs, which suggest a positive and negative tilt at the north and south interfaces respectively. These reinforce our previous observation that at this stage in the evolution, momentum is being fluxed away from the jet core as the instabilities grow.

As the flow evolves, the momentum fluxes at $y = \pm b$ start to vanish and reach 0 at $t = 2590$ hrs. This coincides with the slabs of $\theta \pm \frac{\pi}{4}$ starting to thin and θ approaches $\frac{\pi}{2}$, across the extent of the shear layers from $y = -b$ to $y = b$. At this point, M reaches its maximal value within the jet core demonstrating that eddies are zonally elongating in this region. This coincides with the time the maximum velocity of the jet profile shown in Fig. 4.4.1 is minimised.

Later on in the flow evolution, the momentum fluxes on the jet flanks begin to grow again to maximum, but now with opposite sign to the previous growth period. Momentum is now converging within the jet core. The tilt angles also flip with θ leaning into the shear on the jet flanks which is again consistent with the tilt-angle the scatterplots of $u' - v'$ at $t \approx 3140$ hrs. This is followed later on in the flow evolution by the sharpening of the jet profile shown in Fig. 4.4.1. After

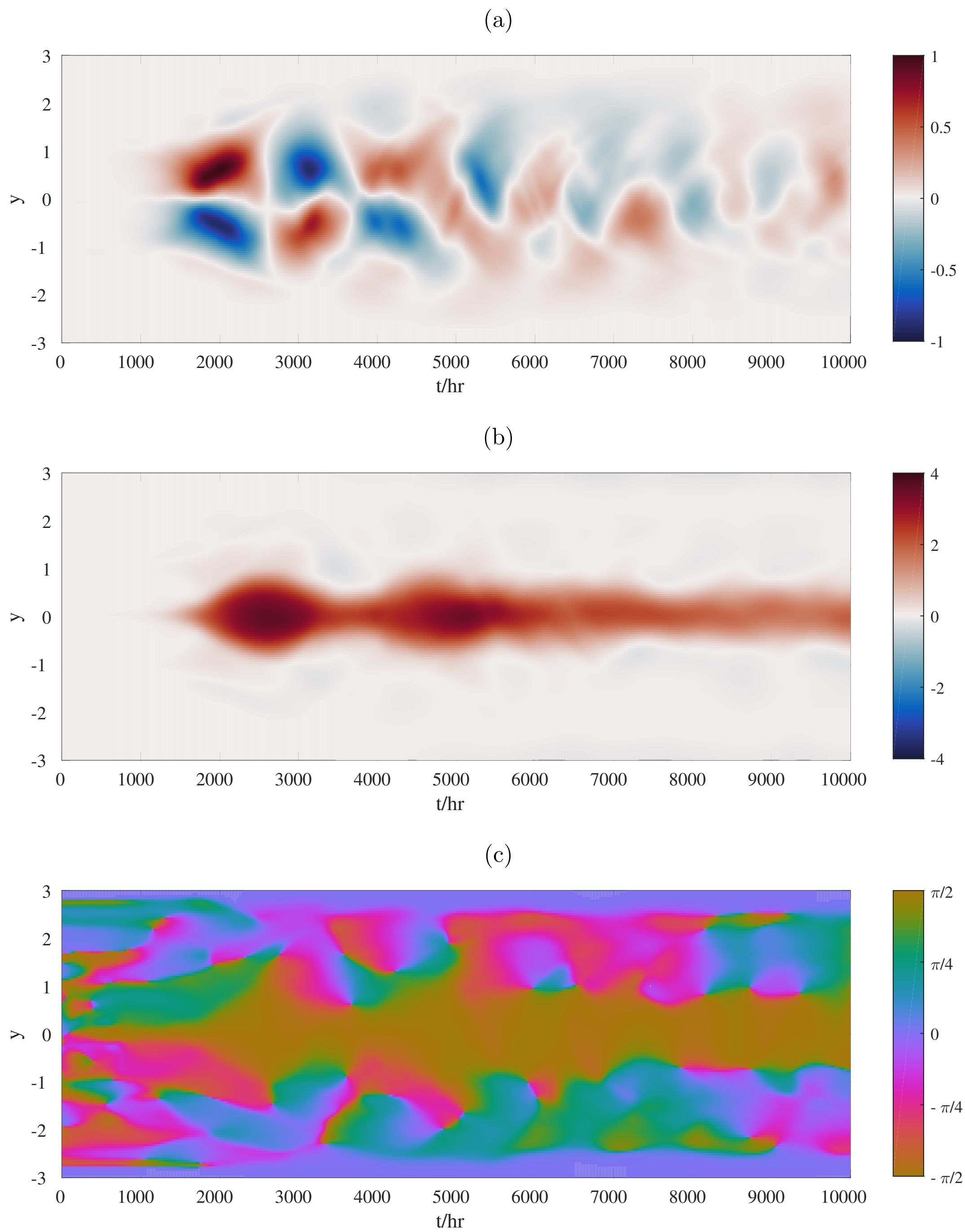

Figure 4.4.4: Hovmöller plots for the eddy ellipse quantities $N/10^{-3}$ m^{2}s^{-2} (a), $M/10^{-3}$ m^{2}s^{-2} (b) and θ/π (c) over the first $10,000$ hrs of the flow evolution.

this point the momentum flux patterns are less obvious as the instabilities begin to break up, though still demonstrate an oscillatory behaviour that coincides with jet sharpening and weakening events.

Turbulent System

We now turn to the more turbulent scenario in which the relaxation term has been switched off. In Fig. 4.4.5 we examine the evolution of the PV-fields for this case.

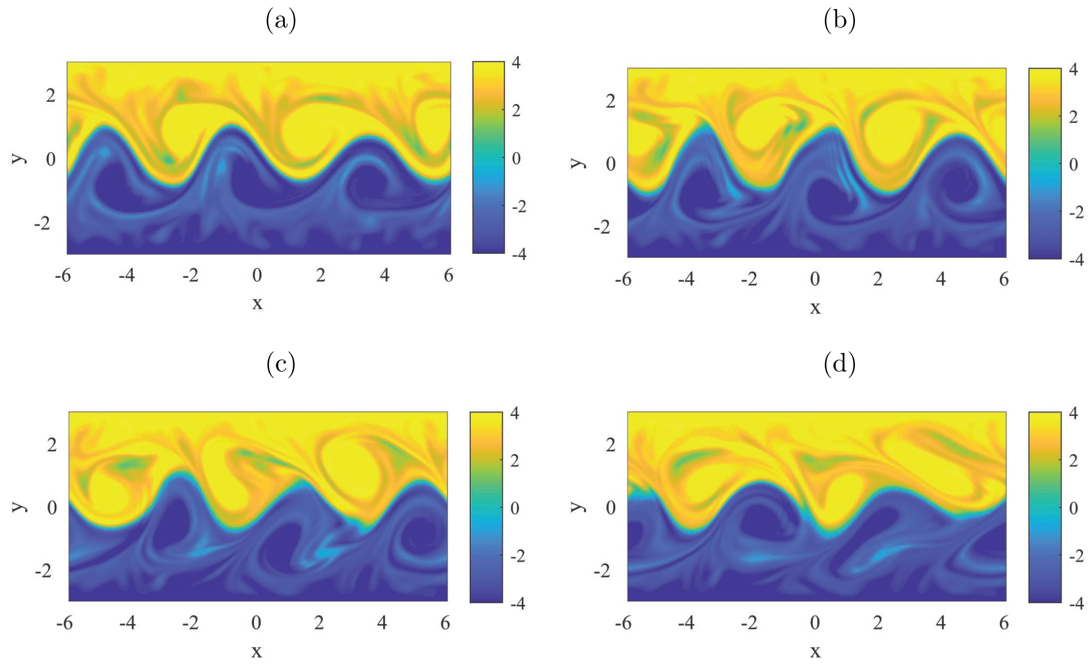

Figure 4.4.5: Snapshot of the potential vorticity $q/10^6$ s^{-1} at different stages of flow evolution for a model run where $r_0 = 0$. The $n = 3$ mode is most unstable and is picked up by the shear, however other modes are not damped by the relaxation term. At $t = 2000$ hrs (a), these instabilities are tilted towards the shear. At $t = 2480$ hrs (b) instabilities begin tilting in the opposite direction until at $t = 3440$ hrs (c) instabilities are tilted against the shear and the flow appears more turbulent. At $t = 3440$ hrs (d) the instabilities begin to break. The coordinates (x, y) are normalised by b.

We see that the flow is marginally more turbulent than when $r_0 \neq 0$ and the growth and decay of the instabilities occur at slightly differing times. Overall though, the evolution of the flow is qualitatively similar to the case where $r_0 \neq 0$ and the initial flow behaviour is dominated by the dynamics of the most unstable mode, $n = 3$. The Reynolds stresses and eddy tilts also show similar behaviours and so are not shown. In Fig. 4.4.6 we plot the inferred eddy ellipse tilt patterns traced in $u' - v'$ prior to, during and after the first jet flattening event at the interface $y = b$. Only at $t = 2,000$ hrs is there an obvious pattern across the jet of ellipse shapes that give rise to the growth of instabilities. At later times, the eddy ellipse shape and orientation is more difficult to determine, especially at $y = +b$. Since in Fig. 4.4.5 we see that the dominant behaviour is from the $n = 3$ mode, we can filter the velocity fields for this mode. The instability is zonal, so we can extract this mode in the velocity fields by taking a zonal Fourier transform and retaining only the $k_x = 3$ mode, where k_x is the zonal wavenumber. The resulting trace in $u' - v'$, of the filtered velocities are shown in 4.4.7. This reveals a distribution of ellipse patterns that almost perfectly match the jet flattening event. Ellipses are tilted at

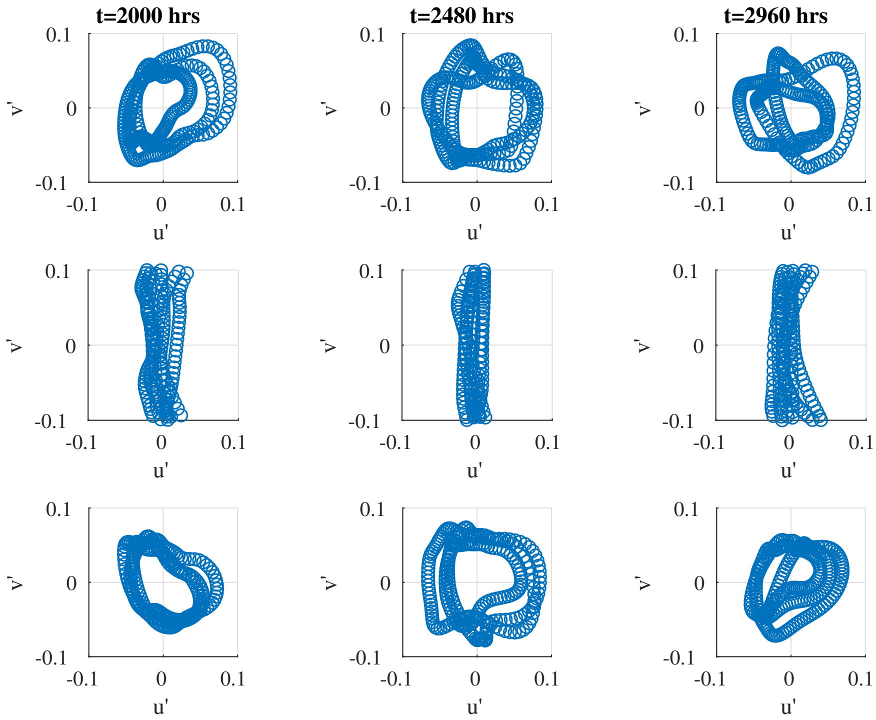

Figure 4.4.6: Scatter plots of (u', v') at different times and meridional locations for a run with $r_0 = 0$. These correspond to Fig. 4.4.5a, Fig. 4.4.5b and Fig. 4.4.5d at meridional locations (top row) $y/b \approx 1$, (central row) $y/b = 0$ and (bottom row) $y/b \approx -1$.

$\theta \approx \pm\pi/4$ against the shear on the flanks of the jets at $t = 2000$ hrs, consistent with momentum being fluxed away from the jet at this time. Then at $t = 2480$ hrs the ellipses are tilted neutrally, suggesting there is no exchange of momentum between the eddies and the mean-flow. Later, at $t = 2960$ hrs the eddy ellipses are tilted towards the shear with $\theta \approx \pm\pi/4$ on the jet flanks. These patterns are not obvious in the unfiltered case with ellipse patterns shown in Fig. 4.4.6. Note that other modes near $n = 3$ were also filtered for, but they did not reveal any significant tilting patterns (not shown). This is consistent with our understanding that the shear instability results in the growth of the $n = 3$ mode only, whilst other modes are not as unstable.

4.4.4 Summary

We have found that the oscillatory nature of the evolution of the zonal velocity profile and qualitative behaviour of the PV-fields can be described as consequences of momentum exchanges between the instabilities and the mean flow. Geometric eddy ellipses reveal the pattern of momentum fluxes which give rise to these exchanges which, in the first instance may be inferred by tracing patterns of $u' - v'$. These patterns agree well with the observed momentum flux

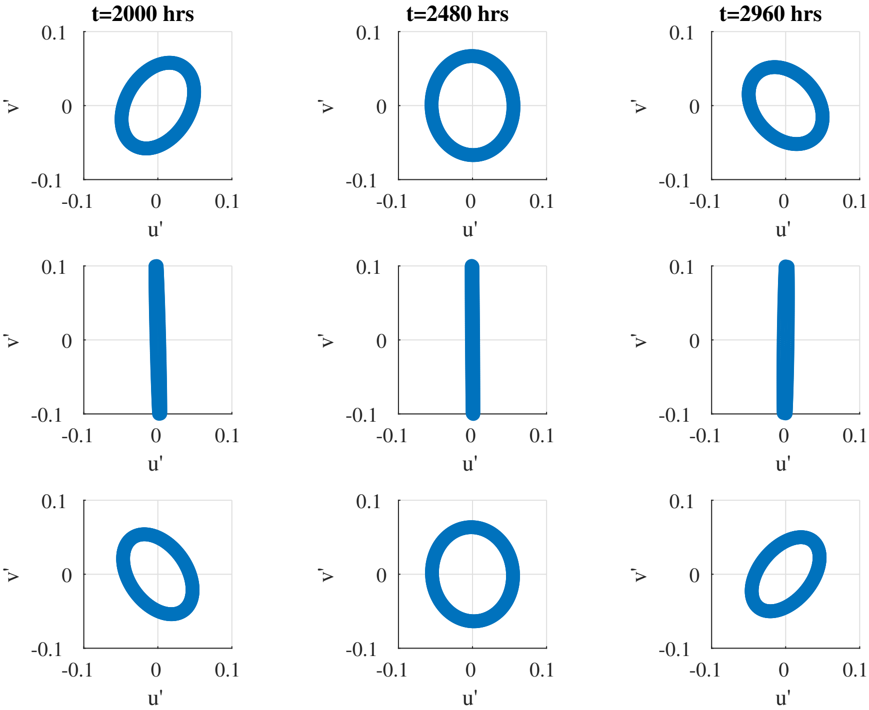

Figure 4.4.7: Scatter plots of (u', v'), using velocity components that are zonally filtered for the $n = 3$ mode. These are plotted at different times and meridional locations for a run with $r_0 = 0$, tracing the variance ellipses for the $n = 3$ mode, corresponding to Fig. 4.4.5a, Fig. 4.4.5b and Fig. 4.4.5d at meridional locations (top row) $y/b \approx 1$, (central row) $y/b = 0$ and (bottom row) $y/b \approx -1$.

patterns but are extremely sensitive, obscured easily by even slightest presence of turbulent behaviours. Filtering u' and v' at $n = 3$ can recover the eddy ellipse tilt patterns in traces of $u' - v'$ in this instance but plotting these traces may have limited scope in a fully turbulent system, where there may be large fluctuations in the velocity field. We may directly calculate eddy ellipse quantities N, M and θ to visualise momentum flux patterns and flux directions. In particular, we have been able to identify the momentum flux and tilt patterns which result in the fluxing of momentum into and away from the mean flow. The dominant dynamical process in the initial stages of evolution, for both $r_0 \neq 0$ and $r_0 = 0$, is the growth and decay of the $n = 3$ mode. For both cases the flow eventually becomes fully turbulent, with the tilt pattern becoming less pronounced and other modes becoming significant. After this point specific momentum flux patterns in the full signal are not so obvious. The geometric eddy ellipse formulation has thus proven to be a useful tool for examining the eddy-mean flow interactions in a barotropically unstable jet. In the turbulent case, filtering can help to identify dominant or underlying dynamics when the ellipse parameters are obscured by the presence of multiple modes.

4.5 Conclusion

In this chapter we have introduced the eddy velocity correlation tensor, whose components are the Reynolds' stresses and shown that this is related to the mean flow through a divergence in the momentum flux. We have introduced a geometric eddy ellipse formulation, which describes the kinetic energy K, the momentum flux N and normal stress difference M, in terms of an ellipse with a magnitude, tilt and eccentricity. Patterns in the distribution of geometric eddy ellipses allow us to visualise the eddy-mean flow interactions. These ideas have been examined in the case of a barotropically unstable jet that has been perturbed and the evolution of unstable modes have been examined, following analysis by Tamarin et al. (2016). By identifying patterns in the tilt angles of the associated ellipses at the shear interfaces, we have been able to build a detailed picture of the eddy-mean flow interactions between the jet and instabilities. We will now seek a formulation in which geometric eddy ellipses may be used to examine eddy-mean flow interactions in geostrophic turbulent jets.

5

Geostrophic Turbulence

5.1 Introduction

High Reynolds number systems which are approximately two-dimensional and evolve within a rapidly rotating frame of reference, may exhibit geostrophic turbulence. As we discussed in §1, the rotating frame of reference itself may be the very cause of the two-dimensionalisation of the fluid via the Taylor-Proudman theorem. For a system to exhibit spontaneous jet formation in geostrophic turbulence it must experience differential rotation in which the planetary vorticity varies with spatial location. To model the effects of differential rotation, the β-plane approximation can be used in the quasi-geostrophic equation given by Eq. (2.2.1), in which planetary vorticity f is taken to vary linearly with latitude. Rhines (1975) first presented a theory working within this setting, in terms of the inverse energy cascade and explored how this was anisotropised by the excitation of Rossby-waves at large scales. The emergent jet structures were then argued to scale according to the Rhines scale given by Eq. (1.2.31). Dritschel and McIntyre (2008) discussed the formation of jets as a consequence of PV-mixing by breaking Rossby-waves and the PV-invertibility principle, resulting in the formation of sharp eastward jets and broad westward jets. Other works focussed on the energy spectrum, in which contour plots of energy in wavespace $k_x - k_y$ reveal a dumbbell structure (Vallis and Maltrud, 1993). A pile up of energy in the vicinity of the k_y-axis has also been observed (Chekhlov et al., 1996). These viewpoints are all interconnected and complimentary to one another. The focus of the first half of this chapter is to unify these different perspectives. We find that the location and propagation of a time-dependent energy front $k_{\min}$, in the angular averaged energy spectra is central to this aim. In the second half of the chapter, we show how we can apply the geometric eddy ellipse formulation, introduced in §4, to study equilibrated jets that have formed under the action of β-plane turbulence. We find that the important scales of motion identified in this chapter do not explain the scales responsible for supporting and maintaining the jet structures.

Table 5.1: Summary of run parameters used in this chapter.

Run	$A0$	$B0$	$C0$	$D0$	$A1$	$B1$	$C1$	$D1$
β	0	β_0	$4\beta_0$	$16\beta_0$	0	β_0	$4\beta_0$	$16\beta_0$
r	0	0	0	0	r_0	r_0	r_0	r_0

5.2 Model Parameters

The channel model used for all simulations in this chapter had dimensions of $L_x =$ 6000 km and $L_y = 3000$ km with 513×257 grid points such that $\Delta x = \Delta y =$ 11.7 km and $\Delta t = 112.5$ s. All simulations used a stochastic isotropic forcing with a constant enstrophy injection rate $\xi = 8 \times 10^{-18}$ s^{-3} at a length scale given by $k_f = 64$, such that the energy injection rate is $\epsilon = 1.78 \times 10^{-8}$ m^{2}s^{-3}. A biharmonic diffusion term was used to suppress the enstrophy cascade with a coefficient $\mathcal{D}_\mathrm{B} =$ 5×10^{10} m^{4}s^{-1} and we set $\mathcal{D}_\mathrm{H} = 0$. Runs were performed with four different rotation rates: $\beta = 0$, $\beta = \beta_0$, $\beta = 4\beta_0$ and $\beta = 16\beta_0$, where $\beta_0 = 2.29 \times 10^{-11}$ m^{-1}s^{-1} is the terrestrial equatorial value. Four runs were damped with Rayleigh friction $r = r_0 \equiv 1 \times 10^8$ s^{-1}. Runs and parameters used in this chapter are summarised in Table 5.1. Although we are using rotation rates where β is larger than its maximum terrestrial value, this is not to say these will be invalid for terrestrial problems. Parameters may be chosen in such a way that they possess dynamic similarity to terrestrial problems. To show this, we non-dimensionalise the barotropic vorticity equation given by Eq. (2.2.1) according to a characteristic length scale L and velocity scale U:

$$(x, y) = L\left(\widetilde{x}, \widetilde{y}\right), \quad (u, v) = U\left(\widetilde{u}, \widetilde{v}\right), \quad \zeta = \frac{U}{L}\widetilde{\zeta}, \quad t = \frac{L}{U}\widetilde{t}, \tag{5.2.1}$$

where non-dimensional quantities are denoted by a tilde, and obtain the dimensionless equation

$$\frac{\partial \widetilde{\zeta}}{\partial \widetilde{t}} = -\widetilde{u}\frac{\partial \widetilde{\zeta}}{\partial \widetilde{x}} - \widetilde{v}\frac{\partial \widetilde{\zeta}}{\partial \widetilde{y}} - \frac{1}{R_\beta}\widetilde{v} - r'\widetilde{\zeta} - \frac{1}{Re_\mathrm{B}}\widetilde{\nabla}^4\widetilde{\zeta}. \tag{5.2.2}$$

Here we have introduced the β-Rossby number

$$R_\beta = \frac{U}{\beta L^2}, \tag{5.2.3}$$

the damping parameter

$$r' = \frac{rL}{U}, \tag{5.2.4}$$

Table 5.2: Summary of dimensionless parameters R_β and Ek for runs presented in this chapter.

β	R_β	Ek
β_0	0.0218	4.58×10^{-6}
$4\beta_0$	0.00546	1.83×10^{-6}
$16\beta_0$	0.00136	7.33×10^{-6}

and the biharmonic Reynolds number

$$Re_{\mathrm{B}} = \frac{L^3 U}{D_{\mathrm{B}}}. \tag{5.2.5}$$

We can divide Eq. (5.2.3) by Eq. (5.2.5) to obtain the Ekman number:

$$Ek = \frac{R_\beta}{Re_{\mathrm{B}}}. \tag{5.2.6}$$

Our system has typical length scales $L \approx 1000$ km and velocities $U \approx 0.5$ ms^{-1}. This gives $Re_{\mathrm{B}} = 1 \times 10^7$ and $r' = 2 \times 10^{14}$ for systems in which we include Rayleigh friction. The corresponding Ekman numbers for each β are summarised in Table 5.2. Jet observations inferred from satellite altimetry data at $1000-1500$ m in the tropical Pacific ocean, for example, show jets to have typical velocities $U \approx 0.05$ ms^{-1} and meridional extent $L \approx 200$ km (Cravatte et al., 2012). This gives $R_\beta = 0.0063$ which is similar to the order of magnitude of values of R_β used in this thesis, summarised in Table 5.2.

5.3 Jet Formation

For two-dimensional turbulent systems forced at small scales, we argued that there is a preferential transfer of energy towards the largest scales that is associated with the inverse energy cascade. In this section we will consider its signature in physical space. The amount of energy contained at a certain length scale follows the $k^{-5/3}$ Kolmogorov power law in Eq. (1.2.23). This tells us that the largest length scales occupied by energy, around some wavenumber k_{min}, will also contain most of the energy in the system, so the total energy E_{m} is

$$E_{\mathrm{m}} = \int_0^\infty E(k)dk \approx \int_{k_{\mathrm{min}}-\delta}^{k_{\mathrm{min}}+\delta} E\left(k\right) dk, \tag{5.3.1}$$

where δ is some small interval. If the system is being spun up from rest, assuming scaling invariance, we expect the spectrum to grow self-similarly and the position of k_{min} will change in time. In this instance, we can think of k_{min} as an energy front which in general will be time-dependent. We also expect that the eddy turnover frequency is approximately proportional to scale

$$\omega_T \propto k. \tag{5.3.2}$$

This implies that the largest and most energetic scale $k_{\min}$ is also the longest-lived. In other words, coherent large-scale structures should dominate the flow[1]. For systems in which $\beta = 0$, flows follow the dynamics of the two-dimensional vorticity equation given by Eq. (1.2.17) and do not exhibit any wave-like characteristics. In these systems there is nothing to anisotropise the cascade of energy so we expect coherent structures to be isotropic. When $\beta \neq 0$, the dynamics will follow Eq. (1.2.13) which differs from Eq. (1.2.17) by the β-plane. This allows for Rossby waves to propagate which, when excited, anisotropise the energy transfer, funnelling energy towards zonal wavenumbers (Rhines, 1975). Therefore, we expect the emerging coherent structures to be zonally elongated.

In Fig. 5.3.1 we compare snapshots of the evolution of the ψ-fields for runs A_0 and B_0.

The temporal evolution of A_0 exhibits signatures of the inverse cascade. At early stages the flow field is dominated by small-scale structures. By $20,000$ hrs these have merged together to form larger structures which can be seen in Fig. 5.3.1 with average scales of around $k = 2 - 4$. These mergers occur successively between vortices of larger size as more energy is pumped into the system. Since these runs are being continuously forced at small scale without energy removal at the largest scales, continues to move upscale until it reaches the domain size ($k_0 = 1$) where it begins to accumulate. This pile up of energy leads to the emergence of a so-called condensate which in our geometry are associated with two cells of opposite signed vorticity. These are the two structures observed in the ψ-field at $t = 40,000$ hrs.

In the initial stages of evolution, the flow fields obtained from run B_0 look similar to those of run A_0. Notably though we see that the structures in B_0 are smaller than those of A_0, indicative of there being some process inhibiting the progress of the cascade compared to run A_0. Run B_0 too exhibits the successive merger of smaller scale structures into larger ones, however in this case the structures which begin to emerge are zonally elongated. As the flow evolves and the system becomes more energetic, these jets become broader. This indicates that although energy is being transferred in an inverse cascade, as in the case A_0, this transfer is occurring anisotropically and favouring the formation of zonally elongated structures. The

[1]McWilliams (1984) refers to "coherent structures" as those which persist longer than time-scales associated with the inverse cascade. However, we use the term "coherent structures" simply for long-lived identifiable structures which in our case, we associate with the inverse casacade.

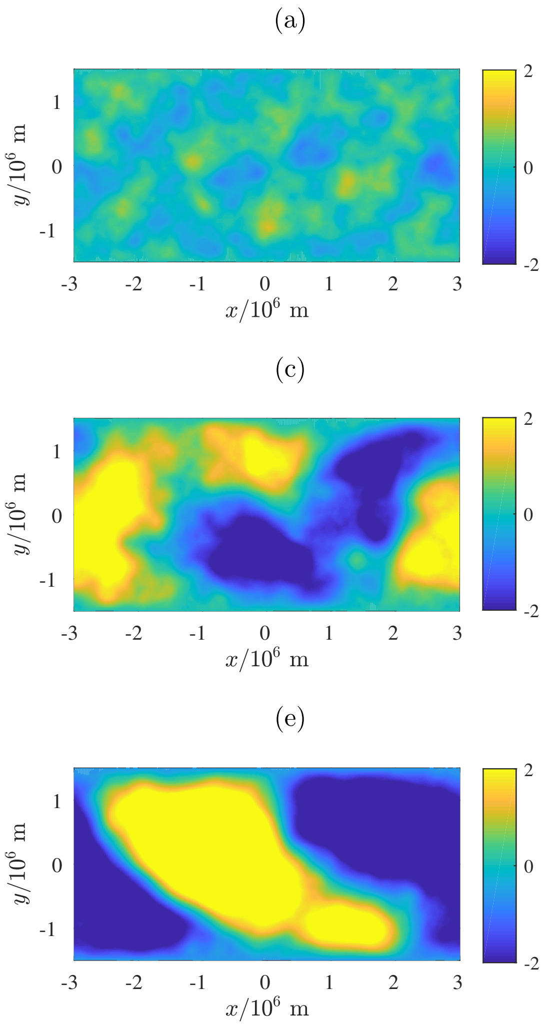

Figure 5.3.1: Comparison of instantaneous ψ-fields at $t = 10,000$ hrs (a) and (b), $t = 20,000$ hrs (c) and (d), and $t = 40,000$ hrs (e) and (f) for runs $A0$ and $B0$ respectively.

largest scales associated with run B_0 would manifest as two strips of opposite vorticity, in practice though this state is difficult to attain as it requires a very long period of integration due to the anistropisation process slowing down the progression of $k_{\min}$.

Since we are primarily interested in the emergence of zonal coherent structures, it is useful to see how the zonal average zonal velocity $\overline{u}$ evolves in time. We do this in Fig. 5.3.2c by examining the Hovmöller plots of $\overline{u}$ for runs A_0, B_0, C_0 and D_0, which each have different β-planes summarised in 5.1. The cascade of energy to larger scales is evident in all runs, with small scale zonal structures merging into larger ones and the larger structures persisting longer than smaller ones, as we expect.

The flow in A_0 rapidly approaches the domain-scale and even though $\beta = 0$ in this case the flow does demonstrate some zonal structure. However, what

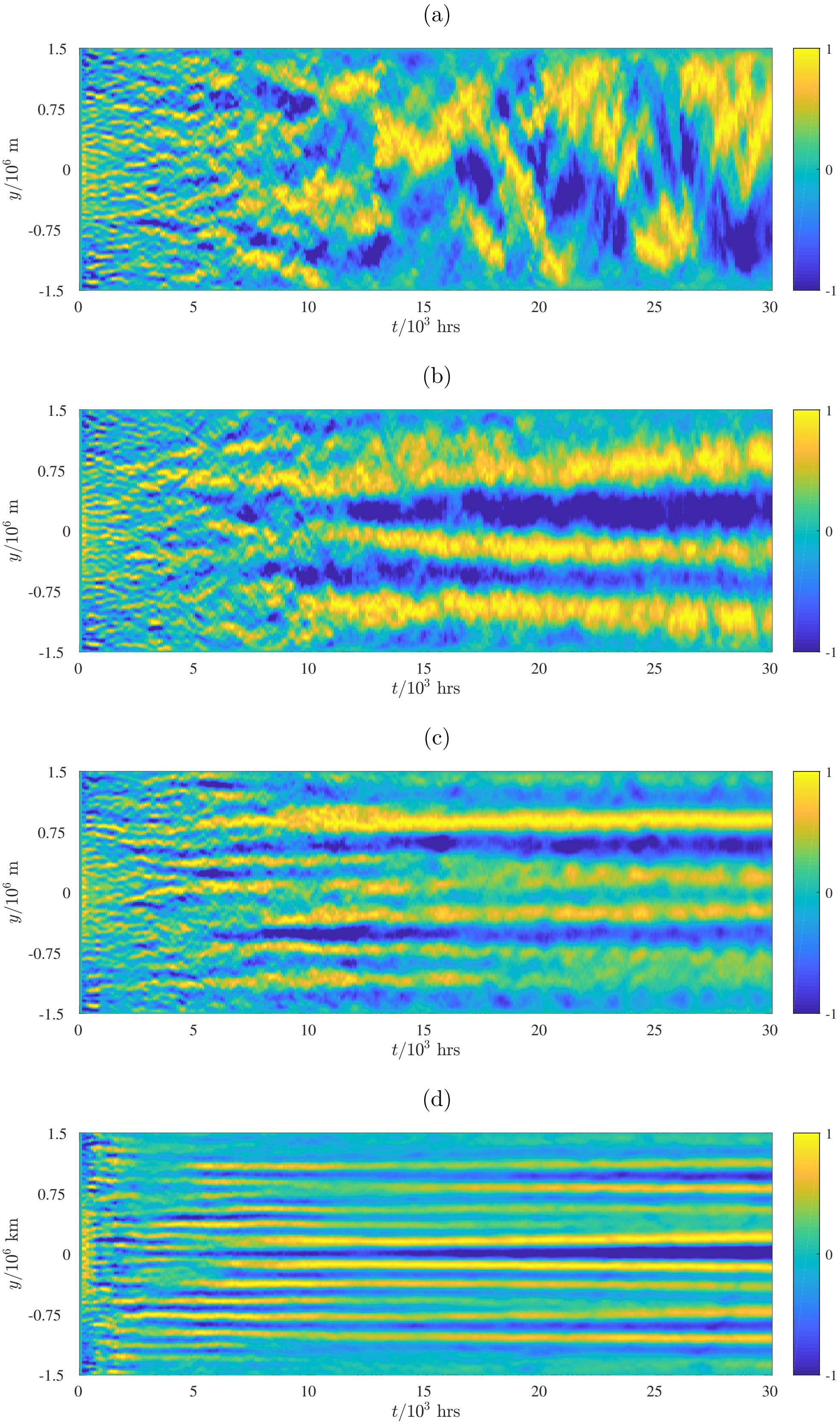

Figure 5.3.2: The Hovmoller plots of u for runs A_0 (a), B_0 (c), C_0 (c) and D_0 (d) normalised by their instantaneous maximum velocity.

we observe in these plots does not correspond to zonal jets but isotropic patches of vorticity. We have seen in Fig. 5.3.1 that the latter stages of evolution are dominated by the condensates consisting of two cells of opposite signed vorticity. These are constrained by the domain walls and the apparent sinusoidal behaviour we see in the late-stage evolution of run A_0 is caused by these vortices meandering out of phase with one another in the meridional direction.

The evolution of run B_0 is very similar to that of A_0 for around the first $7,000$ hrs of the integration period. After this point we begin to see some jet structures which rapidly develop into longer-lived jet structures. The system appears to approach a pattern of two westward jets interleaved between three eastward jets which broaden and sharpen respectively. The cascade appears to slow down significantly after this point, as the number of jets do not change.

The evolution of run C_0 exhibits jet formation very early on under the action of a stronger β-plane, with some evidence of isotropic dynamics in the initial stages. Jet merger events occur frequently in these early stages of the flow evolution but between about $t \approx 10,000 - 15,000$ hrs the frequency of jet merger events significantly reduces. For the remaining stages of the integration period, the structures evolve very slowly though we still witness some slow eastward jet sharpening, westward jet broadening and jet merger events over this time.

The flow in run D_0 organises almost immediately into a persistent pattern of fine jet structures, under the action of the strong β-plane, with very little sign of any isotropic dynamics in the initial stages. Throughout the integration period these structures evolve very slowly in comparison to runs with smaller β. Some persist and strengthen throughout the integration period whilst a few others show signs of merging.

Since we have chosen a form of the forcing to produce a constant ϵ, the energy should grow at a constant rate according to

$$E_{\mathrm{m}}(t) \approx \epsilon t. \tag{5.3.3}$$

In practice, we also remove energy by dissipating at very small length scales. However, because most of the energy is contained at larger scales, this relationship holds approximately. In Fig. 5.3.3, we plot the energy as a function of time for the four continuously forced simulations. In all cases, energy growth is close to linear in the initial stages of evolution before energy removal by the biharmonic friction, which we denote E_{B}, becomes significant and leads to saturation in the growth of energy for some period of time. Then after energy in the system overcomes the biharmonic dissipation, the energy growth possesses a steeper than linear behaviour, though runs A_0 and B_0 begin to shallow toward

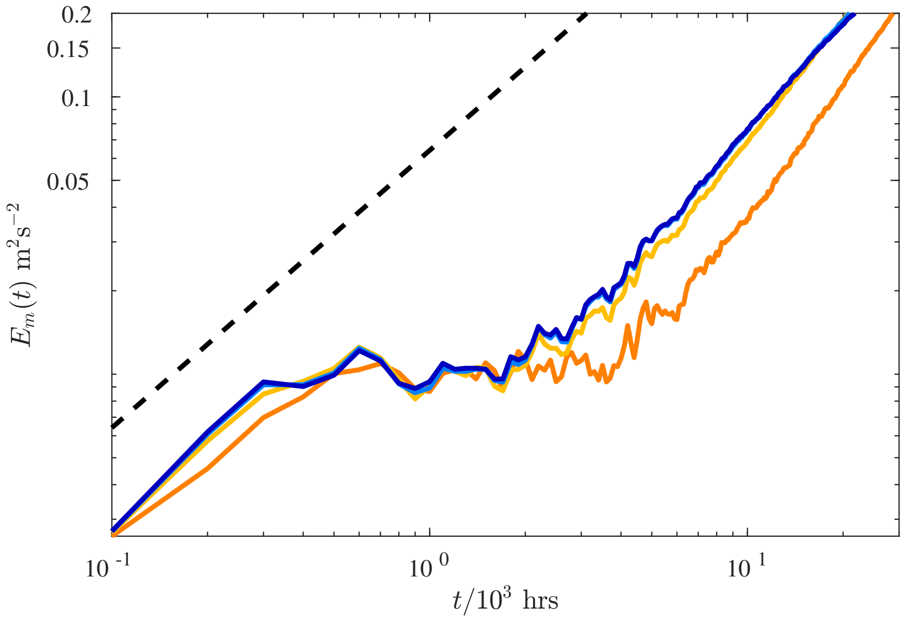

Figure 5.3.3: The evolution of $E_m(t)$ over a $T = 60,000$ hrs spin up period for runs A_0 (dark blue), B_0 (light blue) C_0 (yellow) and D_0 (orange). The predicted energy growth calculated from Eq. (5.3.3) is also shown (black dotted). Note the scales are logarithmic.

linear growth in their later stages. The energy growth for runs A_0 and B_0 are generally very similar throughout their evolution. In contrast, the effect of the biharmonic is more prominent for run C_0, which never approaches a linear growth and D_0 has significantly less energy in its evolution.

In theory, there is no reason for the β-plane to affect the evolution of E_m but in practice simulations with stronger β-planes have sharper gradients. Because the magnitude of E_B is dependent on vorticity gradients, this in turn produces larger E_B. We will also see later on that the β-plane has the effect of slowing down the inverse cascade. This in turn keeps the flows at smaller scales for longer periods of time since these scales are more prone to scale-selective biharmonic dissipation. In all the cases considered, the effect of the biharmonic is significant even at intermediate scales which can affect some of our analysis that assumes ϵ is constant over the inertial range of the inverse energy cascade. Unfortunately, we cannot simply subtract the energy removed by the biharmonic to produce an effective energy injection rate ϵ_eff *a priori* as the dissipation is a function of the emergent flow. Moreover, difficulties arise in attempting to weaken the amplitude of the biharmonic diffusion or increase the amplitude of forcing as these both of these lead to the enstrophy cascade not being fully suppressed. The only solution, without significantly changing the model setup, would be to place the forcing scale at a lower wavenumber. This is because larger scales are less prone to dissipation as the biharmonic is scale-selective and the enstrophy cascade would remain suppressed in this scenario. As we continue to develop the theory of geostrophic turbulence, we will learn that there are several characteristic scales that lie within the inertial range, which should ideally be sufficiently well-separated. A lower wavenumber forcing would restrict these intervals. Since we are primarily interested in these characteristic scales, we will progress without altering model configuration.

The assumption of linear energy growth in time does not lead to the energy front itself $k_{\text{min}}(t)$ propagating to largest scales linearly. As we can see from the speed at which coherent structures emerge in Fig. 5.3.2, the propagation of k_{min} appears to be fastest when $\beta = 0$. To understand this we derive a relationship for the propagation in time of k_{min} that is associated with the Kolmogorov spectrum. Integrating Eq. (1.2.23) to obtain the energy gives

$$E_{\text{m}} = \int_0^\infty E(k,t)\, dk \approx \int_{k_{\text{min}}}^{k_f} C_K \epsilon^{\frac{2}{3}} k^{-\frac{5}{3}} dk = C_K \epsilon^{\frac{2}{3}} k_{\text{min}}^{-\frac{2}{3}}. \tag{5.3.4}$$

The characteristic velocity U_{rms} is related to E_{m} as

$$U_{\text{rms}} = \sqrt{2E_{\text{m}}}, \tag{5.3.5}$$

so the position of the energy front associated with the Kolmogorov spectrum Eq. (1.2.23) is given by

$$k_{\text{min}} \propto k_{\text{KBK}} \equiv \frac{\epsilon}{U_{\text{rms}}^3}, \tag{5.3.6}$$

where we have defined the Kolmogorov (Batchleor-Kraichnan) wavenumber, k_{KBK}. Since our system has an approximate linear energy growth in time given by Eq. (5.3.3) we can obtain explicitly the time dependence for Eq. (5.3.5)

$$U_{\text{rms}} \approx \sqrt{2\epsilon t}, \tag{5.3.7}$$

and in turn, we can find the time dependence of k_{KBK}:

$$k_{\text{KBK}}(t) \approx (8\epsilon)^{-\frac{1}{2}} t^{-\frac{3}{2}}. \tag{5.3.8}$$

We see in Fig. 5.3.2 that when $\beta = 0$, the flow appears to progress to the largest scales relatively quickly compared to when $\beta \neq 0$ but our expression for the propagation of the Kolmogorov energy front given by Eq. (5.3.8) does not have a β-dependence. This is because there is a separate inertial range associated with the β-plane with a slower time-dependence, which we introduced in §1 as the Rhines spectrum Eq. (1.2.35) with a k^{-5} power-law. We will show explicitly in the next section that the Rhines scale is the energy front associated with this power-law, but this is something that we can intuit. We have previously discussed that according to Rhines (1975), the width of zonal structures in β-plane turbulence is set by the Rhines scale given by Eq. (1.2.31) i.e.

$$k_{\text{jet}} = k_{\text{R}}. \tag{5.3.9}$$

Rhines (1975) gave no rigorous justification for this and it was initially disputed by Vallis and Maltrud (1993). Nevertheless, if one assumes this result to hold then as more and more energy is injected into the system U_{rms} will grow according to Eq. (5.3.5) and so k_R will decrease. In systems with fixed $\beta \neq 0$, we have witnessed the successive merger of jets and that the jet number decreases as energy cascades towards the domain scale. This may be interpreted as the Rhines scale evolving in real-time. Now, we have also stated that we expect most of the system's energy to reside at the largest energy containing scale k_{min} and that large scale coherent structures are the manifestation in physical space of this scale. This eludes to the Rhines scale, analagous to k_{KBK}, as being the candidate for the energy front associated with the spectrum given by Eq. (1.2.35) i.e.

$$k_{\text{jet}} = k_{\text{min}} \propto k_{\text{R}}. \tag{5.3.10}$$

Using the assumption of linear energy growth in time given by Eq. (5.3.7) we can show that the Rhines scale given by Eq. (1.2.31) evolves according to:

$$k_{\text{R}} \approx \frac{\sqrt{\beta}}{(8\epsilon)^{\frac{1}{4}}} t^{-\frac{1}{4}}, \tag{5.3.11}$$

which is a relationship first noted in Sukoriansky et al. (2007). So we see that the inclusion of the β-plane alters the time-dependence of the front evolution, slowing it down compared to systems in which $\beta = 0$. We also see from Eq. (5.3.11) that the stronger the β-plane, the slower the evolution of the energy front.

We examine this relationship by calculating U_{rms} for each of our simulations to estimate the evolution of k_{min} over time from Eq. (5.3.6) and Eq. (1.2.31) for cases where $\beta = 0$ and $\beta \neq 0$ respectively. Additionally, in knowing ϵ *a priori* we can predict the temporal evolution of k_{min} using Eq. (5.3.8) for $\beta = 0$ and Eq. (5.3.11) for $\beta \neq 0$. We have plotted the time propagation from the run data in Fig. 5.3.4 alongside their predicted behaviour. The biharmonic acts to stagnate the progression of the estimated energy fronts at early times. Once energy builds up sufficiently to overcome the biharmonic, the estimated front progresses follows shallower time-dependence to the predicted. Run A_0 approaches the largest scales most rapidly, which agrees with the behaviour we have seen in Fig. 5.3.2a where

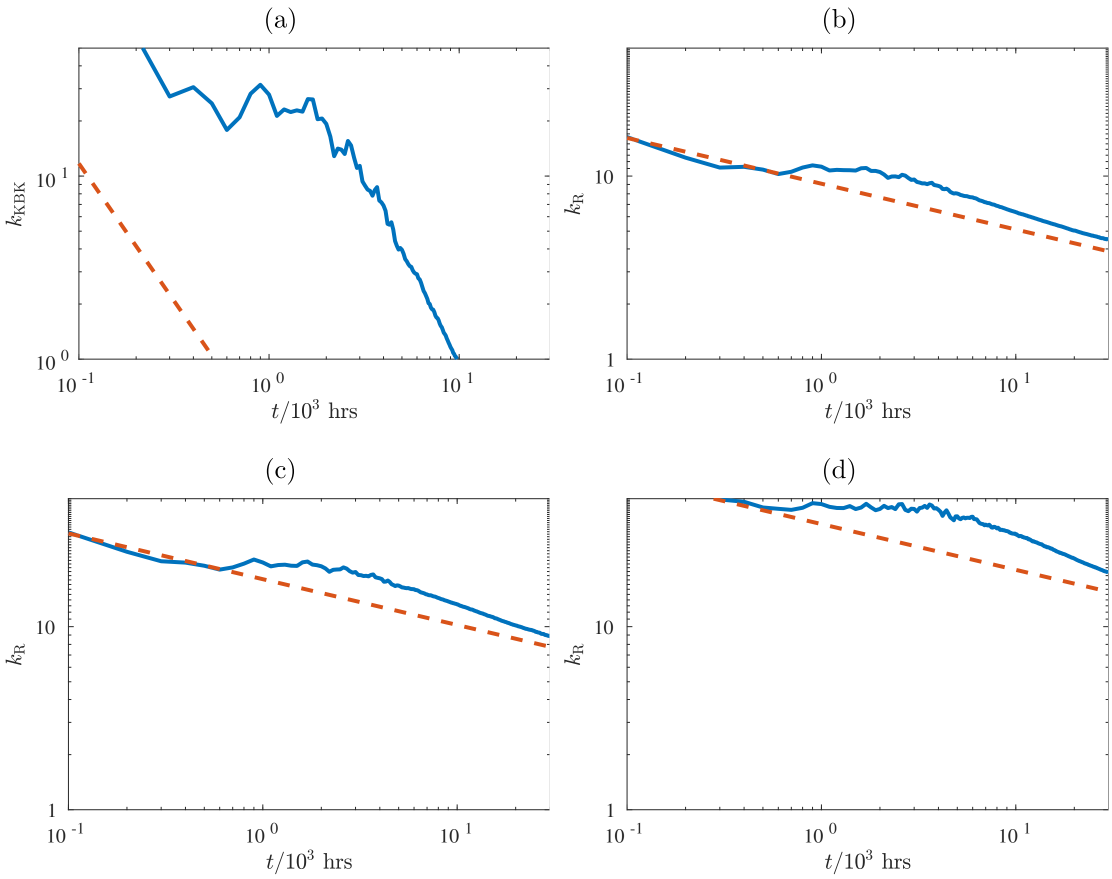

Figure 5.3.4: The progression of the estimated Kolmogorov scale (solid blue) and its prediction $k^p_{\mathrm{KBK}}(t)$ (orange dotted) for run A_0 (a) and the progression of the estimated Rhines scale (solid blue) and predicted Rhines scale $k^p_{\mathrm{R}}(t)$ (dashed orange) for runs B_0 (b), C_0 (c) and D_0 (d).

domain-scale structures emerge early on. Although the estimate suggests that at $t = 30,000$ hrs, the front should sit at $k = 0$, this not possible in our bounded domain geometry in which the $k = 0$ mode cannot be populated. As we have seen from Eq. (5.3.11), the time-evolution of k_{min} will possess a different form when $\beta \neq 0$. Firstly, observe that the predicted time-dependences take longer to reach the largest scales for systems with stronger β. For all runs with $\beta \neq 0$, the time evolution of the energy fronts tend towards their predicted behaviours after overcoming the biharmonic. In all cases where $\beta \neq 0$, the propagation to the larger scales decelerates significantly at intermediate scales, as time progresses. This deceleration is becomes more pronounced as β increases. Additionally, because it takes longer for k_{min} to pass through the higher-wavenumbers as we increase β, this in turn has the effect of keeping the front stagnated by the biharmonic for a longer period of time. This explains why we see jets evolving very slowly when $\beta = 16\beta_0$ compared to when β is smaller.

We can see from Fig. 5.3.2 that, in general, after jets have formed, they successively merge and reduce in number as time-progresses, though this is less obvious when $\beta = \beta_0$ since the flow approaches the largest scales so rapidly in this case. Jet formation and merger, we have argued is the manifestation in physical space of the propagation of k_{R} in spectral space so we expect the relationship given by Eq. (5.3.9) to hold. The effect of the biharmonic prevents the jet profiles from following the predicted behaviour exactly. However, the estimated Rhines scales in Fig. 5.3.4 accurately determine the total number of eastward and westward jets that form in Fig. 5.3.2.

5.3.1 Equilibrium Jets

We will now consider the effect of including a linear drag term that is effective at dissipating energy at large scales thus allowing our flows to equilibrate. In these systems, the energy will evolve according to

$$\frac{dE_{\mathrm{m}}}{dt} = \epsilon - 2rE_{\mathrm{m}} - E_{\mathrm{B}}. \tag{5.3.12}$$

If E_{B} is negligible then, for a flow evolving from rest, the solution to Eq. (5.3.12) will be given by

$$E_{\mathrm{m}}(t) \approx \frac{\epsilon}{2r}\left(1 - e^{-2rt}\right). \tag{5.3.13}$$

As $t \to \infty$, we obtain the steady state energy

$$E_{\mathrm{eq}} \approx \frac{\epsilon}{2r}. \tag{5.3.14}$$

When we analysed our continuously forced systems, we interpreted the Kolmogorov wavenumber and the Rhines wavenumber as the position of an energy front that propagates towards the largest available scale as time progresses. We found that when $r = 0$ and E_{B} is assumed to be negligible, the solution to Eq. (5.3.12) is given by Eq. (5.3.3), where time and energy are proportional. In the presence of Rayleigh friction, this is no longer true and the propagation of the energy front will be halted[2]. Though the energy at which the system equilibriates should be the same for runs with differing β, the frictional or equilibrium wavenumber k_{eq} at which this occurs will be different. We may obtain this following a similar procedure to the continuously forced case, using Eq. (5.3.5) in Eq. (5.3.6) when $\beta = 0$ and in Eq. (1.2.31) when $\beta \neq 0$, and replacing E_{m} with E_{eq} from Eq. (5.3.14). The equilibrium wavenumbers are then found to be

[2]This is not to be confused with the concept of a cascade arrest, where the β-plane is thought to halt the cascade of energy at the Rhines scale.

$$k_{\mathrm{KBK}} = k_{\mathrm{eq}} = \left(\frac{8r^3}{\epsilon}\right)^{\frac{1}{2}}, \text{ when } \beta = 0, \tag{5.3.15a}$$

$$k_{\mathrm{R}} = k_{\mathrm{eq}} = \left(\frac{r\beta^2}{4\epsilon}\right)^{\frac{1}{4}}, \text{ when } \beta \neq 0. \tag{5.3.15b}$$

So k_{eq} is the final destination of the energy front in the presence of the Rayleigh friction. We see from Eq. (5.3.15b) that for a fixed r and ϵ, $k_{\mathrm{eq}} \propto \sqrt{\beta}$ for flows on the β-plane, which means that for different β the jets should scale as

$$k_{\mathrm{jet}} = k_{\mathrm{R}}\,(t \to \infty) = k_{\mathrm{eq}} \propto \sqrt{\beta}. \tag{5.3.16}$$

In Fig. 5.3.5, we examine the time-averaged zonal velocity profiles $[\overline{u}]$, where the square braces indicate a time-average, for β-plane runs $B1$, $C1$ and $D1$, over a 20,000 hrs equilibration period. All possess broad westward jets interspersed with sharp eastward jets with the number of jets increasing as β increases. Between runs B_1 and C_1, the number of westward jets and eastward jets are $k_{\mathrm{jet}} = 5$ and $k_{\mathrm{jet}} = 9$ respectively. These do not agree with their predicted values found by calculating the equilibrium wavenumber using Eq. (5.3.15b), which gives $k^p_{\mathrm{eq}} \approx 3$ and $k^p_{\mathrm{eq}} \approx 6$ respectively, where the superscript p indicates the predicted value. However the jet number does roughly double as β quadruples which agrees with the relationship given by Eq. (5.3.16).

The reason the number of jets are not exactly what is predicted can be traced to the crude estimate of E_{B}. The equilibration energy is predicted to be $E^p_{\mathrm{eq}} = 0.89\ \mathrm{m^2s^{-2}}$ for all runs but, as we know, energy is lost to the biharmonic and its growth differs unpredictably for runs with different β. We expect in general that the number of jets will be larger than predicted which is what we observe for runs B_1 and C_1. We have calculated the true equilibration energy E_{eq} and the true frictional wavenumbers k_{eq} associated with all equilibrated runs and these are tabulated in 5.3. We see that the equilibriation energy is similar for runs A_1, B_1 and C_1 which is why the proportionality relationship of Eq. (5.3.16) holds between B_1 and C_1, even if the exact number of jets are not the same as predicted. The proportionality relationship does not hold for run D_1 where there are fewer equilibrium jets ($k_{\mathrm{jet}} = 12$) than the ≈ 18 jets expected from Eq. (5.3.16). The equilibration energy is a lot higher for this run but what is peculiar is that the number of jets in run D_1 does not agree with its actual frictional wavenumber $k_{\mathrm{eq}} \approx 15$. The fact that it actually agrees best with the predicted $k^p_{\mathrm{eq}} \approx 11$ is a coincidence. This suggests that run D_1 does not follow the scaling laws Eq. (5.4.4). We will later in this chapter that this is due to run D_1 demonstrating inadequate

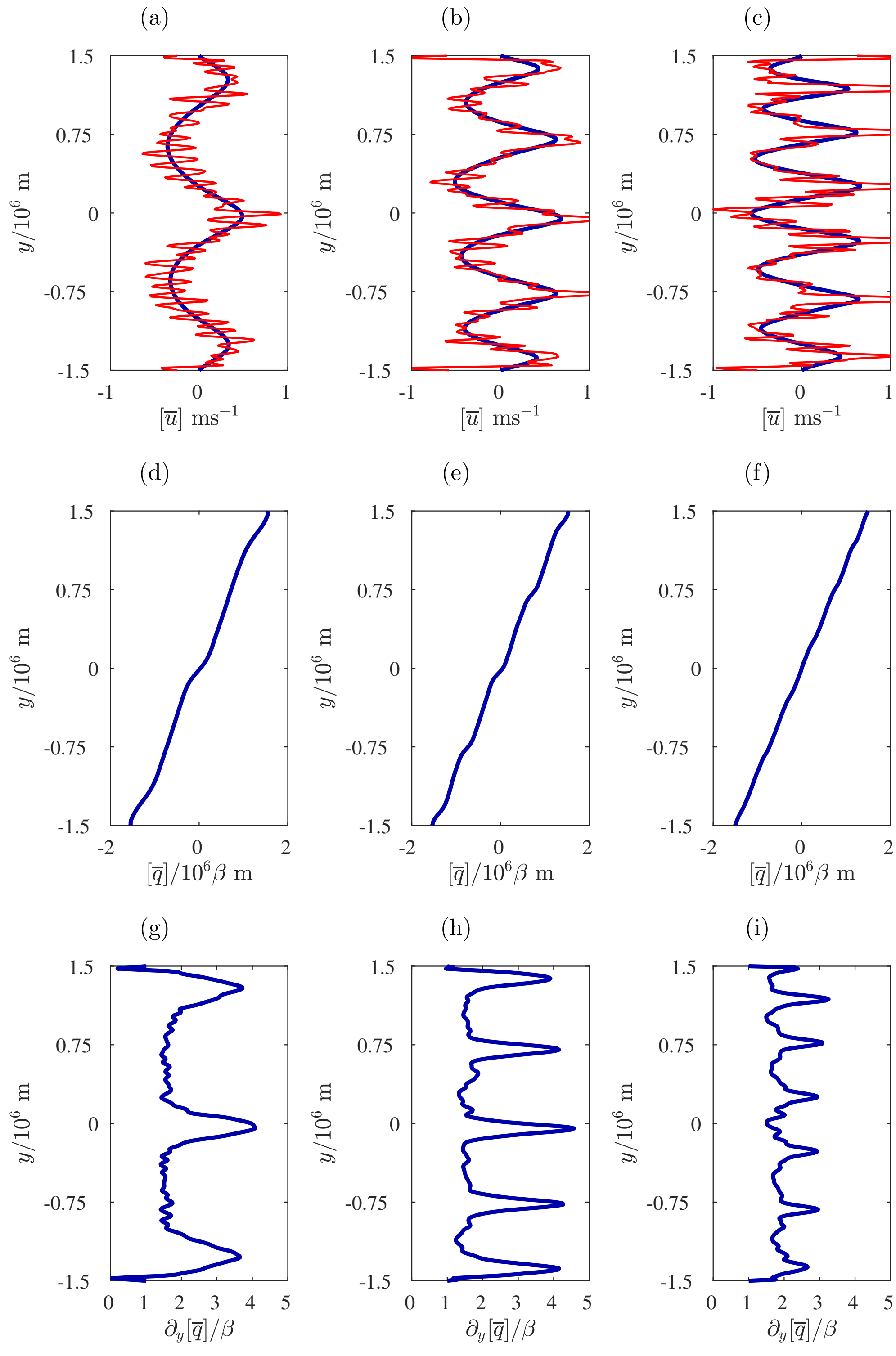

Figure 5.3.5: $[\overline{u}]$ (blue solid) evaluated after the energy has equilibrated (a) $B1$, (b) $C1$ and (c) $D1$. (d), (e) and (f) are the corresponding $[\overline{q_a}]$ profiles, normalised by β. (g), (h) and (i) are $\partial_y[\overline{q_a}]$ normalised by β. Superimposed on $\overline{u}$ is the divergence of the shear stress $-r^{-1}\partial_y N$ (red solid). The time-average has been taken over a $t = 20,000$ hr equilibration period.

Table 5.3: Equilibrium wavenumbers for runs where $r = r_0$. All runs are predicted to equilibriate with energy $E^p_{\mathrm{eq}} = 0.89\ \mathrm{m^2s^{-2}}$ and from this we may calculate k_{eq} in Eq. (5.3.15a) when $\beta = 0$ and Eq. (5.3.15b) when $\beta \neq 0$. E_{eq} is the true equilibration energy and k_{eq} is calculated from this.

Run	β	k^p_{eq}	E_{eq}	k_{eq}
$A1$	0	0	0.18	0
$B1$	β_0	2.7	0.18	4.2
$C1$	$4\beta_0$	5.5	0.19	8.2
$D1$	$16\beta_0$	11.1	0.28	14.9

scale separation.

In our quasi-geostrophic system, the patterns in $[\overline{u}]$ and in $[\overline{q}]$ are interrelated. This is because Eq. (2.2.1) is dependent upon a single variable ψ, which in turn is found by inverting q; or without loss of generality q_a, the absolute vorticity, as we have assumed a constant fluid depth. This is the PV-invertibility principle. We examine this by plotting $[\overline{q_a}]$ in Fig. 5.3.5.

We see that the jet patterns observed in profiles of $[\overline{u}]$ correspond to a weak alternating pattern in $[\overline{q_a}]$ where sharp eastward jets correspond to stronger PV-gradients and broad westward jets correspond to weaker PV-gradients. As noted in other works, these patterns are quite subtle and are more like PV-"washboards" (in the language of Berloff et al. (2009b)) rather than the staircase pattern discussed in Dritschel and McIntyre (2008). Dritschel and McIntyre (2008) describes this alternating pattern as a positive feedback process. The β-plane acts as the restoring force for Rossby-waves. PV-contours are bunched closely together in the region where there are sharp eastward jets, this causes a restoring force to act towards the westward jet cores. In the region where there are broad westward jets, Rossby-waves break leading to PV-mixing. The PV-contours then weaken further in the mixed region, facilitating further mixing and strengthen on the flanks. The limiting behaviour of this is homogenised strips of PV which lead to a staircase pattern in $[\overline{q_{\mathrm{a}}}]$.

In order to understand this asymmetric jet pattern of broad westward jets interspaced with sharp eastward jets in a different way, we have calculated the Rayleigh-Kuo stability criterion Eq. (4.4.2). We plot this in Fig. 5.3.5 as $\partial_y [\overline{q_a}]$. We see that there is no limit on the stability corresponding to eastward flow which is why they are able to sharpen, but westward jets may breach $\partial_y \overline{q_a} = 0$ if they are too sharp so persisting westward structures must be broad.

We notice that the jet profiles all have eastward jets at the boundaries. In run D_1, this is less obvious in the time average velocity profiles, but the stability criterion possesses a sharp spike at the boundary suggesting there is a narrow eastward jet residing there. We reason that the system favours eastward jets at the boundaries for stability and to satisfy the boundary conditions. This fixes $\partial_{yy}\overline{u} = 0$ on the boundary. In turn, the stability criterion must equal β. Eastward jets at each boundary will ensure the stability profiles fall to the left of β.

In §4 we found that a tendency in the zonal mean flow is governed by a divergence of the shear stress Eq. (4.3.11). Upon introducing Rayleigh friction the flow will equilibrate as energy is removed from the largest scales. By switching on the linear drag term in Eq. (2.1.37) and performing a Reynolds decomposition as described in §4, we obtain the zonally averaged Reynolds decomposed, forced-damped shallow water equation:

$$\frac{\partial \overline{\mathbf{u}}}{\partial t} + \overline{\mathbf{f}_{\mathrm{h}}} = -\boldsymbol{\nabla} \cdot \mathbf{T} - r\overline{\mathbf{u}} - g\nabla\overline{\eta}. \tag{5.3.17}$$

Since, as before, $\overline{v} = 0$ then the dynamics are governed by the zonal component of the shallow water equation

$$\frac{\partial \overline{u}}{\partial t} = -\frac{\partial N}{\partial y} - r\overline{u}, \tag{5.3.18}$$

where the pressure gradient term vanishes under zonal averaging. When the flow reaches a steady state

$$\overline{u} = -\frac{1}{r}\frac{\partial N}{\partial y}. \tag{5.3.19}$$

Note that here we still taking our Reynolds average as the zonal mean and fluctuations as departures from the zonal mean. Of course in our case we also have a biharmonic diffusion term so this relationship is approximate. This tell us that our jets will be maintained by the divergence of the shear stresses. We examine this relationship in Fig. 5.3.5 for the equilibrium jet profiles of runs $B1$, $C1$ and $D1$ which have been averaged over a 20,000 hrs of the flow evolution. Over this time-average, the divergence in the shear stress broadly matches the zonal mean structure with some small variation. Shortening this time interval however produces less agreement and the relationship given by Eq. (5.3.19) no longer holds. The fact that the divergence of the shear stress produces steady jet patterns suggests a scale separation may exist between scales producing the jet patterns and the scales producing temporal variations. In Huang and Robinson (1998), for example, the flow was separated into transient and long-lived eddies, and their interactions were examined. They found that at intermediate scales, transient eddies were responsible for eddy-mean flow interactions that supported the jet structures. This is a behaviour we will examine later on in this chapter.

5.4 Spectral View

In §1 we discussed how the two-dimensional vorticity equation for an ideal fluid simultaneously conserves energy and enstrophy leading to the upscale transfer of energy following Kolmogorov scaling given by Eq. (1.2.23) and downscale transfer of enstrophy following a steep k^{-3} power-law given by Eq. (1.2.22) (Kraichnan, 1967). Since the quasi-geostrophic equation given by Eq. (1.2.13) and the 2D vorticity equation given by Eq. (1.2.17) possess the same functional form, we also argued, following Charney (1971), that they should demonstrate the same scaling laws. We should expect then for Eq. (1.2.13) to exhibit an inverse energy cascade to larger scales and a direct enstrophy cascade which is dissipated at small scales. The key difference, of course, between Eq. (1.2.13) and Eq. (1.2.17) is the β-plane which allows for the propagation of Rossby-waves. Expecting Rossby-wave mechanisms to dominate energy transfer at the largest scales Rhines (1975) introduced the steep k^{-5} power-law given by Eq. (1.2.35), which has since been observed to exist on the k_y-axis of the energy spectrum (Chekhlov et al., 1996). Intuitively this makes sense since we expect Rossby waves to funnel energy towards zonal modes, which should result in a build up of energy at $k_x = 0$. By observing the appearance of coherent structures which grow in time and estimating the energy fronts $k_{\min}$ associated with the Kolmogorov scale given by Eq. (5.3.6) and the Rhines scale set by Eq. (1.2.31), we have seen evidence for the transfer of energy to the largest scales. In this section we will examine in closer detail the spectral evolution of the energy cascade and the associated scaling laws, following closely and building upon analysis in Sukoriansky et al. (2007) in which ideas were collated from previous works i.e. Chekhlov et al. (1996); Galperin et al. (2006); Huang et al. (2001); Huang and Robinson (1998); Sukoriansky et al. (2002).

We rewrite Eq. (1.2.35) making explicit its location near the k_y-axis:

$$E_Z\left(k\right) \approx C_\beta \beta^2 k_y^{-5}, \tag{5.4.1}$$

where C_β is an $\mathcal{O}\left(1\right)$ constant, and ask how this relates to the Rhines scale Eq. (1.2.31). Often this scale is thought to coincide with the point where turbulent energy is relinquished to Rossby-waves which propagate according to the dispersion relation given by Eq. (1.2.29), this is commonly described in the literature as an "arrest" of the cascade. As have seen in Fig. 5.3.4, the temporal evolution of the energy front for continuously forced systems under the β-plane, dictated by Eq. (5.3.11), does significantly slow down at larger scales. This effect is stronger as we increase β. But the propagation of $k_{\min}$ to the largest scales is never actually stopped since there is nothing stopping energy from travelling to the largest scales when $\beta \neq 0$. The only restriction is that energy transfer in the latter must occur anisotropically which is what causes the process to slow down but not stop. Secondly, this picture presents a rather simplistic view, since is it based on the assumption that once turbulent frequencies are low enough to excite linear Rossby waves, the flow follows linear dynamics at scales larger than this. We can plainly see from the highly turbulent nature of our flow fields, that this is incorrect! Strong non-linearity exists throughout the flow dynamics, in turn presenting a slew of complications such as the fact that linear Rossby waves may excite additional slave waves (zonons) (Sukoriansky et al., 2008) and that turbulence and Rossby waves may coexist over a wide range of scales. We will not dwell on these details here, but mention this to illustrate that this wide-held interpretation of the Rhines scale, as a sharp transition point between waves and turbulence, is inaccurate.

However, the fact that the Rhines scale reliably calculates the number of jets in the system is not a coincidence. Arguments from traditional theories of 2D turbulence lead us to conclude that most of the energy in the system will reside at $k_{\min}$, the smallest wavenumber occupied by energy and the wavenumber containing the largest amount of energy in the system. Now, for systems under the β-plane, the steep k^{-5} spectrum develops only in the vicinity of the k_y-axis, outside of this, we expect the spectrum to be Kolmogorov-like. As we can see from Eq. (5.4.1), it is possible that if β is sufficiently large, the amount of energy contained in the k_y-axis may exceed that of the rest of the system. In this case then $k_{\min}$ will not reside at the peak of the Kolmogorov spectrum, as we previously assumed, it will reside at the peak of the steeper Rhines spectrum. We obtained the Kolmogorov wavenumber Eq. (5.3.6) by integrating the Kolmogorov spectrum over wavenumber space to find the total energy, we now do the same with the Rhines spectrum given by Eq. (5.4.1) to obtain

$$E_{\mathrm{m}} \approx \int_{k_{\min}}^{k_f} E\left(k_y\right) dk_y \approx \int_{k_{\min}}^{k_f} \beta^2 k_y^{-5} dk_y = \beta^2 k_{\min}^{-4}. \tag{5.4.2}$$

Substituting for U_{rms} using Eq. (5.3.5) we find that

$$k_{\min} \propto \sqrt{\frac{\beta}{2U_{\mathrm{rms}}}} \equiv k_R. \tag{5.4.3}$$

So the Rhines scale's dynamical significance is that it describes the movement of the energy front along the k_y-axis *after* the point at which energy contained within the k_y-axis exceeds that of the rest of the spectrum. Because the energy along k_y follows different scaling laws to the rest of the spectrum, it is helpful for us to divide the total energy spectrum into zonal $E_Z\left(k\right)$ and residual $E_R\left(k\right)$ components where

$$E_Z(k) = C_\beta \beta^2 k^{-5}, \text{ when } \phi = \phi_Z, \tag{5.4.4a}$$

$$E_R(k) = C_K \epsilon^{-\frac{2}{3}} k^{-\frac{5}{3}}, \text{ when } \phi \neq \phi_Z, \tag{5.4.4b}$$

$$E(k) = E_Z(k) + E_R(k), \tag{5.4.4c}$$

where $\phi = \arctan(k_x/k_y)$ is the angle measured from the zonal axis. We have also introduced the zonal angle ϕ_Z which is the size of the wedge around the k_y-axis that contains zonal energy. In general we find that ϕ_Z is smaller as β increases. From this we can find the transition point in the total spectrum, the wavenumber at which the energy along the zonal spectrum exceeds that in the residual spectrum. This transition point is obtained by equating the two spectra Eq. (5.4.4a) and Eq. (5.4.4b)

$$k_\beta = \left(\frac{C_\beta}{C_K}\right)^{\frac{3}{10}} \left(\frac{\beta^3}{\epsilon}\right)^{\frac{1}{5}} \approx 0.5 \left(\frac{\beta^3}{\epsilon}\right)^{\frac{1}{5}}. \tag{5.4.5}$$

where $C_\beta \sim 0.5$ and $C_K \sim 5-6$ have been empirically determined (Sukoriansky et al., 2002). This is the anisotropic wavenumber, first derived in Maltrud and Vallis (1991), which is static for systems with constant ϵ, regardless of whether there is Rayleigh friction. Note this is not to say that for length scales where $k > k_\beta$ the system is isotropic. Rather that we expect zonal energy to dominate for length scales exceeding k_β.

5.4.1 Spectral Evolution

We examine the spectral evolution of continuously forced, undamped runs A_0, B_0, C_0 and D_0, in Fig. 5.4.1. The forcing scale is positioned at $k_f = 64$ where there is a spike in the spectrum. In all cases the spectra exhibit a self-similar growth in time as most of the energy cascades to the largest scales from k_f. This results in the establishment of the Kolmogorov spectrum very early on with energy peaking at $k_{\min}$ for all runs except D_0. For this case, the energy growth is initially very stunted due to its sensitivity to the biharmonic dissipation. After overcoming the dissipation, the flow almost immediately follows the Rhines spectrum. In all cases, the biharmonic dissipation suppresses the enstrophy cascade such that it does not develop a k^{-3} scaling law, though this spectrum has historically been rather elusive (Tran and Bowman, 2003). Runs in which $\beta \neq 0$ steepen towards the Rhines spectrum at higher wavenumbers as β increases. The wavenumber at which the steepening should occur is at the predicted anisotropic wavenumber k_β^p, set by Eq. (5.4.5) which is tabulated for each run in Table 5.4. From examining Fig. 5.4.1 we see that spectral steepening occurs in the vicinity of k_β^p for each run, when $\beta \neq 0$. Owing to the fact that k_β is more sensitive to changes in β than to

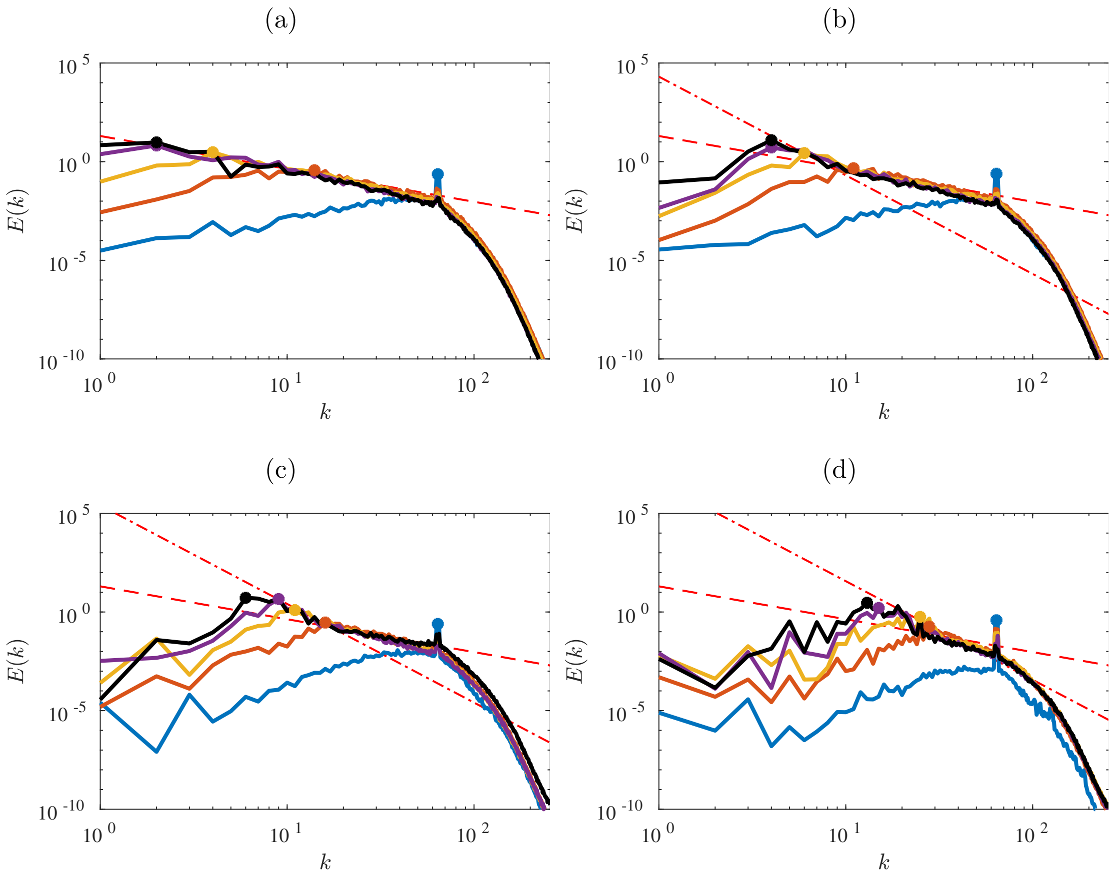

Figure 5.4.1: $E(k)$ at different stages in the evolution of the flow for runs A_0 (a), B_0 (b), C_0 (c) and D_0 (d) at times $t = 2,000$ hrs (solid blue), $t = 8,000$ hrs (solid orange) and $t = 14,000$ hrs (solid yellow), $t = 20000$ hrs (solid purple) and $t = 26000$ hrs (solid black). We also mark the position of the energy front at these times with an asterisk of the corresponding colour, calculated with Eq. (5.3.1). The spectra given by Eq. (5.4.4b) (dashed red) and Eq. (5.4.4a) (dot-dashed red) are also shown with k_β as the position where these two spectra cross.

those in ϵ, the agreement turns out to be better than expected given we have found that ϵ_{eff}, the effective energy injection rate, is smaller than ϵ and the energy growth is not strictly linear in time. So calculating k_β^p still provides a good indication of the anisotropy in the system even if it is not exact. We have seen previously that the initial development of the zonal structures in Fig. 5.3.2 and the propagation of the estimated energy fronts in Fig. 5.3.4 are very similar for runs A_0 and B_0 though the latter has $\beta \neq 0$. This is probably because the system for the latter possesses a cross-over wavenumber $k_\beta^p = 7$, which is close to the domain scale and the flow only develops significant anisotropy once its approached the largest scales. We see then that the differences between the two spectra are only obvious for the later stages of the flow evolution at times $t = 20,000$ hrs and after. At this point, a peak develops in the spectrum for run B_0, upscale from k_β^p with a steepness tending towards the

Table 5.4: The predicted anisotropy wavenumber k_β^p calculated using Eq. (5.4.5). Run A_0 where $\beta = 0$ does not have a meaningful k_β^p and so this is undefined.

Run	β	k_β^p
$A0$	0	
$B0$	β_0	7
$C0$	$4\beta_0$	16
$D0$	$16\beta_0$	37

Rhines spectrum. Spectral steepening also occurs in run C_0 but further downscale because $k_\beta^p = 16$ in this case. Run C_0 also reaches its anisotropic wavenumber much earlier on in its evolution around $t = 8,000$ hrs, after initially following the Kolmogorov spectrum.

The development of the energy spectrum is stunted for run D_0, where $k_\beta^p = 37$. This scale is relatively small but still sits a few decades upscale from the forcing wavenumber. This suggests that our calculation for k_β^p, for this run, may be less reliable than others. The reason run D_0 shows poorer agreement with k_β^p than the other runs with $\beta \neq 0$, is due to its sensitivity to the biharmonic. This would result in a smaller ϵ_{eff} which in turn would place k_β at a higher wavenumber. At later times, the spectrum only marginally progresses and the steep Rhines spectrum is evident over all wavenumbers.

In Fig. 5.4.1 we also plot explicitly the position of the energy front $k_{\min}$ associated with each of the times plotted. This we calculate as the most energetic wavenumber. The progression of $k_{\min}$ in time generally follow the scaling laws given by Eq. (5.4.4) after progressing from the forcing scale, which is the high-wavenumber spike.

The energy fronts for run A_0 follow an entirely Kolmogorov scaling for each of the times plotted. By $t = 20,000$ hrs, the front approaches the domain scale and only then does its propagation slow, which is why $k_{\min}$ at $t = 20,000$ hrs and $t = 26,000$ hrs are the same. This agrees well with the estimated evolution of k_{KBK} in Fig. 5.3.4a and the observation that the condensate consisting of two opposite signed vorticies, quickly develop in Fig. 5.3.2a.

The energy fronts in run B_0 occupy nearly identical wavenumbers to run A_0 during its initial development, when $t = 2,000$ hrs and $t = 8,000$ hrs. This agrees well with our observations in physical space, that the emergence of isotropic coherent structures occur at similar times. The frontal evolution for A_0 and B_0 only differ after the flow in B_0 reaches k_β^p. The spectral peak at $t = 20,000$ hrs lies at a higher wavenumber than for run A_0 and the front progression is

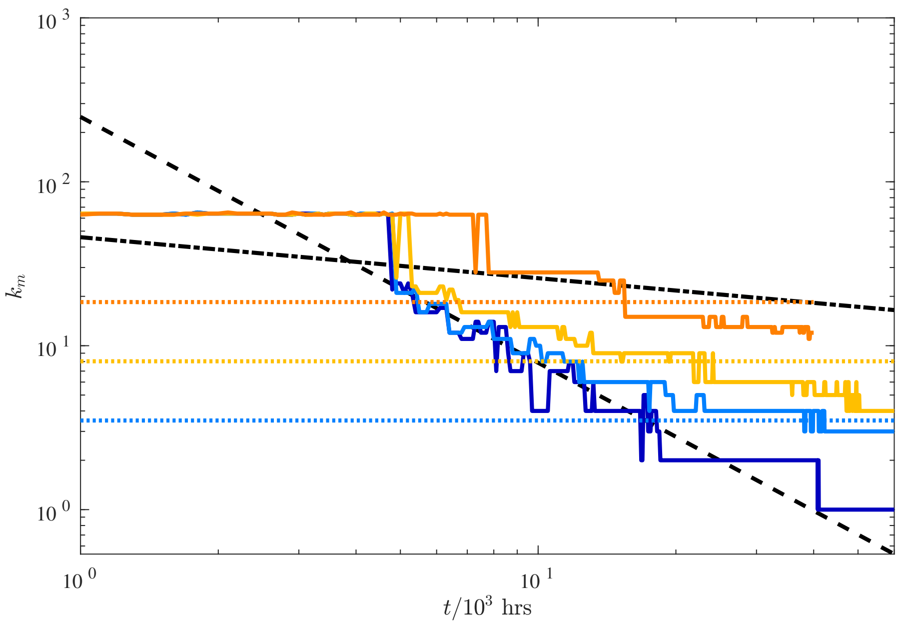

Figure 5.4.2: Evolution of the energy front $k_{\min}$ for runs A_0 (dark blue) B_0 (light blue) C_0 (yellow) and D_0 (orange). The lines are not smooth because the wavenumbers are discrete. Also marked are the predicted slopes of the time-dependences $t^{-2/3}$ (dashed black) and $t^{-1/4}$ (dot-dashed black) corresponding to $\beta = 0$ and $\beta \neq 0$ respectively. The horizontal dotted lines mark the position of k_β for each run where $\beta \neq 0$.

significantly slower as $k_{\min}$ traces the Rhines spectrum. The energy at lower wavenumbers fall off rapidly in comparison to run A_0. The reason that $k_{\min}$ is the same at $t = 20,000$ hrs and $t = 26,000$ hrs is because our wavenumbers are discrete and energy accumulation slows significantly when the Rhines spectrum begins to develop, unlike the spectrum for A_0, where the front progression is affected by the domain geometry.

The progression of the energy front for run C_0 is generally slower than that of runs A_0 and B_0 with $k_{\min}$ at later times positioned along the Rhines spectrum. This coincides with energy dropping off after $k_{\min}$ sharply as the front progresses

The energy front D_0 progresses very slowly in comparison to the other runs, the energy front appears to trace the Rhines spectrum very slowly. This agrees well with the observations of fine jet structures emerging quickly but developing slowly in Fig. 5.3.2d.

Earlier in the chapter, we estimated the positions of $k_{\min}$ from U_{rms} as they evolved in time and we have examined the positions of the energy fronts as the spectra grow self-similarly in Fig. 5.4.1. In Fig. 5.4.2 we explicitly plot the evolution in time of $k_{\min}$ for each run. The early time stagnation of all runs at the forcing scale ($k_f = 64$) is due to energy removal by the biharmonic. The plots do not show smooth relationships because the wavenumbers are discrete. Run A_0 progresses the quickest after overcoming the biharmonic and follows closely a $t^{-3/2}$ time-dependence that we expect from Eq. (5.3.8) until domain effects become significant and the front progression begins to shallow at the condensate scale $k = 1$.

We have seen that for runs with $\beta \neq 0$ and at scales where $k_{\min} < k_\beta$, the energy front should follow the Rhines scale with a time-dependence given by Eq. (5.3.11). Comparing this to Eq. (5.3.8)—the time-dependence when $\beta = 0$—the front should propagate more slowly when the flow crosses k_β. $k_{\min}$ for run $B0$, initially evolves similarly to that of run $A0$ following the $t^{-3/2}$ power-law. At $t \approx 9000$ hrs the front begins to slow down and shallow towards the $t^{-1/4}$ spectrum. The transition towards the $t^{-1/4}$ slope occurs gradually at a time earlier than when the flow approaches k_β^p, where this wavenumber appears to mark the end of the transition period. This is not surprising since we expect the true value of k_β to be higher.

The energy front appears to feel the β-plane for most of its evolution in run C_0, as it gradually shallows towards the $t^{-1/4}$ for the first ≈ 9000 hrs. The transition process continues for a short while after it approaches k_β^p, after which point it follows a $t^{-1/4}$ dependence associated with the spectral steepening we have observed. The front evolves very slowly after overcoming the biharmonic for run D_0 appearing to follow the $t^{-1/4}$ slope for the entirety of its evolution and k_β^p does not appear indicative of a transition point in this case.

We notice how for runs B_0 and C_0, coherent zonal structures in physical space emerge at times much earlier than when their respective energy fronts cross k_β^p suggesting that there should be some evidence of spectral anisotropy further downscale from this. We have also seen that the transition in the progression of $k_{\min}$ between the Kolmogorov time-dependence given by Eq. (5.3.8) and the Rhines time dependence given by Eq. (5.3.11) occurs gradually for runs B_0 and C_0. To understand this we divide the total spectrum (Eq. (5.4.4c)) into its zonal (Eq. (5.4.4a)) and residual (Eq. (5.4.4b)) components and plot the movement of the zonal energy front $k_{\min}^z$ and residual energy front $k_{\min}^r$ in wavenumber space in Fig. 5.4.3.

For run A_0 it is most instructive to take our zonal angle $\phi_Z = \pi/4$ in Eq. (5.4.4a). This implies that energy densities associated with $k_{\min}^z$ and $k_{\min}^r$ are the same in a fully isotropic system. We see that that total energy spectrum follows a Kolmogorov cascade $E\left(k_{\min}^z\right) \approx E\left(k_{\min}^r\right)$ in run A_0 such that fronts both follow Kolmogorov scaling through out their evolution and are equal in magnitude.

We also set $\phi_Z = \pi/4$ for run B_0 and at small scales the fronts follows the same behaviour as A_0, with both fronts containing the same amount of energy and following Kolmogorov scaling. Before the flow reaches k_β^p, $k_{\min}^z$ steepens towards the Rhines spectrum and begins to trace it. As the Rhines spectrum becomes established, the development of $k_{\min}^r$ stagnates. This explains why we see the

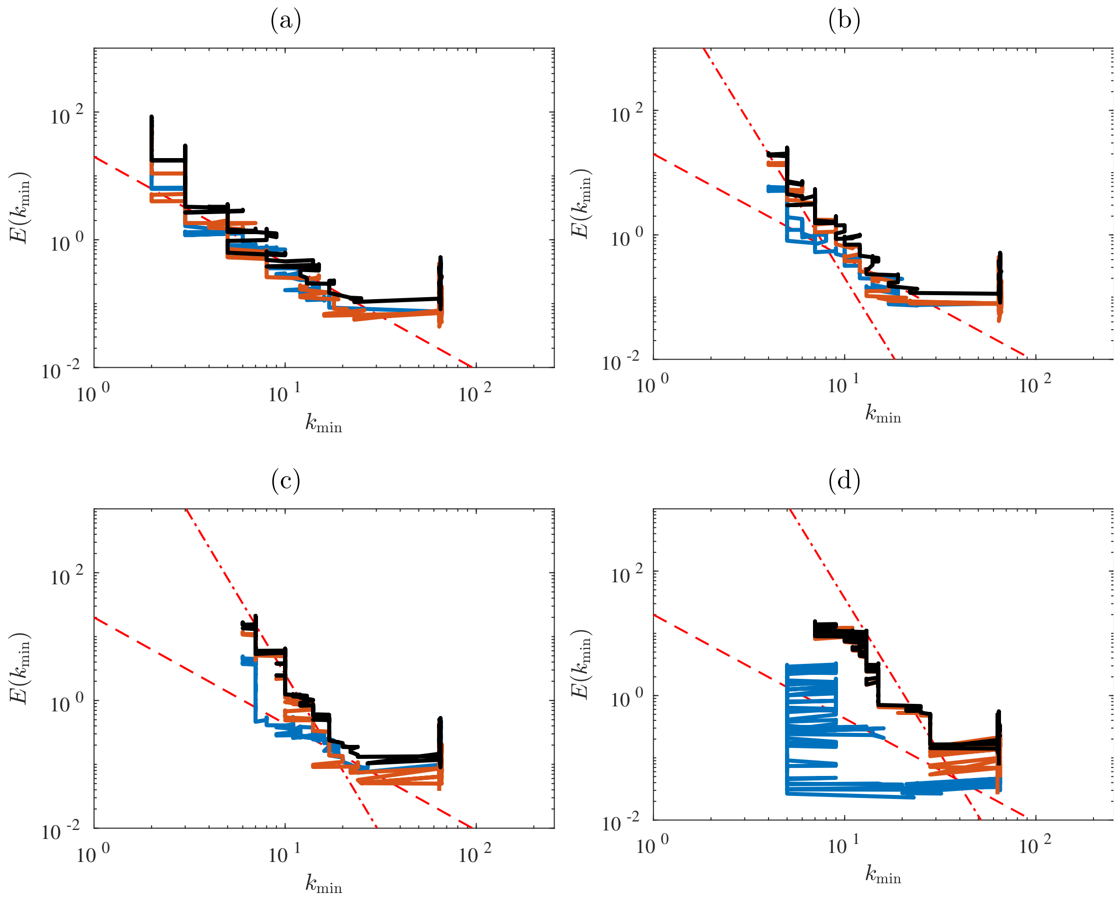

Figure 5.4.3: The energy density at $k_{\min}$ corresponding to spectrum $E(k)$ (black solid) divided into that of $E_Z(k)$ (orange solid) and $E_R(k)$ (blue solid), for runs A_0 (a), B_0 (b), C_0 (c) and D_0 (d). All runs have been spun up over a 40,000 hrs period. As in Fig. 5.4.1, we also plot the spectra Eq. (5.4.4b) (red dashed) and Eq. (5.4.4a) (red dotted) and k_β is the point at which these two spectra cross. ϕ_Z in Eq. (5.4.4) is taken to be $\pi/4$ for run A_0 and B_0, $\pi/6$ for run C_0 and $\pi/8$ for run D_0.

emergence of jet structures at times earlier than when the front has reached k_β. Spectral anisotropisation, although not the dominant process, occurs at smaller scales and the flow approaches these scales a lot earlier in their evolution. For run C_0 we have taken our zonal angle $\phi_Z = \pi/6$. This is because runs with increasing β funnel energy towards zonal modes over a narrower range of angles. $k^r_{\min}$ follows a Kolmogorov scaling in its evolution. We see that despite being defined using a smaller ϕ_Z, $k^z_{\min}$ steepens very early on in its flow evolution and begins to cross the residual at around k^p_β. After this point it follows a distinctive k^{-5} law. As we have seen for run B_0, we see that shortly after the Rhines spectrum has been established, the development of $k^r_{\min}$ stagnates. Our zonal angle is narrower still for run D_0 at $\phi_Z = \pi/8$. Beyond the forcing scale, the zonal spectrum steepens considerably immediately following the Rhines spectrum, containing more energy than the residual for the entirety of the flow evolution. The growth of the residual spectrum is stunted throughout the flow evolution and there is no evidence of Kolmogorov scaling.

Since we are dealing with an anisotropisation process in the energy spectrum it is useful to examine full 2D evolution of the energy density in wavenumber space $E(k_x, k_y)$ which we plot in Fig. 5.4.4. At $t = 2,000$ hrs and $t = 8,000$ hrs, run A_0 progresses isotropically, where energy transfer is a function of k only except along the k_x-axis where these modes cannot be populated in this domain geometry. At $t = 20,000$ hrs, energy begins to pile up at the largest available mode in the system $k = 1$. At $t = 2,000$ hrs, the energy distribution of B_0 looks similar to that of A_0. At $t = 8,000$ hrs the energy distribution of run B_0 develops a small dumbbell pattern which appears around the largest wavenumbers, but the rest of the spectrum looks similar to that of A_0. This is a signature of β-plane turbulence discussed first in Vallis and Maltrud (1993) and an indication that Rossby-waves have become excited. This coincides with the steepening of the zonal spectrum and jet structures begin to appear shortly after this. By $t = 20,000$ hrs, the dumbbell is localised near the lowest modes and the energy distributions for runs A_0 and B_0 look similar on first glance. The difference, however, is that a larger proportion of the total energy resides in the vicinity of the meridional axis than the residual in run B_0.

Rossby-wave propagation is evident as early as $t = 2,000$ hrs for run C_0, where we already see a faint dumbbell structure emerging. By $t = 8,000$ hrs a dumbbell pattern spanning a larger area than for B_0 has been established. Energy appears to have circumvented this region and is being funnelled towards the k_y-axis. By $t = 20,000$ hrs the dumbbell structure appears to shrink but there is more energy contained in the vicinity of the k_y-axis and over a smaller range of angles than for run B_0. It is also spread over a larger range of meridional wavenumbers although, the energy does not penetrate the lowest modes.

For run D_0, we notice that energy is already progressing along the k_y-axis at $t = 2,000$ hrs whilst the rest of the spectrum develops very little. One could imagine that that there is a dumbbell pattern attributed to this that extends beyond the forcing scale. This suggests that Rossby-waves have been excited almost immediately. At $t = 8,000$ hrs the dumbbell is smaller but still spans a large portion of the inertial ranges which correspond to the stunted development of the residual energy front in Fig. 5.4.3 for this run. Energy along the k_y-axis however progresses more quickly. At $t = 20,000$ hrs, the dumbbell structure is smaller but most of the energy in the system, which has been funnelled towards zonal modes, now resides inside a narrow wedge around the k_y-axis spanning a large range of scales.

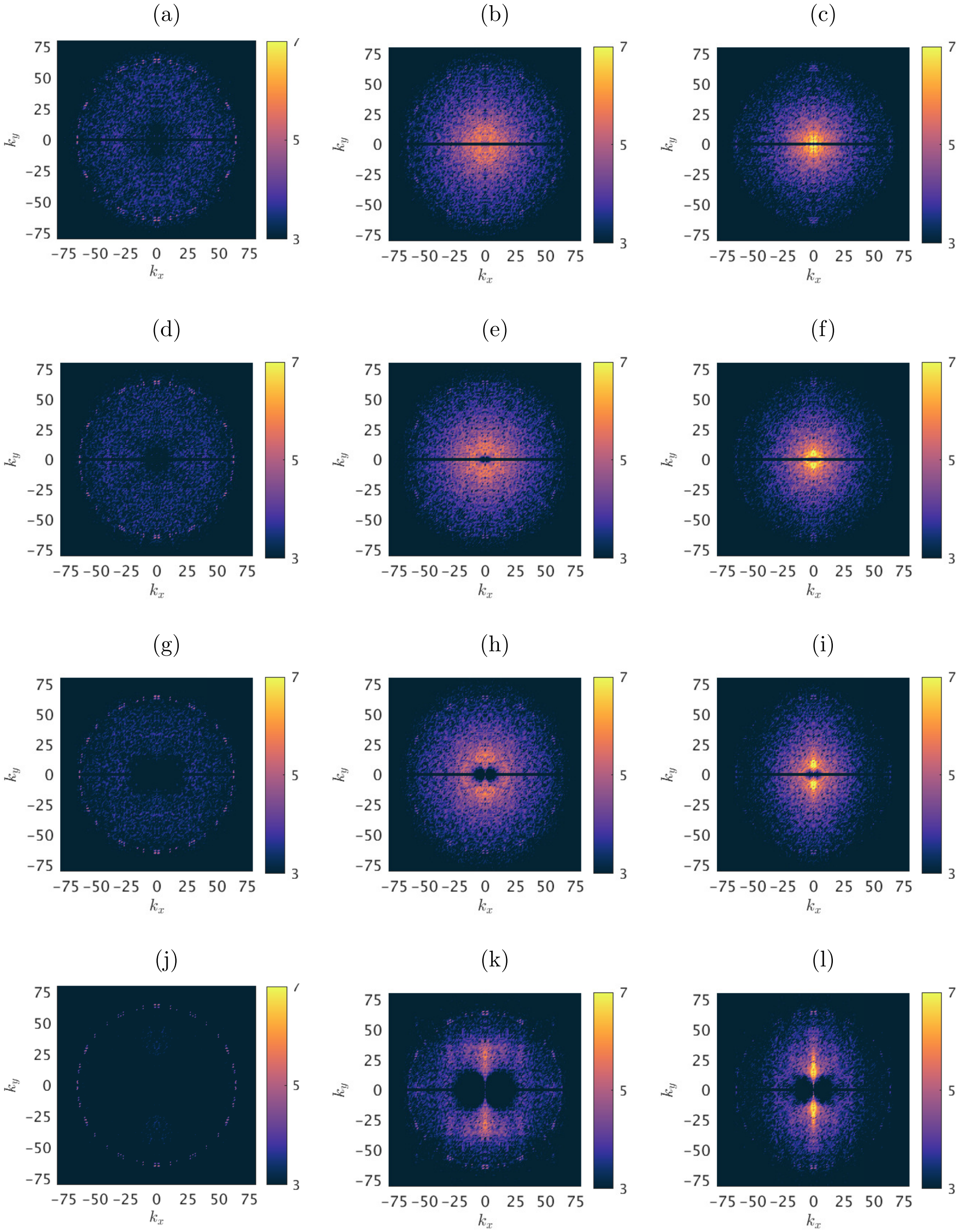

Figure 5.4.4: $\log|E(k_x, k_y)|$ for runs A_0 (a), (b) and (c); B_0 (d), (e) and (f); C_0 (g), (h) and (i); D_0 (j), (k) and (l), at $t = 2,000$ hrs, $t = 8,000$ hrs and $t = 20,000$ hrs respectively.

5.4.2 Steady State Spectra

Rayleigh friction causes the energy to eventually equilibrate. We have discussed how the propagation of k_{min} should then halt at k_{eq}, calculated from the system's equilibrium energy E_{eq} using Eq. (5.3.15). These are tabulated in Table 5.3 for each run. We have also found that the number of jets counted in the equilibrium velocity profiles of Fig. 5.3.5, for runs B_0 and C_0 approximately correspond to k_{eq}. In this section we will tie these observations in to the spectral viewpoint.

In Fig. 5.4.5 we examine the steady state spectra over the $t = 20,000$ hrs equilibration period for each equilibrated run. The spectrum for run A_1, $E(k)$ follows Kolmogorov scaling at all scales. $E_Z(k)$ and $E_R(k)$ also follow Kolmogorov scaling and are of comparable size throughout the spectrum, except at the largest scales where the zonal spectrum steepens slightly. This suggests that the flow is mostly isotropic save for some domain effects. The spectral peak of $E(k)$ resides at $k_{\text{min}} = 2$ where $E_Z(k)$ and $E_R(k)$ contribute approximately equal energy to this mode. However k_{min} does not reside at the calculated equilibrium wavenumber $k_{\text{eq}} = 0$. This discrepency arises because the assumptions on which Eq. (5.3.15a) was derived break down at the largest scales. Firstly, $k = 0$ is physically unrealisable in our system where $k = 1$ is the largest available scale. Also, as we have seen in our continuously forced systems, the flow begins to feel the boundaries at the lowest scales causing the propagation of k_{min} to slow down at the smallest wavenumbers. Together these result in Eq. (5.3.15a) underestimating k_{eq} if the flow is close to the domain scale.

The spectra for run B_1, $E(k)$ and its constituent spectra $E_Z(k)$ and $E_R(k)$ are similar to that of A_1 for wavenumbers $k \gg k_\beta$, where $E_Z(k)$ and $E_R(k)$ contain comparable energy. A short distance upscale from k_β^p, $E(k)$ sharply rises to a peak $k_{\text{min}} = 5$ that resides on the Rhines spectrum. This is exactly equal to the number of equilibrium jets we count in the velocity profile. We also see that the steady steepening of $E_Z(k)$ towards the Rhines spectrum is responsible for this peak whilst $E_R(k)$ lies along the Kolmogorov spectrum. $E_Z(k)$ then gradually begins to peak downscale from k_β^p. Both spectra fall off at the largest scales. The spectral peak also agrees well with our calculated $k_{\text{eq}} \approx 4$.

In run C_1, $E(k)$ follows the Kolmogorov spectrum until k_β where it steepens and follows the Rhines spectrum over $8-10$ wavenumbers. The peak finally settles at $k_{\text{min}} = 9$ which equals the number of jets observed, though considerable energy has still accumulated at $k = 6-8$, suggesting that we have damped the system at a point where it is attempting to transition to a different jet configuration. $k_{\text{eq}} \approx 8$ which agrees roughly with the number of jets observed. Since we are using a smaller ϕ_Z to define $E_Z(k)$ in run C_1, it contains less energy than $E_R(k)$ at smaller scales. Both spectra drop considerably for smaller scales.

Energy growth in run D_1 initially follows a Kolmogorov scaling which sharply peaks, touching the Rhines spectrum at scales $k \approx 15 \ll k_\beta$. The spectral peak resides at $k = 11$ which agrees with the jet number observed for this run. However, this does not coincide with the calculated equilibrium wavenumber $k_{\text{eq}} \approx 15$. We

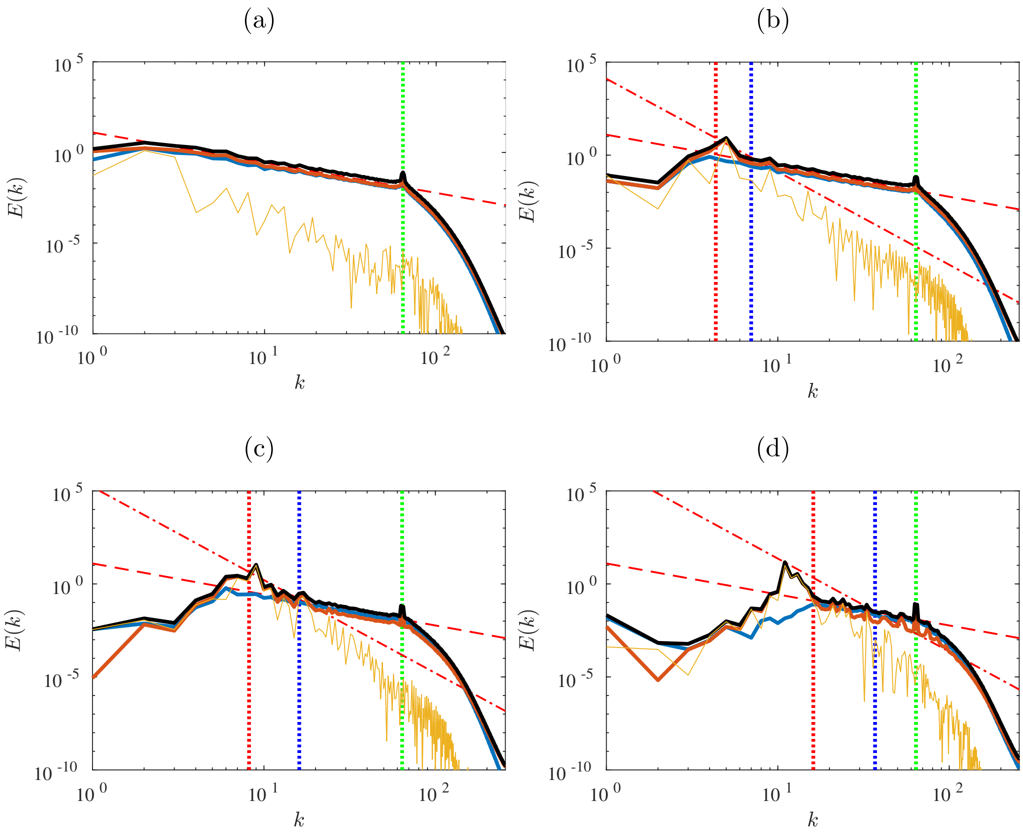

Figure 5.4.5: Time averaged spectra $E(k)$ (solid black), $E_Z(k)$ (solid orange) and $E_R(k)$ (solid light blue) for runs A_1 (a), B_1 (b), C_1 (c) and D_1 (d) over a 10,000 hrs equilibration period. k_{fr} (vertical dotted red) marks the position of the frictional wavenumber calculated from E_{eq}, k_{fr} lies at $k = 0$ for A_1 so it does not appear on the plot. We also plot the spectra given by Eq. (5.4.4b) (dashed red) and Eq. (5.4.4a) (dot-dashed red), k_β is the point at which these two spectra cross (vertical dotted blue). Also plotted is the jet spectrum $E_{\text{jet}}(k)$ (thin yellow) calculated as the energy distribution in the zonal-time average zonal velocity $[\overline{u}]$.

see that although $E_Z(k)$ is responsible for the spectral peak, its slope does not follow the Rhines spectrum, which is an assumption upon which Eq. (5.3.15b) is derived. The slope is also slightly steeper than the Kolmogorov spectrum, that $E_R(k)$ follows, breaching the latter spectrum when it sharply steepens at $k = 15$.

For run C_1 and to a lesser extent A_1, the steepness of the zonal spectrum does not follow the Rhines spectrum exactly as it is comprised of jagged spikes. This is not an effect of the discreteness of the wavespace. As discussed in Danilov and Gurarie (2004), these spikes are harmonics of the spectral peak at k_{min}. To examine how this fits in to our theory of jet formation, we also plot the jet spectrum $E_{\text{jet}}(k)$ which is a spectrum calculated from the equilibrium time-average velocity profile. In all cases, the magnitude of the spikes in $E_{\text{jet}}(k)$ match with the spikes observed in the spectra.

Run A_1 only possesses one significant peak in $E_{\text{jet}}(k)$ that corresponds to the $k = 2$ mode at which this system equilibrates. There are three significant peaks for run B_1. These peaks touch the Rhines spectrum. The first peak coincides with roughly where the residual spectrum $E_Z(k)$ begins to steepen. The jet spectrum contains a rich set of harmonics for run C_1, where there are many peaks touching the Rhines spectrum around k_β^p. There is only one significant spike in run D_1 that touches the Rhines spectrum.

In physical space we saw that jets arrange themselves in an asymmetric pattern of broad westward and narrow eastward jets. These harmonics we observe in the spectra are a signature of this pattern which requires several modes that, in superposition, produce these jet structures. We note that in run D_1 there is only one significant peak which is why the jet structure appears more symmetric in this case than for runs A_1 and B_1.

Finally it is useful to see how the 1D spectra emerge from the 2D, so we plot the energy density in wavenumber space $E(k_x, k_y)$ as shown in Fig. 5.4.6, For run

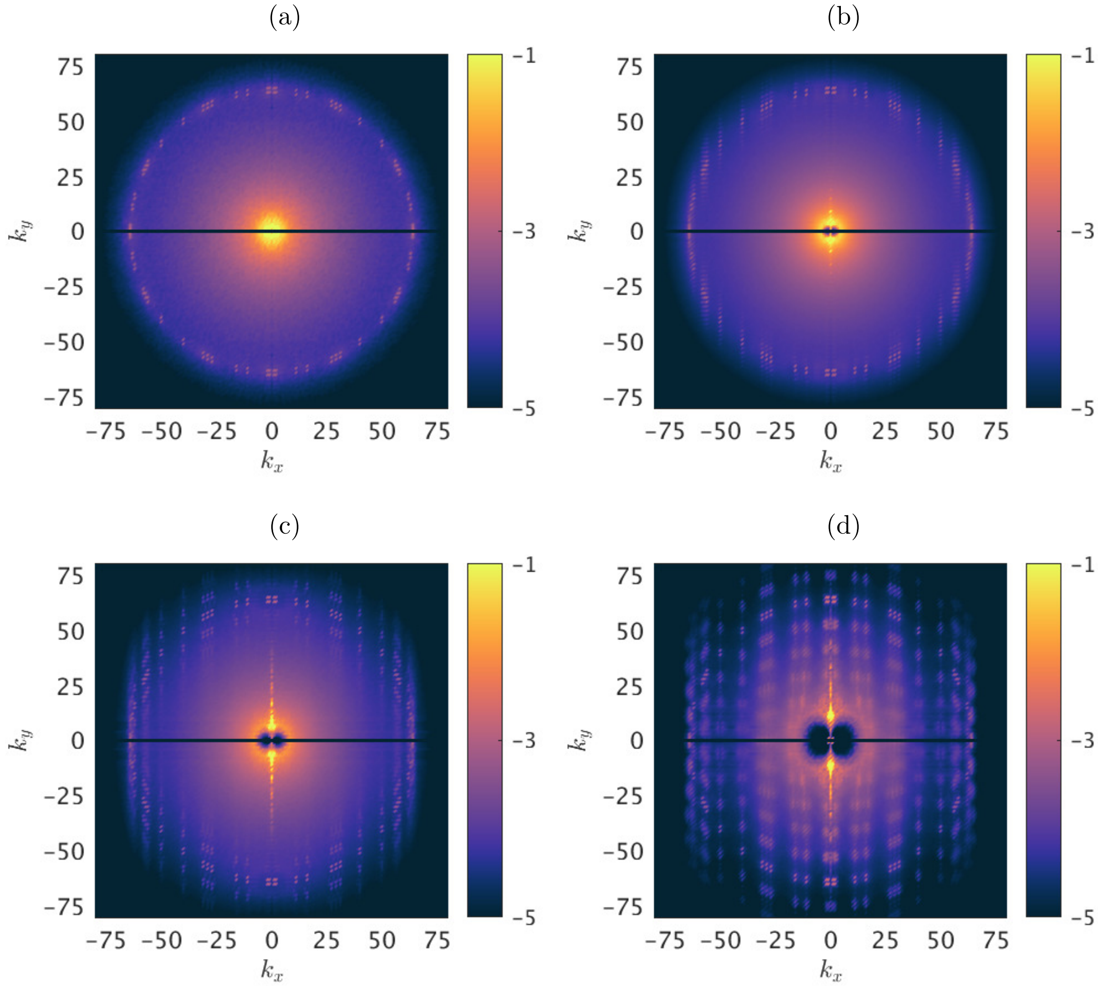

Figure 5.4.6: Time average contour plots of $E(k_x, k_y)$ for run A_1 (a), B_1 (b), C_1 (c) and D_1 (d) over a 10000 hr period.

A_1, save for the k_x-axis which is not populated because of our channel geometry, we see a smooth isotropic pattern in which the energy density is a function of its radial shell k only, with energy accumulating at the centre. Away from the largest scales located the centre of the plot, run B_1 looks very similar to run A_1 with energy distributed isotropically as function of k. As we approach the centre of the plot, along the k_y-axis there is a spike of energy corresponding to the first spectral peak in $E_Z(k)$. A small, but clear dumbbell pattern occupies the central few radial shells with most of the energy piling up along the k_y-axis. However, around the dumbbell structure there is still a large amount of energy associated with the isotropic dynamics of the Kolmogorov spectrum which provides further justification for why we chose our zonal angle ϕ_z to be so wide. In run C_1, away from the centre, the energy is a function of k everywhere except for a narrow region about the k_y-axis. Here, significant amounts of energy have accumulated far downscale from the dumbbell structure that resides close to the centre. We have associated the peaks of energy along the k_y-axis with the jet spectrum $E_{\text{jet}}(k)$. We also note that the central dumbbell is larger than that of run B_1 and there is a clear separation between the magnitude of energy that resides along the k_y-axis the rest of the energy that surrounds the dumbell structure, associated with the peak of the residual spectrum. Run D_1 shows significant anisotropy even as far as the forcing scale. A large dumbbell structure occupies the centre with very little energy surrounding it. Energy accumulation along the k_y-axis peaks sharply between the two lobes of the dumbbell. We speculate that the lack of scale separation between k_f and k_β for this run results in the spikes at the forcing scale acquiring the harmonics along the k_y-axis, leading to the pulsing pattern observed in this spectrum. This effect is seen to lesser extent in the forcing scales of the 2D spectrum for run C_1 as well.

5.4.3 Scale Separation

All simulations of β-plane turbulence we have seen in this chapter demonstrate jet formation in physical space. However, the signatures this leaves in the spectra can be more subtle if scales are not adequately separated. Ideally we would like to have scales separated according to

$$k_0 \ll k_{\text{eq}} \ll k_\beta \ll k_f \ll k_D \tag{5.4.6}$$

where k_0 is the domain scale and k_D is the dissipation scale. Flows respecting Eq. (5.4.6) are said to be in the *zonostrophic* regime Galperin et al. (2006). The last inequality simply tells us that the dissipation scale and forcing scale should be well-separated in order for there to be an enstrophy cascade. This we have seen is not the case in our system in which the biharmonic affects scales within the inverse cascade.

Runs B_0 and B_1 suffer from the first two inequalities not being respected though the third is. We have seen that although runs A_0 and B_0 clearly differ, where the former develops isotropic structures and the latter jets, the spectral evolution of both runs are nearly indistinguishable as the Kolmogorov cascade dominates most $k < k_f$ for run B_0. Only at the scales where $k < k_\beta$ was a small departure from isotropic dynamics noticeable. This departure is most noticeable in the angularly averaged energy spectra. The zonal energy contributing to the formation of zonally elongated structures is more broadly distributed over a wide angle $\phi_Z = \pi/4$ about the k_y-axis and as such, this signature is not so obvious in the corresponding plots of $E\left(k_x, k_y\right)$ especially in the late-stage evolution of B_0 where the dumbbell structure shrinks. The dumbbell structure is apparent in the equilibrated run B_1. However it spans a very small area and the energy accumulated around it, associated with k^r_{min}, appears to be of comparable size to the energy contained in k^z_{min}. If scales were adequately separated, the fronts should be expected to contain energies where

$$E_m \approx E\left(k_{\text{min}}\right) \approx E\left(k^z_{\text{min}}\right) \ll E\left(k^r_{\text{min}}\right). \tag{5.4.7}$$

The scale separation condition between k_0 and k_{eq} is clearly not satisfied for the forced damped run B_1 where $k_{\text{eq}} = 5$. We have seen that for isotropic runs A_0 and A_1 that this may cause spectral steepening that is not associated with jet formation. Furthermore, given that $k^p_\beta = 7$ for this run (though we know this scale is likely to be underestimated) this leaves little space for the Rhines spectrum to develop.

Runs D_0 and D_1 suffer the opposite issue in which the last two inequalities in Eq. (5.4.6) are not well respected. The strong β-plane results in k_β being located close to the forcing scale which in turn is affected more by the dissipation scale. This stunts the development of the isotropic portion of the spectrum in D_0 and the Rhines spectrum barely develops even after long integration periods. In run D_1 there is only a single spectral peak that touches the Rhines spectrum rather than a rich superposition of harmonics required to produce a sharp eastward and broad westward jet pattern.

Runs C_0 and C_1 demonstrate the best scale separation with the first 3 inequalities in Eq. (5.4.6) being well respected. k_β is located sufficiently far from k_f such that a Kolmogorov cascade features in all spectra. For run C_1 a Rhines spectrum containing several harmonics is allowed to span a decade of wavenumbers, corresponding to a pattern of sharp eastward and broad westward jets. The domain scale is also located several wavenumbers upscale from the largest scale in the Rhines spectrum k_{eq} such that domain affects do not obscure the spectra.

5.5 Eddy Tilt Patterns

In §4 we introduced the eddy ellipse formulation which allows us to visualise the movement of eddy momentum. By performing a principle axis decomposition on the eddy velocities we obtained the geometric properties of the ellipse shape traced by u' and v' (Preisendorfer, 1988). These encode information about the direction and magnitude of the stresses associated with the eddy distributions. In particular the tilt direction given by Eq. (4.3.16) of these ellipses informs us of the net direction of the momentum flux, providing a more intuitive sense of how eddies interact with the mean flow. This can be more informative in comparison to examining the shear stress N given by Eq. (4.3.7) and the normal stress difference M given by Eq. (4.3.6) alone. We have seen that zonal mean structures, which in our case are jets, should evolve according to the divergence in shear stress and linear drag according to Eq. (5.3.18). In §4 we examined a jet profile that was barotropically unstable and associated characteristic ellipse patterns and distributions to the growth and decay of perturbations on the jet flanks. In this section we apply the geometric eddy ellipse formulation developed in §4 to examine eddy-mean flow interactions in geostrophic turbulence.

We have seen that jets form under β-plane turbulence when flows approach scales $k < k_\beta$ and equilibrate under Rayleigh friction with jet number $k_{\text{jet}} = k_{\text{fr}}$. The flow eventually reaches a steady state and the eddy momentum flux into the jet structure should approximately balance the Rayleigh friction (Eq. (5.3.19)). We have confirmed this relationship by examining our systems after energy has equilibrated and we have seen that the shear stress divergence pattern converges to the zonal average jet structure after averaging over a time interval $T = 20,000$ hrs. We have also emphasised the importance of characteristic scales being adequately separated according to the inequality given by Eq. (5.4.6) and have discussed how run C_1 is the only one which possesses reasonable scale separation for $k < k_f$. For the rest of this section, we will analyse this run in more detail.

In §4 we examined a barotropically unstable zonal jet profile that was successively strengthened or weakened as instabilities on the jet flanks decayed and grew respectively. In contrast, we have found that the jet structures which form under the action of spectral anisotropisation by the β-plane have barotropically stable jet profiles. We expect then for the eddy ellipse patterns corresponding to the jets to be static in time in order to maintain the jet structure. It is peculiar that we only witness the relationship given by Eq. (5.3.19) after a relatively long time-averaging, when the jets form and stabilise on time-scales much shorter than this. To understand this we examine the Hovmöller plots of the momentum fluxes N, M and the ellipse quantity θ in Fig. 5.5.1 for run C_1 over $20,000$ hrs after the energy of the run has equilibrated.

Though the energy has equilibrated, we see that there are significant time-dependent processes occurring in the shear stress N, where momentum is fluxed north and south in an alternating pattern. We see however that over a time average, the shear stress possesses a pattern that is consistent with the jet structure. In particular we find eastward jets are flanked by a negative flux of eastward momentum to their north and a positive flux of eastward momentum to their south. The converse is true for westward jets. This leads to a characteristic pattern in the stress that is half a jet-width off-set from the jet structure.

The difference in normal stresses M is in general an order of magnitude larger than N. The temporal evolution of M shows a zonal structure that is time-dependent and pulsing regularly. The pulses are always positive and coincide with regions where the N changes sign in time. These pulses are located at some of the jet cores and at domain walls but do not appear to correlate with any strengthening pattern in the zonal mean structure itself. We speculate that the intermittent signal of pulses in M can be attributed to the action of the Rayleigh friction which becomes important as the jet strengthens. Both in the time evolution and the time average, M is purely zonal and does not drop below zero so there is no net meridional eddy momentum at any point in the flow over the equilibration period. Also, although there is a zonal jet pattern in the normal stress field, this structure does not match the zonal mean jet pattern in $\overline{u}$.

The resulting Hovmöller plot of the eddy tilt angle θ, calculated from M and N, does not look particularly instructive. It shows a vague time alternating pattern of net northward and net southward momentum fluxing which posses a meridional structure which is strongest at the jet cores. However, the time average shows a very clear eddy-mean flow interaction, consistent with the jet pattern, where eddy ellipses are tilted towards the jet structure in an alternating pattern on the flanks of the jets. We see then that time-dependent processes which dominate the flow mask a more subtle flow process that supports the jet structure. Our task is therefore to find the scales responsible for supporting the jet.

5.5.1 Zonal Filter

In the previous section we calculated a number of characteristic scales for run C_1. We found that scales where $k > k_\beta$ are dominated by energy in the residual spectrum Eq. (5.4.4b) and scales where $k < k_\beta$ are dominated by energy accumulation along the k_y-axis corresponding to the development of the Rhines spectrum. The latter we associate with the formation of jets. We also know that

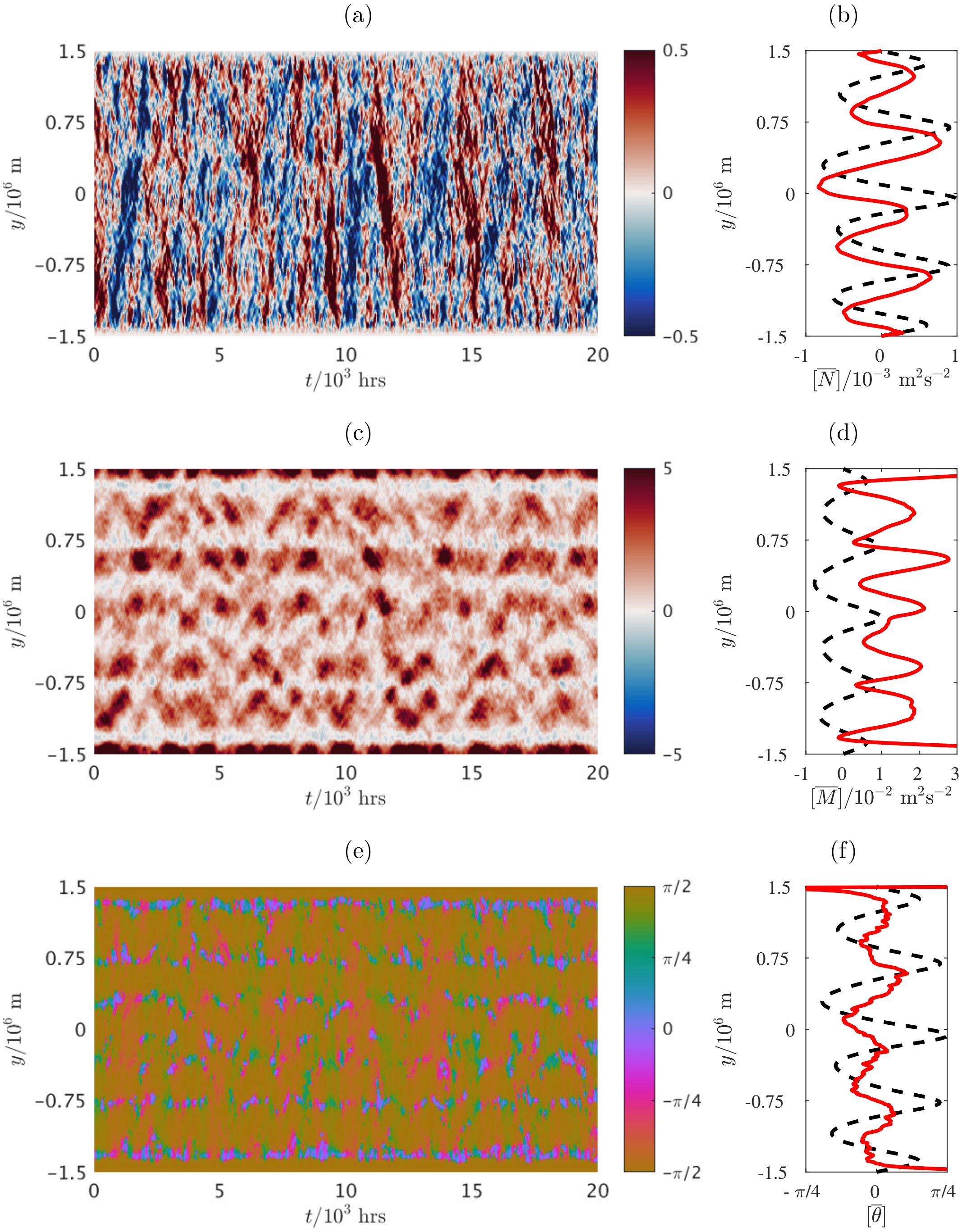

Figure 5.5.1: Hovmöller plots of the shear stress $N(y)/10^{-2}$ m^{2}s^{-2} (a) and time average $[N(y)]/10^{-3}$ m^{2}s^{-2} (red solid) (b), normal stress difference $M(y)/10^{-2}$ m^{2}s^{-2} (c) and time average $[M(y)]/10^{-2}$ m^{2}s^{-2} (red solid) (d) and the corresponding ellipse quantity $\theta(y)$ (e) and time average $[\theta]$ (red solid) (f) over a $T = 20,000$ hrs equilibration period. The normalised zonal-time average zonal velocity $[\overline{u}]/U_{\max}$ is also plotted for comparison (black dotted) where $U_{\max}$ is the maximum value of $[\overline{u}]$.

in the steady state, the number of jets are equal to the frictional wavenumber k_{eq}. Consequently, we expect that eddies supporting the jet structures will reside between the frictional scales k_{eq} and the anisostropy scale k_β. We expect that β-plane dynamics are homogeneous in x and y as the flow spins up and only develops inhomogeneity in y for scales where $k < k_\beta$. Through out the flow evolution, we expect homogeneity in x to remain. We have seen in §4 that we may isolate contributions from certain k_x wavenumbers to the stress quantities. Here we will extend this approach by developing a filter that separates the velocity correlations that contribute to the eddy stresses M and N by zonal scale.

We can exploit the homogeneity in x to find the contributions of eddy velocities of different zonal scales to the eddy stress quantities N and M. Since our flow is periodic in x we take a Fourier transform of the eddy velocities in the x-direction and substitute these into the eddy velocity correlation tensor Eq. (4.3.2), we find, by equating the zonal average of the ensemble average, that

$$T(y) = \frac{2}{L_x}\begin{pmatrix} \int_1^{k_D} |\widetilde{u'}|^2 dk_x & \int_1^{k_D} \widetilde{u'}\widetilde{v'}^* dk_x \\ \int_1^{k_D} \widetilde{v'}\widetilde{u'}^* dk_x & \int_1^{k_D} |\widetilde{v'}|^2 dk_x \end{pmatrix}, \tag{5.5.1}$$

where the tilde represents the Fourier transform in the zonal direction and we take the limit of integration from $k_x = 1$ as the eddying velocities denoted by a prime have have the zonal mean subtracted. Also we have used that since velocities are real quantities, we need only use the positive terms. From this we can rewrite M, as

$$M = M_l + M_h, \tag{5.5.2a}$$

$$\text{where } M_l = \frac{1}{L_x}\int_1^{k_c-1} \left|\widetilde{u'}\right|^2 - \left|\widetilde{v'}\right|^2 dk_x, \tag{5.5.2b}$$

$$\text{and } M_h = \frac{1}{L_x}\int_{k_c}^{k_D} \left|\widetilde{u'}\right|^2 - \left|\widetilde{v'}\right|^2 dk_x, \tag{5.5.2c}$$

and N as

$$N = N_l + N_h, \tag{5.5.3a}$$

$$\text{where } N_l = \frac{1}{L_x}\int_0^{k_c-1} \widetilde{u'}\widetilde{v'}^* dk_x, \tag{5.5.3b}$$

$$\text{and } N_h = \frac{1}{L_x}\int_{k_c}^{k_D} \widetilde{u'}\widetilde{v'}^* dk_x, \tag{5.5.3c}$$

where k_c is some threshold wavenumber and the subscripts l and h represent a low-pass and high-pass filter respectively. In Fig. 5.5.2, we plot the eddy-mean flow relationship given by Eq. (5.3.19), separating N into N_l and N_h as in Eq. (5.5.3a) for different cut-off wavenumbers k_c. What we see is that the divergence of N does not capture the jet pattern for scales where $k_c \leq k_\beta$. The low-pass filter on

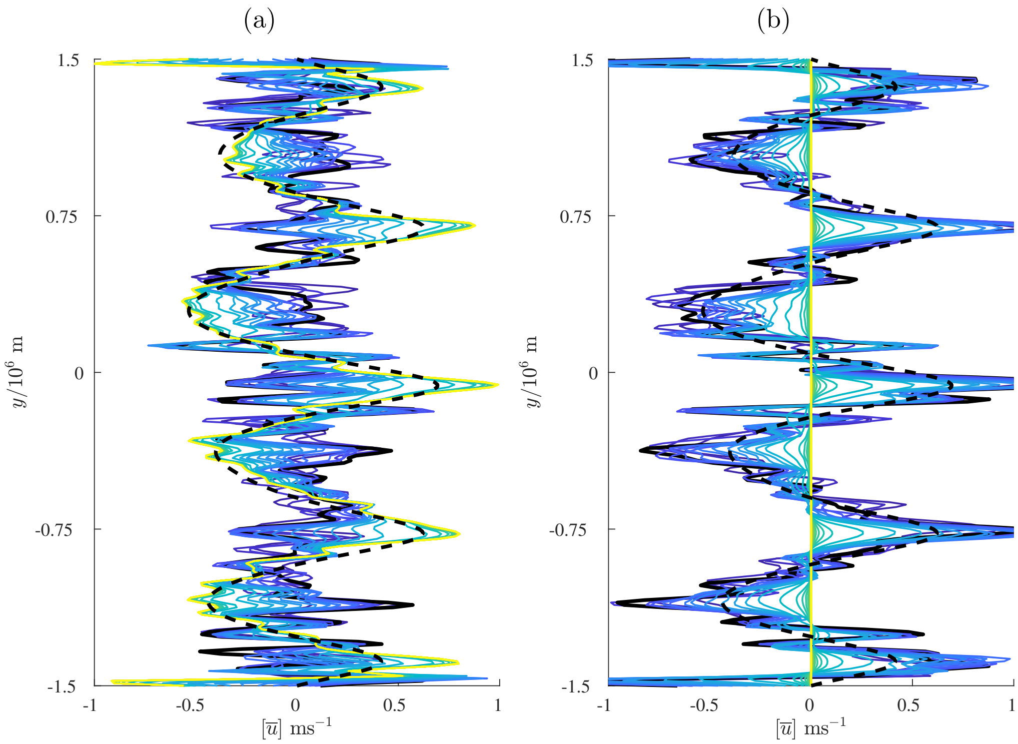

Figure 5.5.2: $[\overline{u}]$ over the $T = 20,000$ hrs equilibration period (black dotted) compared to (a) $-r^{-1}\partial_y N_l$ and (a) $-r^{-1}\partial_y N_h$. N_l is the low-pass filter on N, retaining wavenumbers between $k_x = 1$ up to cut-off wavenumber $k_c = 2, 4, 8, 16, 32, 48, 64, 256$ (dark blue to green-yellow). N_h is the corresponding high-pass filter between the same cut-off wavenumber k_x^c to $k_x = 256$ (dark blue to green-yellow) such that $N = N_l + N_h$ for each k_c. The special case, $k_c = k_\beta = 16$ is shown as the thick black line.

N is only able to captures this pattern for large values of k_c, with the structure beginning to emerge at relatively high wavenumbers $k_c \geq 32$. Below this, the signal has an amplitude comparable to the jet-scale but is noisy. In contrast, the jet pattern is evident for nearly all k_c, in the high-pass filter, with a faint, low-amplitude jet pattern still present when wavenumbers $k \geq k_f$ are retained. As k_c varies, the transition between the noisy low-wavenumbers and the appeareance of the jet-pattern in the high-wavenumbers is relatively smooth but $k_c = k_\beta$ does appear to be representative of the transition between the two regimes so we will proceed using this choice.

In Fig. 5.5.3 we examine the Hovmöller plots from the low-pass filtered stresses M_l and N_l and the tilt angle calculated from this. The Hovmöller plots of each quantity appears almost identical to that of the unfiltered quantities in Fig. 5.5.1 where it is dominated by noisy, time-dependent processes.

The Hovmöller plot of N_l demonstrates the same alternating pattern of momentum flux observed in the shear stress. Unlike the unfiltered case N, the

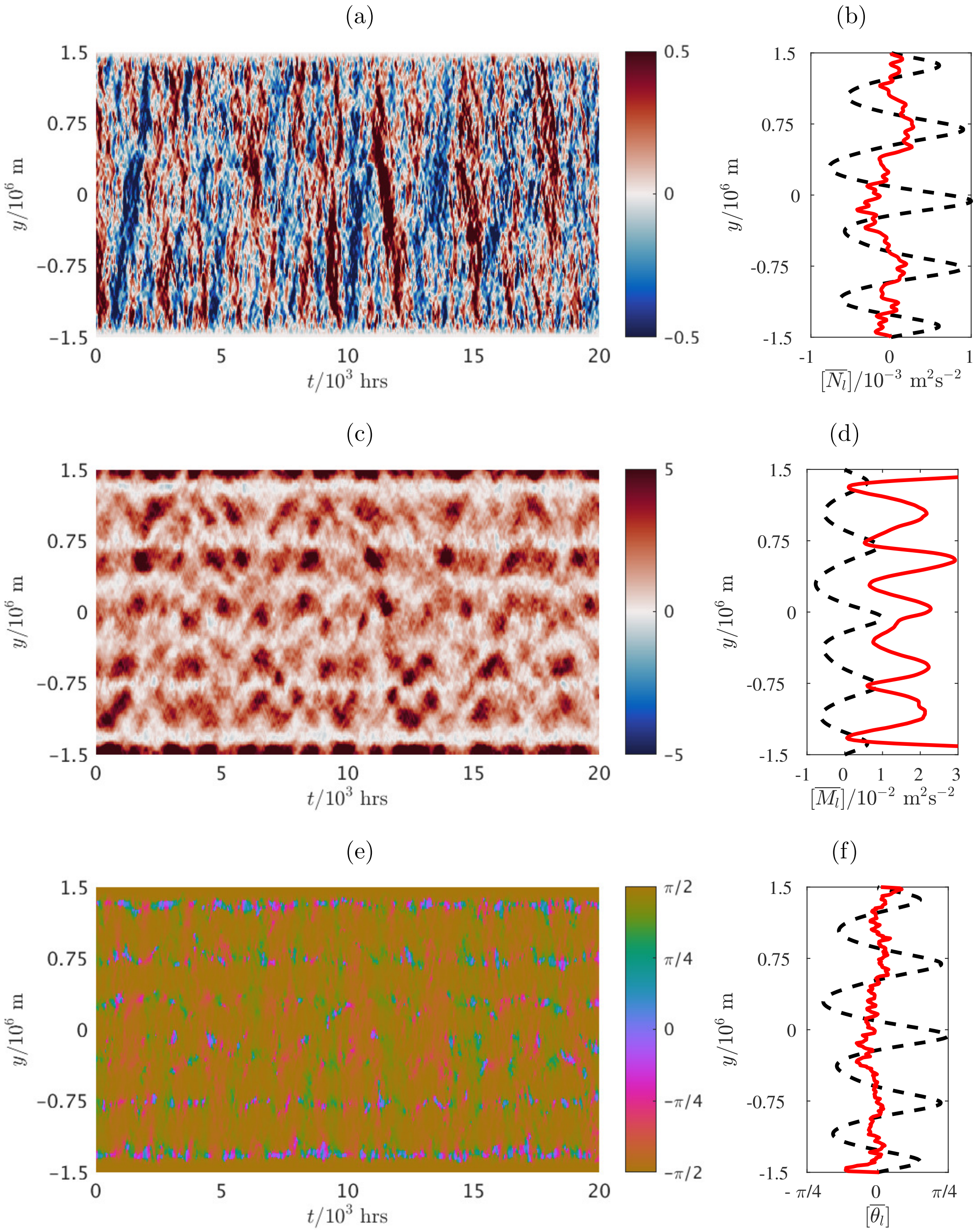

Figure 5.5.3: Hovmöller plots of the large-scale shear stress $N_l/10^{-2}$ m^{2}s^{-2} (a) and time average $[N_l]/10^{-3}$ m^{2}s^{-2} (red solid) (b), normal stress difference $M_l/10^{-2}$ m^{2}s^{-2} (c) and time average $[M_l]/10^{-2}$ m^{2}s^{-2} (red solid) (d) and the corresponding ellipse quantity θ_l (e) and time average $[\theta_l]$ (red solid) (f) over a $T = 20,000$ hrs equilibration period. The normalised zonal-time average zonal velocity $[\overline{u}]/U_{\max}$ is also plotted for comparison (black dotted) where $U_{\max}$ is the maximum value of $[\overline{u}]$.

time-mean over N_l does not average to reveal a correlation with the jet structure and so scales retained in the low-pass filter are not responsible for the time-mean structure in N. The zonal pulses observed in the Hovmöller plots of M are also present in M_l. We see in the time-mean of M_l that these scales provide the zonal structure witnessed in the time-mean of M presented in Fig. 5.5.1. As we have noted before, these pulses are not entirely consistent with the jet pattern, though they do broadly resemble some jet structure. They are however consistent with the alternating streaking pattern in N_l. The Hovmöller plot of θ_l, calculated from the low-pass filtered stress quantities N_l and M_l, demonstrates the same vague alternating north and south flux direction witnessed in θ with no discernable tilting pattern in the time-mean.

In Fig. 5.5.4 we examine the momentum flux quantities filtered at high-pass where wavenumbers $k \geq k_c = k_\beta$ are retained. The Hovmoller plot of N_h reveals an alternating band structure that does not vary in time save for some noise. The strength of these bands are smaller than the magnitude of the streaks in N_l which is why they are not apparent in the unfiltered signal N. From the the time-average plot we can see these bands provide the zonal structure observed in the time-mean of N. This zonal structure is consistent with the zonal jets.

The Hovmöller plot of M_h demonstrates small, negative, persistent band structures that align with the jet structure. The sign of M_h is negative everywhere inside the domain and is only positive at the domain walls. M_h has its highest amplitude, and is most negative within the jet cores. The pattern in the time-mean correlates with the jet structure—though the jet structure is purely zonal—and the eddies at the scales supporting the jet have strong meridional velocities.

The high-pass tilt angle θ_h demonstrates a persistent banded pattern consistent with the jet in its Hovmöller plot. The pattern in the time-mean is consistent with the jet structure and also reveals some more subtle features. A sharp eastward jet requires a sharp change in tilt angle going from strongly negative on its northern flank to positive to its south across the jet maximum. A broad westward jet requires a softer change in the tilt angle gradually changing from positive to negative from the north to the south. This results in the sawtooth shape observed in the time-mean structure of the tilt-angle.

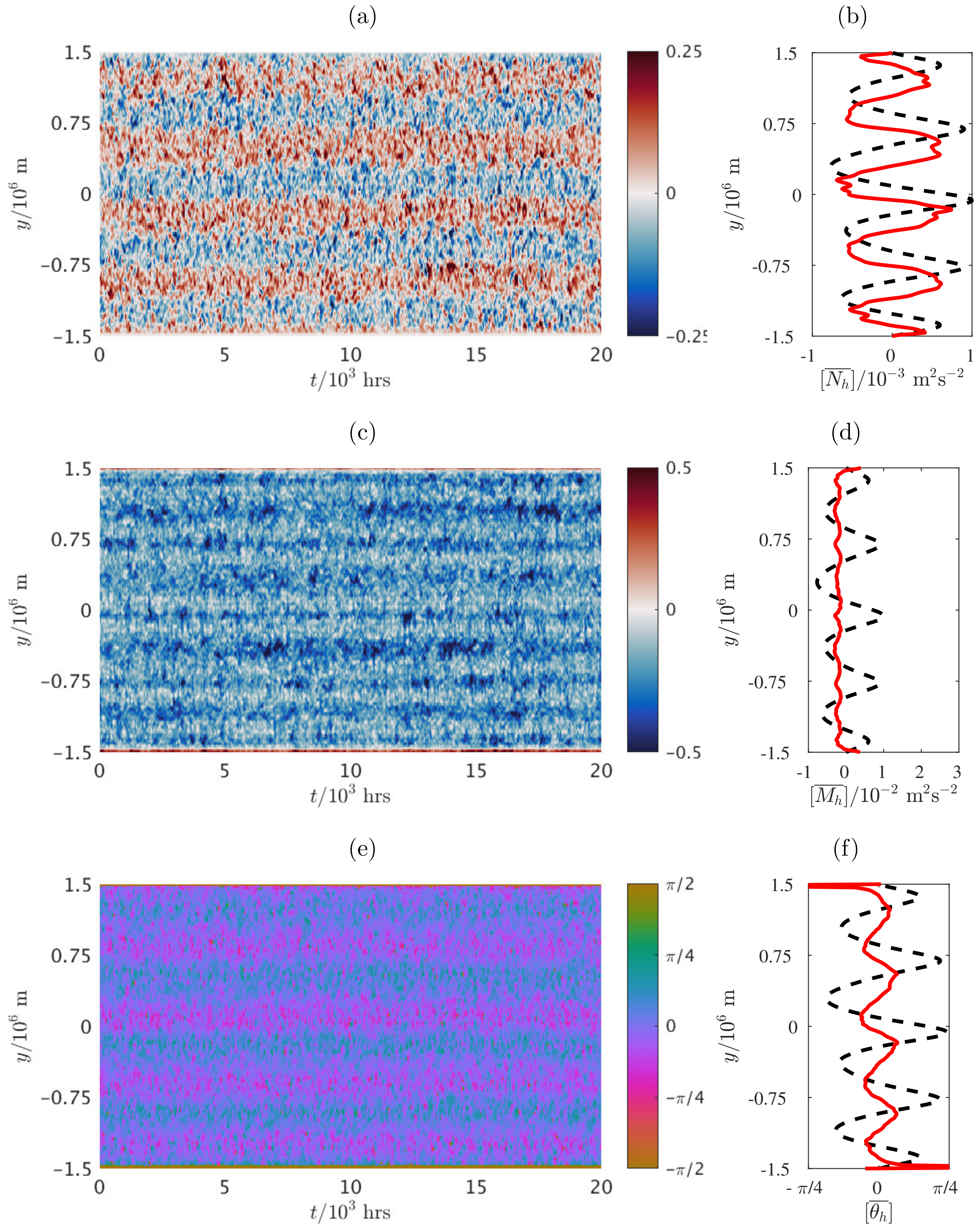

Figure 5.5.4: Hovmöller plots of the intermediate-scale shear stress $N_h/10^{-2}$ m^{2}s^{-2} (a) and time average $[\overline{N_h}]/10^{-3}$ m^{2}s^{-2} (red solid) (b), normal stress difference $M_h/10^2$ m^{2}s^{-2} (c) and time average $[\overline{M_h}]/10^{-2}$ m^{2}s^{-2} (red solid) (d) and the corresponding ellipse quantity θ_h (e) and time average $[\overline{\theta_h}]$ (red solid) (f) over a $T = 20,000$ hrs equilibration period. The normalised zonal-time average zonal velocity $[\overline{u}]/U_{\max}$ is also plotted for comparison (black dotted) where $U_{\max}$ is the maximum value of $[\overline{u}]$.

5.6 Discussion

Knowing the energy injection rate ϵ *a priori* has allowed us to predict, with some success, the characteristic scales associated with 2D turbulence and anisotropic β-plane turbulence. Though we have noted that the effective energy injection rate ϵ_{eff} which transfers along the inertial ranges, differs in an unpredictable way due to the inclusion of the biharmonic dissipation, so these will not be exact. Nevertheless, we have been able to characterise flows according to these scales. The two scales of importance in jet formation are k_β, the anisotropic wavenumber and the Rhines scale given by Eq. (1.2.31).

We have calculated k_β^p for each run in Table 5.4. Though this is likely to be underestimated, we have found for intermediate β (runs B_0, B_1, C_0 and C_1) this lies in the transition region between isotropic and anisotropic dynamics. Firstly, in both continuously forced and forced damped runs, k_β^p resides at the vicinity where the 1D spectra and its energy front k_{min}, steepen towards the Rhines spectrum. Secondly, the temporal evolution of the energy front for run $\beta = 0$ has been shown to follow the fast $t^{-3/2}$ scaling law in Eq. (5.3.8). When we introduced β, the evolution of the energy front bends towards the comparatively slow $t^{-1/4}$ scaling law in Eq. (5.3.11). Sukoriansky et al. (2007) state that the transition in the time evolution between the two regimes is difficult to characterise. Here find that though there is no sharp transition between the two regimes, there is a clear transition between the two and that the position of k_β^p maybe found in this region.

We have paid a lot of attention to the 1D spectra in Eq. (5.4.4) as they provide us more insight than looking at the distribution of energy in wavenumber space $E\left(k_x, k_y\right)$, where it is difficult to determine positions of characteristic scales. This is complicated further by the fact that our flows are meridionally inhomogeneous and require us to consider our energy spectra as functions meridional position. In the next chapter we will explore the anisotropy and inhomogeniety in the 2D spectra in more detail.

What has been overlooked in studies such as Chekhlov et al. (1996) and Sukoriansky et al. (2007), is the role of ϕ_Z that determines how the zonal energy is spread about the k_y-axis. We have seen that this angle needs to made smaller as β-increases. In the prior studies, this has perhaps not been necessary as runs which fall squarely in the zonostrophic regime in which scales respect the chain inequality given by Eq. (5.4.6), will usually have small ϕ_Z. Though its role will not be pursued further in the present work, this may be a useful avenue for future exploration.

Following analysis from Sukoriansky et al. (2007), we have understood the Rhines scale given by Eq. (1.2.31) as the position of the energy front k_{min} along the Rhines spectrum and have emphasised that there is nothing stopping the flow from reaching the lowest mode. However, we have no runs in which the flow has managed to attain the largest available scale when $\beta \neq 0$. The behaviour of the Rhines scale's evolution in time is given by Eq. (5.3.11) which slows down significantly as $k_{\min} \to 0$, this effect is greater when β is larger. For runs B_0, C_0 and D_0 jets approached a quasi-stationary configuration of $k_{\text{jet}} = 5$, $k_{\text{jet}} = 9$ and $k_{\text{jet}} = 19$ respectively, which evolves very slowly over a $50,000$ hr period, apart from some westward jet broadening or eastward jet sharpening events. For the time-scales of significance for mesoscale oceanic processes, from a few weeks $T \sim 500$ hrs to a few months $T \sim 3000$ hrs this quasi-stationary state does not evolve at all and so for all intents and purposes the cascade may be considered arrested.

The apex of this chapter has been to learn more about the role of anisotropisation process in eddy-mean flow interactions of steady state jets. We have confirmed the balance between the shear stress divergence and Rayleigh friction in Eq. (5.3.19) and we have explored this relationship in more detail using the tools developed in §4. On closer examination and with the aide of a zonal filter, we have found rather counter-intuitively that eddies in the vicinity of the zonal spectrum, where $k_x < k_\beta$, do not support the jet structure. Rather, eddies in which $k_x > k_\beta$ are responsible for the maintaining the jet. Following a stationary-transient decomposition developed by McWilliams (1984), in which the flow was separated into coherent structures and transient eddies, Huang and Robinson (1998) came to a similar conclusion by examining the spectral energy fluxes. Here we have been able to visualise these interactions using the contemporary geometric eddy ellipse framework.

Whilst our zonal filter has provided us with some insight, it would be useful to understand how meridional scales contribute to this picture and how anisotropy develops as a function of radial wavenumber k. We will develop the tools to do this in the next chapter.

5.7 Conclusion

In this chapter we have analysed data from eight runs of varying β, four of which have been continuously forced and four of which have equilibrated under the inclusion of linear drag.

We began by examining the signatures in physical space of an inverse energy cascade. We understood the evolution of the flow, the emerging coherent structures and their equilibrium configurations, in terms of the position of energy front $k_{\min}$. We found that $k_{\min}$ may be equal to the Kolmogorov wavenumber k_{KBK} or the Rhines scale k_{R}, depending on the β-plane strength. Each of these are associated with isotropic and anisotropic dynamics respectively. We have also examined the zonal-time average equilibrium jet profiles and found their profiles to satisfy the barotropic stability criteria.

We predicted the anisotropy wavenumber k_β^p for each run, which marks the position where the Rhines spectrum steepens beyond the Kolmogorov spectrum and found these to roughly agree with observations for $\beta = \beta_0$ and $\beta = 4\beta_0$. There was less agreement for run $\beta = 16\beta_0$ between the predicted anisotropy wavenumber and the observed, due to the effect of the scale-selection biharmonic that is more pronounced when β is stronger. We also found that the Rhines spectrum takes significantly longer periods of time than the Kolmogorov spectrum to develop, with the Rhines scale following a $t^{-1/4}$ dependence when compared to the Kolmogorov wavenumber which follows a $t^{-3/2}$ scaling law.

The inclusion of linear drag leads to flows equilibrating and $k_{\min}$ halting its propagation in wavenumber space at equilibrium wavenumber k_{eq}. This we have predicted using Eq. (5.3.15) and have calculated directly from the equilibration energy. We find that though k_{eq}^p does not agree exactly, it falls in the vicinity of the observed values of k_{eq} and the final destination of the energy front $k_{\min}$.

We found that the eddy-mean flow relationship Eq. (5.3.19) holds after a long time average, suggesting that there are significant time-dependent processes dominating the eddy-mean flow interactions at short timescales. This masks an underlying pattern of momentum fluxes that support the jet structures. We examined Hovmöller plots of the shear stress N and the normal stress difference M and calculated the tilt angles θ of geometric eddy ellipses associated with this flow. We found that large amplitude, short timescale momentum fluxes dominated the zonal scales in the vicinity of the Rhines spectrum, where $k < k_\beta$. We found that the intermediate scales eddies where $k < k_\beta$, in contrast, contained a low-amplitude, persistent momentum flux pattern that correlated with the jet structure.

6

Anisotropy and Inhomogeneity

6.1 Introduction

In §5 we described jet formation in geostrophic turbulence as a consequence of an anisotropisation process in the 2D energy spectrum. We saw that jet formation coincides with the appearance of a dumbbell structure in $E(k_x, k_y)$ (Vallis and Maltrud, 1993) and a build up of energy around the k_y-axis which contains most of the energy in the system. In this section we will investigate this anisotropy in the energy spectrum in more detail.

Anisotropisation of 2D energy spectra had been a separate subject of investigation dating as far back as the work of Herring (1975) where the 2D energy spectra of systems, forced anisotropically, were decomposed into an angular Fourier series. This decomposition was later used by Basdevant et al. (1981) for some elementary investigations of anisotropy in the energy spectra of two dimensional flows under β-plane turbulence. However, their analysis did not consider that the jets that form in geostrophic turbulence are also meridionally inhomogeneous.

In §4 we derived the eddy stress tensor given by Eq. (4.3.5). This tensor is based on single point statistics, where we only considered correlations between velocity components at the same spatial and temporal location. In §5 we were able to filter the eddy velocities zonally to obtain their contributions to the single point quantities N and M. We used the fact that in zonally homogeneous systems, the only velocity correlations that contribute to the single point quantities are those where

$$\left\langle \widetilde{u}_i(k_x^{(1)}, y)\widetilde{u}_j(k_x^{(2)}, y) \right\rangle \propto \delta(k_x^{(1)} + k_x^{(2)}), \tag{6.1.1}$$

i.e. where $k_x^{(1)} = -k_x^{(2)}$. Here, $\widetilde{u}_i(k_x^{(1)}, y)$ is the i^{th} component of the zonal Fourier transform of the velocity with zonal wavenumber $k_x^{(1)}$. However, the flow is inhomogeneous in y and we will need to consider the two point correlations associated with the energy spectra in order to relate this to the y-dependent components of the tensor given in Eq. (4.3.5). The reason single point statistics are not sufficient to relate results is that the 2D energy spectrum $E(k_x, k_y)$ we have analysed is a quantity that has been integrated over the direction of inhomogeneity. Therefore it does not contain the two-point correlations that are needed to make the connection between the different diagnostics we analysed in the previous chapter. In this chapter, we will derive the inhomogeneous analogue of the energy spectrum to bridge this gap and better understand the role of anisotropy in jet formation.

6.2 The Inhomogeneous Spectrum Tensor

In this section, we will generalise the results from homogeneous incompressible two-dimensional turbulence presented in Batchelor (1953) to account for general inhomogeneity. To calculate the spectrum, formally we must consider correlations between velocity components at two separate spatial and temporal locations. The wavevector $\mathbf{k} = (k_x, k_y)$ we have been using is then the reciprocal of the separation vector $\mathbf{r} = \mathbf{x}^{(1)} - \mathbf{x}^{(2)}$ between two locations $\mathbf{x}^{(1)}$ and $\mathbf{x}^{(2)}$ at which we evaluate our velocity components. Consider an ensemble of incompressible velocity fields $u_i(\mathbf{x}, t)$, where i labels the velocity component. If we consider a fluid to be homogeneous, its statistics depend only on the separation vector $\mathbf{r}$ such that the two-point velocity correlation tensor will be given by

$$\begin{aligned} Q_{ij}(\mathbf{x}^{(1)}, \mathbf{x}^{(2)}, t^{(1)}, t^{(2)}) &= \left\langle u_i(\mathbf{x}^{(1)}, t^{(1)}) u_j(\mathbf{x}^{(2)}, t^{(2)}) \right\rangle \\ &= \left\langle u_i(\mathbf{x}^{(1)}, t^{(1)}) u_j(\mathbf{x}^{(1)} + \mathbf{r}, t^{(2)}) \right\rangle \\ &= Q_{ij}(\mathbf{r}, t^{(1)}, t^{(2)}), \end{aligned} \tag{6.2.1}$$

and we can assume that the ensemble average is equal to the spatial average

$$\begin{aligned} Q_{ij}(\mathbf{r}, t^{(1)}, t^{(2)}) &= \left\langle u_i(\mathbf{x}^{(1)}, t^{(1)}) u_j(\mathbf{x}^{(1)} + \mathbf{r}, t^{(2)}) \right\rangle \\ &\equiv \int_\Omega u_i(\mathbf{x}^{(1)}, t^{(1)}) u_j(\mathbf{x}^{(1)} + \mathbf{r}, t^{(2)}) d^2\mathbf{x}^{(1)}. \end{aligned} \tag{6.2.2}$$

For $t^{(1)} = t^{(2)}$, this provides the premise upon which the widely used 2D energy spectrum is calculated which does not apply to our meridionally inhomogeneous system. The statistics of general inhomogeneous systems depend on $\mathbf{r}$ but also depend on the centre coordinate between two points $\mathbf{x}_c = (\mathbf{x}^{(1)} + \mathbf{x}^{(2)})/2$. The two-point velocity correlation tensor then has the dependence

$$\begin{aligned} Q_{ij}(\mathbf{x}^{(1)}, \mathbf{x}^{(2)}, t^{(1)}, t^{(2)}) &= \left\langle u_i(\mathbf{x}^{(1)}, t^{(1)}) u_j(\mathbf{x}^{(2)}, t^{(2)}) \right\rangle \\ &= \left\langle u_i(\mathbf{x}_c - \frac{\mathbf{r}}{2}, t^{(1)}) u_j(\mathbf{x}_c + \frac{\mathbf{r}}{2}, t^{(2)}) \right\rangle \\ &= Q_{ij}(\mathbf{x}_c, \mathbf{r}, t^{(1)}, t^{(2)}). \end{aligned} \tag{6.2.3}$$

We will now assume that the flow is stationary in time and drop the time dependence of the tensor. The incompressibility condition Eq. (2.2.2b) gives

$$\frac{\partial Q_{ij}}{\partial r_i} = \frac{\partial Q_{ij}}{\partial r_j} = 0, \tag{6.2.4}$$

for a given $\mathbf{x}_c$ where we have used summation convention. As with homogeneous flows, where it can be shown that $Q_{ij}(\mathbf{r}) = Q_{ji}(-\mathbf{r})$, inhomogeneous flows possess the symmetry

$$\begin{aligned} Q_{ij}(\mathbf{x}_c, \mathbf{r}) &= \left\langle u_i\left(\mathbf{x}_c - \frac{\mathbf{r}}{2}\right) u_j\left(\mathbf{x}_c + \frac{\mathbf{r}}{2}\right)\right\rangle \\ &= \left\langle u_j\left(\mathbf{x}_c + \frac{\mathbf{r}}{2}\right) u_i\left(\mathbf{x}_c - \frac{\mathbf{r}}{2}\right)\right\rangle \\ &= Q_{ji}(\mathbf{x}_c, -\mathbf{r}). \end{aligned} \tag{6.2.5}$$

Single point statistics are recovered by setting $\mathbf{r} = \mathbf{0}$. The components of the single point velocity correlation tensor are given by

$$T(\mathbf{x}_c) = Q_{ij}(\mathbf{x}_c, \mathbf{0}) = \langle u_i(\mathbf{x}_c), u_j(\mathbf{x}_c)\rangle. \tag{6.2.6}$$

We note that the system we are interested in is zonally homogeneous so $\mathbf{x}_c = y_c\hat{\mathbf{j}}$ and we can assume the zonal average is equivalent to the ensemble average. Substituting the eddy velocities $u_i' = u_i - \overline{u}$ in Eq. (6.2.3), we obtain the appropriate two-point eddy velocity correlation tensor for this system:

$$Q_{ij}'(y_c, \mathbf{r}) = \overline{u_i'\left(y_c\hat{\mathbf{j}} - \frac{\mathbf{r}}{2}\right) u_j'\left(y_c\hat{\mathbf{j}} + \frac{\mathbf{r}}{2}\right)}. \tag{6.2.7}$$

We can then recover the components of Eq. (4.3.2) by setting $\mathbf{r} = \mathbf{0}$:

$$T_{ij}(y_c) = Q_{ij}'(y_c, \mathbf{0}) = \overline{u_i'(y_c)\, u_j'(y_c)}. \tag{6.2.8}$$

We now introduce the inhomogeneous spectrum tensor $\Phi_{ij}(\mathbf{x}_c, \mathbf{k})$ given by the transforms

$$\Phi_{ij}(\mathbf{x}_c, \mathbf{k}) = \frac{1}{\sqrt{L_x L_y}} \int \exp(-i\mathbf{k}\cdot\mathbf{r})\, Q_{ij}(\mathbf{x}_c, \mathbf{r})\, d^2\mathbf{r}, \tag{6.2.9}$$

$$Q_{ij}(\mathbf{x}_c, \mathbf{r}) = \frac{1}{\sqrt{L_x L_y}} \int \exp(i\mathbf{k}\cdot\mathbf{r})\, \Phi_{ij}(\mathbf{x}_c, \mathbf{k})\, d^2\mathbf{k}. \tag{6.2.10}$$

For simplicity we have assumed that our domain is doubly periodic. Using the incompressibility condition Eq. (6.2.4) we find that

$$k_j \Phi_{ij}(\mathbf{x}_c, \mathbf{k}) = k_i \Phi_{ij}(\mathbf{x}_c, \mathbf{k}) = 0. \tag{6.2.11}$$

The spectrum tensor given by Eq. (6.2.9) also has the symmetries

$$\Phi_{ij}(\mathbf{x}_c, \mathbf{k}) = \Phi_{ji}(\mathbf{x}_c, -\mathbf{k}) = \Phi^*_{ji}(\mathbf{x}_c, \mathbf{k}), \tag{6.2.12}$$

where we have used Eq. (6.2.5) and the last relation arises because Q_{ij} is real. Integrating Φ_{ij} over $\mathbf{k}$ is equivalent to setting $\mathbf{r} = \mathbf{0}$ in Q_{ij}, so we may write the eddy velocity correlation tensor given by Eq. (6.2.8) as

$$T_{ij}(y_c) = Q'_{ij}(y_c, \mathbf{0}) = \frac{1}{\sqrt{L_x L_y}} \int \Phi'_{ij}(y_c, \mathbf{k})\, \mathrm{d}^2\mathbf{k}. \tag{6.2.13}$$

6.2.1 Structure of the Spectrum Tensor

The argument presented in Batchelor (1953) for deriving the general form of a homogeneous spectrum tensor assumed continuity and geometric considerations. Here we will follow a similar argument to derive the general form of Eq. (6.2.9) holding $\mathbf{x}_c$ fixed. Firstly we note that since Φ_{ij} is Hermitian, it can be diagonalised. Consider an arbitrary vector $\mathbf{X}$. Its dot product with the two orthogonal eigenvectors $\mathbf{a}$ and $\mathbf{b}$ of Φ_{ij} is given by

$$Y_1 = a_i X_i, \tag{6.2.14a}$$

$$Y_2 = b_i X_i. \tag{6.2.14b}$$

Then the scalar field

$$\Phi(\mathbf{x}_c, \mathbf{k}) = X_i X^*_j \Phi_{ij}(\mathbf{x}_c, \mathbf{k}) = s_1 Y_1 Y^*_1 + s_2 Y_2 Y^*_2 \geq 0, \tag{6.2.15}$$

is of non-negative quadratic form and has been reduced to its diagonal form. Here the scalar fields $s_1(\mathbf{x}_c, \mathbf{k})$ and $s_2(\mathbf{x}_c, \mathbf{k})$ are the real non-negative eigenvalues of Φ_{ij}. If we choose $\mathbf{X}$ to lie parallel to $\mathbf{k}$ then by the incompressibility condition given by Eq. (6.2.11), Eq. (6.2.15) becomes

$$\Phi(\mathbf{x}_c, \mathbf{k}) = X_i X^*_j \Phi_{ij}(\mathbf{x}_c, \mathbf{k}) \propto k_i k_j \Phi_{ij}(\mathbf{x}_c, \mathbf{k}) = 0. \tag{6.2.16}$$

In general, at least one of Eq. (6.2.14a) and Eq. (6.2.14b) must be non-zero. If (say) $Y_1 = 0$ then $Y_2 \neq 0$ and $s_2 = 0$ and Eq. (6.2.15) becomes

$$\Phi(\mathbf{x}_c, \mathbf{k}) = X_i X_j \Phi_{ij}(\mathbf{x}_c, \mathbf{k}) = s_1 Y_1 Y^*_1 = s_1 X_i X^*_j \left(a_i a^*_j\right) = 0, \tag{6.2.17}$$

and so the most general form of the inhomogeneous spectrum tensor is given by

$$\Phi_{ij}(\mathbf{x}_c, \mathbf{k}) = s_1 a_i a^*_j. \tag{6.2.18}$$

We can rewrite Eq. (6.2.18) in a more useful form by observing that since $\mathbf{a}$ and $\mathbf{X}$ are orthogonal then $\mathbf{a}$ must also be orthogonal to $\mathbf{k}$ and the following identity holds

$$\delta_{ij} = \frac{a_i a_j^*}{|\mathbf{a}|^2} + \frac{k_i k_j^*}{|\mathbf{k}|^2}. \tag{6.2.19}$$

Substituting this into Eq. (6.2.18), we find the spectrum tensor has the general form

$$\Phi_{ij}\left(\mathbf{x},\mathbf{k}\right) = f\left(\mathbf{x}_c,\mathbf{k}\right)\left(\delta_{ij} - \frac{k_i k_j}{k^2}\right), \tag{6.2.20}$$

where we have relabelled $s_1|\mathbf{a}|^2 = f\left(\mathbf{x}_c,\mathbf{k}\right)$ and $k = |\mathbf{k}|$. We ensure that the symmetry properties given by Eq. (6.2.12) are obeyed. Firstly

$$\Phi_{ji}\left(\mathbf{x}_c,-\mathbf{k}\right) = f\left(\mathbf{x}_c,-\mathbf{k}\right)\left(\delta_{ji} - \frac{k_j k_i}{k^2}\right) = \Phi_{ij}\left(\mathbf{x}_c,\mathbf{k}\right) \tag{6.2.21}$$

holds because

$$f\left(\mathbf{x}_c,-\mathbf{k}\right) = f\left(\mathbf{x}_c,\mathbf{k}\right). \tag{6.2.22}$$

Also

$$\begin{aligned}\Phi_{ji}^*\left(\mathbf{x}_c,\mathbf{k}\right) &= f^*\left(\mathbf{x}_c,\mathbf{k}\right)\left(\delta_{ji} - \frac{k_j k_i}{k^2}\right)\\ &= f\left(\mathbf{x}_c,\mathbf{k}\right)\left(\delta_{ij} - \frac{k_i k_j}{k^2}\right)\\ &= \Phi_{ij}\left(\mathbf{x}_c,\mathbf{k}\right),\end{aligned} \tag{6.2.23}$$

because $f\left(\mathbf{x}_c,\mathbf{k}\right)$ must be real. We observe that the trace of Φ_{ij} is related to the energy spectrum by

$$E\left(\mathbf{x}_c,\mathbf{k}\right) = \frac{1}{2}\Phi_{ii}\left(\mathbf{x}_c,\mathbf{k}\right) = \frac{1}{2}f\left(\mathbf{x}_c,\mathbf{k}\right). \tag{6.2.24}$$

So the scalar function $f\left(\mathbf{x}_c,\mathbf{k}\right)$ is simply half the inhomogenous energy spectrum and we therefore substitute Eq. (6.2.24) into Eq. (6.3.5) to obtain

$$\Phi_{ij}\left(\mathbf{x},\mathbf{k}\right) = 2E\left(\mathbf{x}_c,\mathbf{k}\right)\left(\delta_{ij} - \frac{k_i k_j}{k^2}\right). \tag{6.2.25}$$

From this, we may recover the 2D eddy energy spectrum $E'\left(\mathbf{k}\right) = E'\left(k_x,k_y\right)$ by integrating Eq. (6.2.24) over $\mathbf{x}_c$:

$$E'\left(\mathbf{k}\right) = \int_\Omega E'\left(\mathbf{x}_c,\mathbf{k}\right) d^2\mathbf{x}_c. \tag{6.2.26}$$

6.3 Anisotropy

In this section we will consider the anisotropy of the spectrum tensor given by Eq. (6.2.25). We do this by expanding the energy spectrum $E(\mathbf{x}_c, \mathbf{k})$ using the angular decomposition presented in Herring (1975):

$$E(\mathbf{x}_c, k, \phi) = \sum_{n=-\infty}^{\infty} \exp(in\phi) f_n(\mathbf{x}_c, k) \tag{6.3.1}$$

where the anisotropy coefficients f_n are functions of $\mathbf{x}_c$ and $k = |\mathbf{k}|$, and ϕ is the angle $\mathbf{k}$ makes with respect to the direction of anisotropy, which in our case is the k_y-axis. The expansion given by Eq. (6.3.1) should obey the symmetry properties in Eq. (6.2.12). We require that Eq. (6.2.22) is obeyed, this gives

$$\sum_{n=-\infty}^{\infty} f_n \exp(in\phi) = \sum_{n=-\infty}^{\infty} f_n \exp(in(\phi+\pi)), \tag{6.3.2}$$

which only holds if $\exp(in\pi) = 1$ and so n must be even. Since $E(\mathbf{x}_c, \mathbf{k})$ is real

$$\begin{aligned} \sum_{n=-\infty}^{\infty} f_n \exp(in\phi) &= \sum_{n=-\infty}^{\infty} f_n^* \exp(-in\phi) \\ \sum_{n=\infty}^{-\infty} f_{-n} \exp(-in\phi) &= \sum_{n=-\infty}^{\infty} f_n^* \exp(-in\phi), \end{aligned} \tag{6.3.3}$$

which holds if

$$f_{-n}(\mathbf{x}, k) = f_n^*(\mathbf{x}, k). \tag{6.3.4}$$

Substituting the expansion given by Eq. (6.3.1) into Eq. (6.2.25), we obtain the inhomogenous spectrum tensor in terms of an angular decomposition

$$\Phi_{ij}(\mathbf{x}_c, k, \phi) = 2\left(\delta_{ij} - \frac{k_i k_j}{k^2}\right) \sum_{n=-\infty}^{\infty} f_n(\mathbf{x}_c, k) \exp(in\phi). \tag{6.3.5}$$

Now we can recover the single point information in the eddy velocity correlation tensor given by Eq. (6.2.8) by using Eq. (6.2.13) and integrating Eq. (6.3.5) over k and ϕ. The result is equivalent to setting $\mathbf{r} = \mathbf{0}$ and we find:

$$Q_{ij}(\mathbf{x}_c, \mathbf{0}) = 2\int_0^{\infty}\int_0^{2\pi} \sum_{n=-\infty}^{\infty} \exp(in\phi) f_n(\mathbf{x}_c, k) \left(\delta_{ij} - \frac{k_i k_j}{k^2}\right) k dk d\phi. \tag{6.3.6}$$

Using $k_1 = k_x = -k\sin\phi$ and $k_2 = k_y = k\cos\phi$ we find that the first diagonal element in Eq. (6.2.8) is given by

$$Q_{11}\left(\mathbf{x}_c, \mathbf{0}\right) = 2\pi \int_0^\infty \mathrm{d}k k f_0 + \pi \int_0^\infty \mathrm{d}k k \left(f_2 + f_2^*\right), \tag{6.3.7}$$

and the second is given by

$$Q_{22}\left(\mathbf{x}_c, \mathbf{0}\right) = 2\pi \int_0^\infty \mathrm{d}k k f_0 - \pi \int_0^\infty \mathrm{d}k k \left(f_2 + f_2^*\right), \tag{6.3.8}$$

where we have used Eq. (6.3.4). We find that only angular modes $n = 0$ and $n = 2$ give non-zero contributions to the diagonal elements of the single point correlator. The off-diagonal elements of Eq. (6.2.8) are given by

$$Q_{12}\left(\mathbf{x}_c, \mathbf{0}\right) = Q_{21}\left(\mathbf{x}, \mathbf{0}\right) = -i\pi \int_0^\infty \mathrm{d}k k \left(f_2 - f_2^*\right), \tag{6.3.9}$$

where only the $n = 2$ angular mode gives a non-zero contribution. If we write

$$E_n \equiv 2\pi \int_0^\infty dk k f_n, \tag{6.3.10}$$

we can decompose Q_{ij} into its isotropic and anisotropic components:

$$Q\left(\mathbf{x}_c, \mathbf{0}\right) = E_0 I + \begin{pmatrix} \frac{E_2+E_2^*}{2} & -i\frac{E_2-E_2^*}{2} \\ -i\frac{E_2-E_2^*}{2} & -\frac{E_2+E_2^*}{2} \end{pmatrix}. \tag{6.3.11}$$

Now if we set $Q_{ij} = Q'_{ij}$ given by Eq. (6.2.8), then the decomposition given by Eq. (6.3.11) is equivalent to Eq. (4.3.3). Here the single point correlators Eq. (4.3.4), Eq. (4.3.6) and Eq. (4.3.7) have the representations

$$K\left(y_c\right) = E_0 = 2\pi \int_0^\infty dk k f_0, \tag{6.3.12a}$$

$$M\left(y_c\right) = \frac{E_2 + E_2^*}{2} = 2\pi \int_0^\infty dk k \mathrm{Re}\left(f_2\right), \tag{6.3.12b}$$

$$N\left(y_c\right) = -i\frac{E_2 - E_2^*}{2} = 2\pi \int_0^\infty dk k \mathrm{Im}\left(f_2^*\right). \tag{6.3.12c}$$

We now have decomposed the single point statistics given by Eq. (6.3.13) in terms of contributions from eddy velocities at different radial scales k. These are given by

$$K\left(k, y_c\right) = 2\pi k f_0 \tag{6.3.13a}$$

$$M\left(k, y_c\right) = 2\pi k \mathrm{Re}\left(f_2\right), \tag{6.3.13b}$$

$$N\left(k, y_c\right) = 2\pi k \mathrm{Im}\left(f_2\right), \tag{6.3.13c}$$

From this, we may obtain the eddy tilt angle at different radial scales as

$$\theta(k, y_c) = \frac{1}{2}\arctan\left(\frac{\mathrm{Im}(f_2)}{\mathrm{Re}(f_2)}\right). \tag{6.3.14}$$

Our analysis has revealed that we must consider both anisotropy and inhomogeneity in order to relate the energy spectrum to the eddy stress parameters. The inhomogeneous energy spectrum $E(y_c, k_y, k_y)$ is comprised of a superposition of all even anisotropic modes given by the expansion Eq. (6.3.1). However, the only modes contributing to the single-point statistics are $n = 0, \pm 2$.

From Eq. (6.3.13a) we see that the isotropic mode f_0 suffices to describes all the eddy velocity correlations as a function of radial scales k that contribute to the energy density. If we integrate Eq. (6.3.13a) over the direction of inhomogeneity y_c we find that the total eddy energy of the system is given by

$$E_m' = \int_{-\frac{L_y}{2}}^{\frac{L_y}{2}} \int_0^{\infty} K(k, y_c)\, dk\, dy_c. \tag{6.3.15}$$

Note that $E_m' \neq E_m$ because it does not contain the energy from the zonal mean flow. If we integrate Eq. (6.3.13a) over y_c we obtain the 1D energy spectrum of the eddy energy

$$K^0(k) \equiv E'(k) = \int_{-\frac{L_y}{2}}^{\frac{L_y}{2}} 2\pi k f_0\, dy. \tag{6.3.16}$$

The mode f_2 and its complex conjugate provide a complete description of the components of the eddy stress tensor given by Eq. (4.3.5). This is calculated as

$$f_2 = \int_0^{2\pi} E(y_c, k, \phi)(\cos 2\phi + i \sin 2\phi)\, d\phi. \tag{6.3.17}$$

The real part of the f_2 component gives the normal stress difference. We see that this difference is weighted more towards the zonal and meridional axes. The shear stress is given by the imaginary part of f_2. From Eq. (6.3.17) we see that this is quantity is weighted towards the diagonals of the energy spectrum.

In §5 we were only able to filter modes in the direction of homogeneity. We have now developed a formulation with which we can consider more general contributions to eddy velocity correlations from different scales. In particular, we have shown that the imaginary part of the anisotropic mode f_2 is the only quantity required to describe the eddy-mean flow relationship given by Eq. (5.3.19).

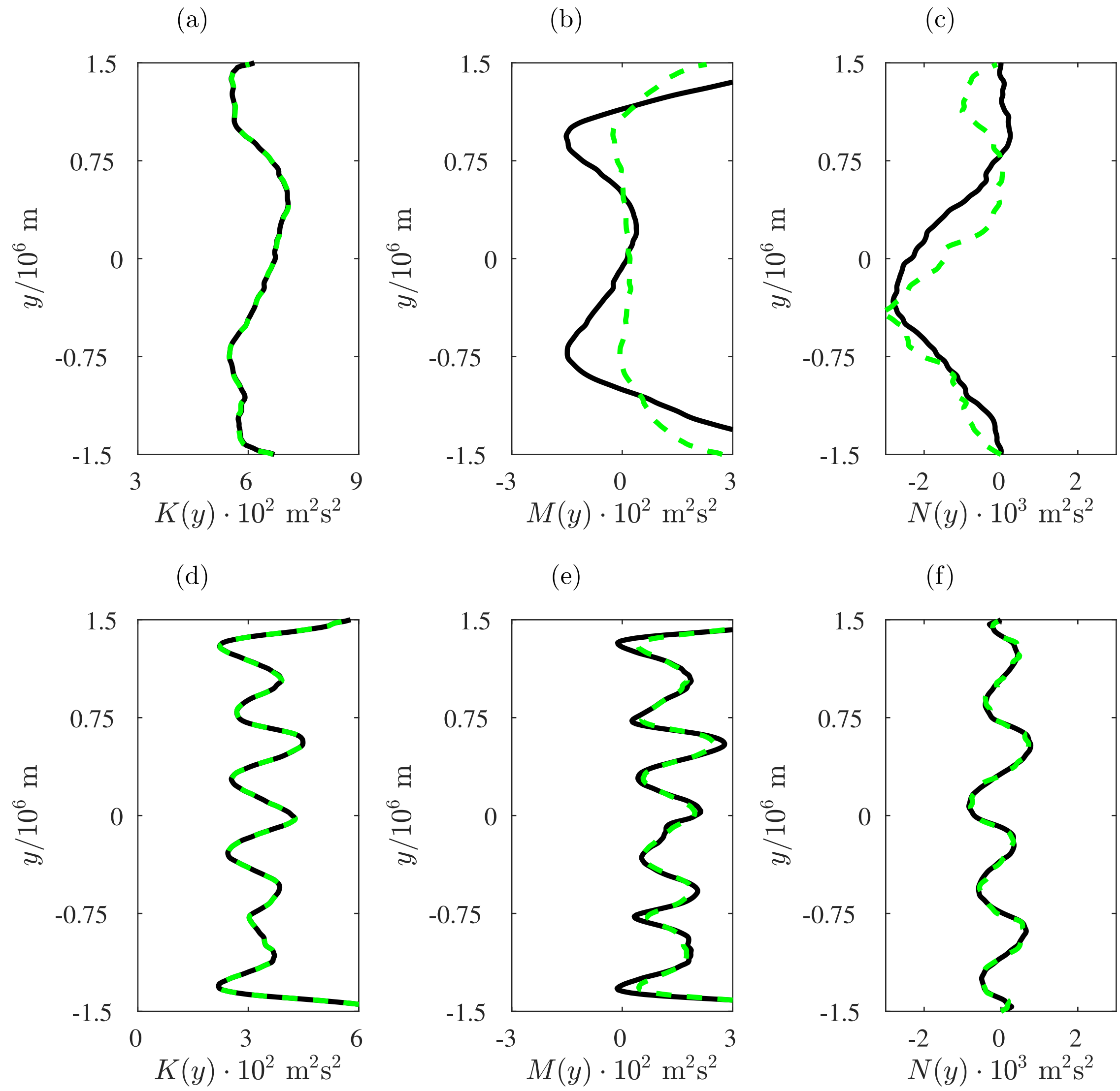

Figure 6.4.1: Zonal and time averaged eddy tensor components $K(y_c)$ (a) and (d), $M(y_c)$ (b) and (e) and $N(y_c)$ (c) and (f) for runs A_1 (top row) and C_1 (bottom row) respectively. This is calculated directly (black solid) and using Eq. (6.3.12a), Eq. (6.3.12b) and Eq. (6.3.12c) with the inhomogeneous energy spectrum $E(y_c, k_x, k_y)$.

6.4 Results and Discussion

We will now perform some basic diagnostics using this formulation with the equilibrated runs A_1 and C_1 (see Table 5.1) over a $t = 20,000$ hr equilibration period. In Fig. 6.4.1 we plot the components of the eddy velocity correlation tensor Eq. (4.3.3) calculated directly from the eddy velocity components u' and v' and using the angular decomposition given by Eq. (6.3.1) of the inhomogeneous energy spectrum. The eddy energy density $K(y_c)$ is recovered exactly for both A_1 and C_1. This is to be expected since the $K(y_c)$ given by Eq. (6.3.12a) is found from $E(y_c, k, \phi)$ by integrating in k and ϕ, over wavenumber space. The normal stress difference $M(y_c)$ does not agree exactly in either case and requires a long time-average to give the agreement shown. These should agree exactly suggesting that the low-wavenumbers are not correctly represented. This is also the reason that there is less agreement for run A_1 than for C_1, because modes in A_1 involve lower wavenumbers. The shear stress $N(y_c)$ only shows good agreement after a long time average. This demonstrates the worst agreement of the three eddy velocity correlation tensor variables because correlations in $N(y_c)$ turn out to be more sensitive to the details of the flow that are correspondingly less energetic.

We can recover the 1D and 2D spectra that we obtained in §5, by integrating over y_c. These are plotted in Fig. 6.4.2 for A_1 and C_1. In both cases, the 2D eddy energy spectrum $E'(k_x, k_y)$ is similar to the plots of $E(k_x, k_y)$ we examined in §5 in Fig. 5.4.6 except for the fact that here the $k_x = 0$ axis is not populated, as this axis corresponds to the zonal mean which we have subtracted. We also show plots of the 1D angularly averaged spectrum $E'(k)$ for the eddy energy. This is differs from the 1D spectra $E(k)$ we have plotted in 5.4.6 because the condensates along the k_y-axis have been removed through subtracting the zonal average. For run A_1 the eddy energy follows Kolmogorov scaling as expected. We also see that the eddy energy for run C_1 follows Kolmogorov scaling. However, there is still some contamination from the Rhines spectrum at the lowest wavenumbers in the spectra which can be seen as spikes. Note that taking the angular average of $E'(k_x, k_y)$ to obtain $E'(k)$ is equivalent to obtaining the zeroth mode in the angular decomposition so the two spectra we have plotted using these two methods are the same by construction.

In Fig. 6.4.3 we plot $K(k, y_c)$ given by Eq. (6.3.13a). As we have seen in Fig. 6.4.1, there is little variation in $K(k, y_c)$ over y_c for run A_1, this is reflected in its spectrum as it does not vary significantly as a function of y_c. This is not the case for run C_1 which does possess inhomogeneity in y_c. We see that in this case, low wavenumbers around k_{eq} provide the zonal pattern in $K(k, y_c)$. Also k_β does not mark a significant change in this spectrum which we have also noted for the y_c-integrated spectra in Fig. 6.4.2.

Here we have also included the positive and negative component of the spectrum $K(k, y_c)$ to illustrate issues with the implementation of this formulation. The inhomogenous spectrum tensor is derived based on the symmetry conditions given by Eq. (6.2.12). These require that $E(y_c, k, \phi)$ in Eq. (6.3.1) is real and positive and so then its angular average must also be real and positive. We see from Fig. 6.4.3 this is mostly an issue in low-wavenumbers which might suggest that symmetries imposed by the boundary conditions have not been properly considered. In Fig. 6.4.4 we plot $M(k, y_c)$ for runs A_1 and C_1. At high k both have comparable positive and negative components, indicating isotropic dynamics, except at the boundary where the positive component is

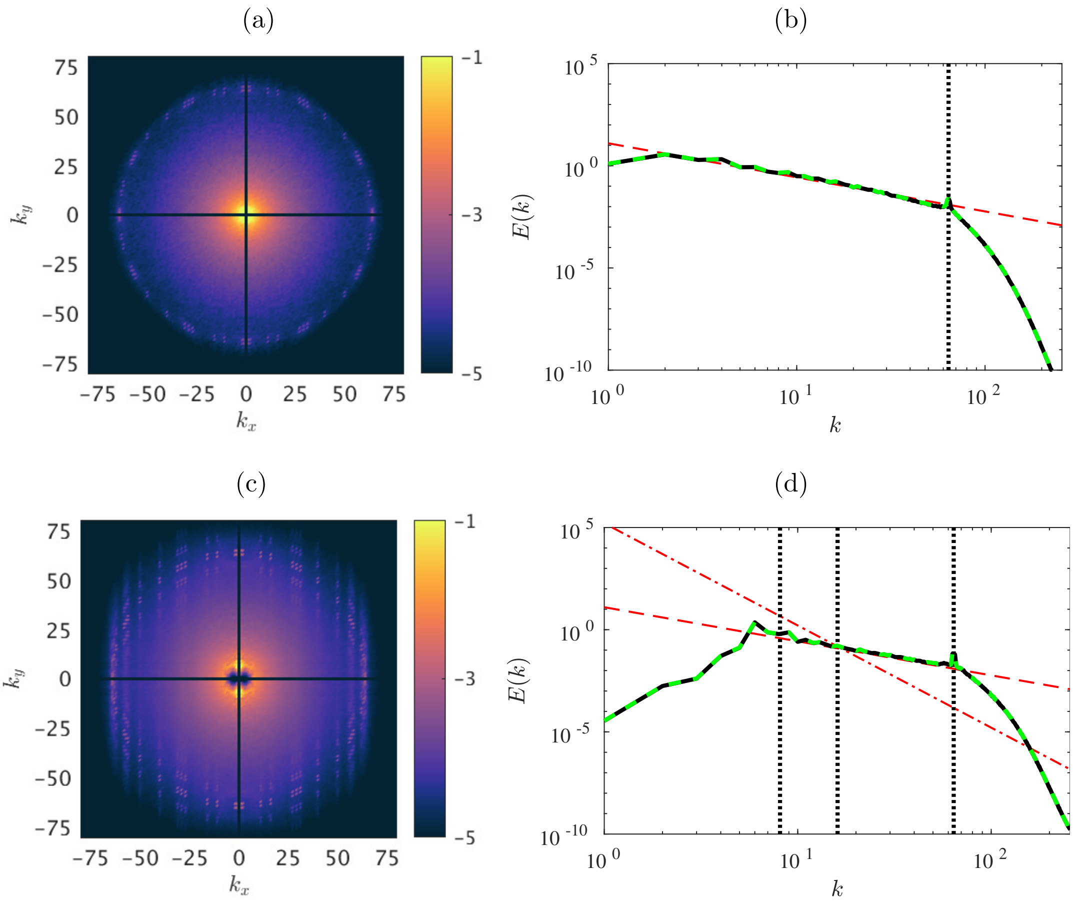

Figure 6.4.2: The 2D and 1D spectra that are typically calculated in homogeneous, isotropic turbulence are recovered using the inhomogeneous anisotropic decomposition. $E'(k_x, k_y)$ for run A_1 (a) and C_1 (c), are calculated using Eq. (6.2.26). $E'(k)$ for run A_1 (b) and run C_1 (d) is calculated as the angular average of $E'(k_x, k_y)$ (black solid) and using Eq. (6.3.16) (green dotted). The zonal (red dot-dash) and residual (red dash) spectra given by Eq. (5.4.4) are shown in the figure. For run A_1, the forcing scale is marked as a vertical black dotted line. For run C_1, from left to right the vertical black dotted lines are the characteristic scales k_{eq}, k_β and k_f.

larger for intermediate wavenumbers. For run C_1, the positive alternating pattern in $M(y_c)$ corresponds to a weakening and strengthening patterns in the positive component of $M(k, y_c)$ near scales k_{eq}. The imaginary component of f_2 in the expansion Eq. (6.3.1) provides the inhomogeneous spectrum of the shear stress given by Eq. (6.3.13c). Its absolute value, positive and negative components are plotted in Fig. 6.4.5. For run A_1, there are no distinguishing features in these smaller and intermediate scales. Only at the largest scales is there a strong northward flux of momentum interleaved with some weaker southward momentum fluxes that are a consequence of the flow not being fully equilibrated.

For run C_1, we have seen in §5.5 that zonal scales in which $k_\beta < k_x < k_f$ contain

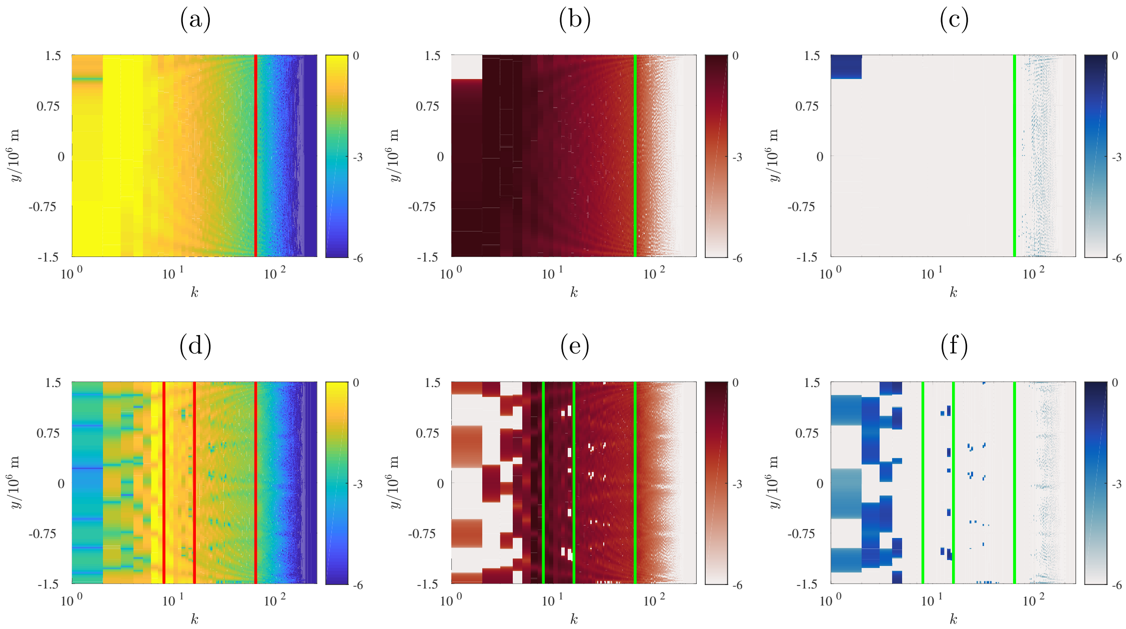

Figure 6.4.3: $K(k, y_c)$ for runs A_1 and C_1 respectively, plotted as its absolute value $|K(k, y_c)|$ (a) and (d); its positive components $K(k, y_c) > 0$ (b) and (e) and its negative components $|-K(k, y_c)| > 0$ (c) and (f), for runs A_1 (top row) and C_1 (bottom row). The solid vertical line in plots for run A_1 is k_f. From left to right, the vertical lines for run C_1 are characteristic scales k_{eq}, k_β and k_f.

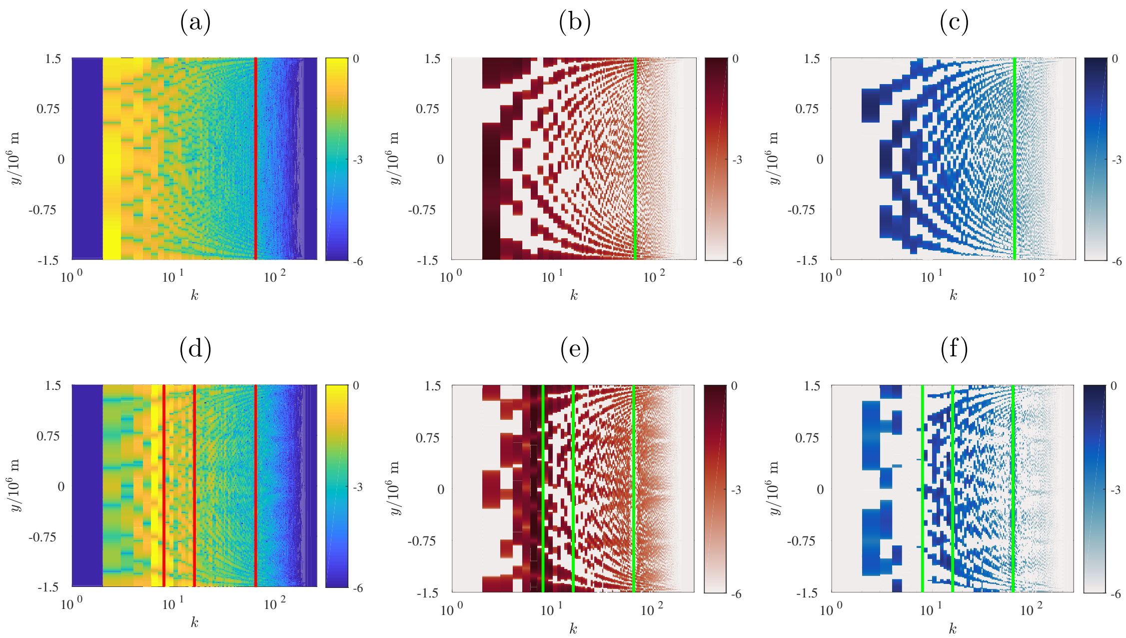

Figure 6.4.4: $M(k, y_c)$ for runs A_1 and C_1 respectively, plotted as its absolute value $|M(k, y_c)|$ (a) and (d); its positive components $M(k, y_c) > 0$ (b) and (e) and, its negative components $|-M(k, y_c)| > 0$ (c) and (f), for runs A_1 (top row) and C_1 (bottom row). The solid vertical line in plots for run A_1 is k_f. From left to right, the vertical lines for run C_1 are characteristic scales k_{eq}, k_β and k_f.

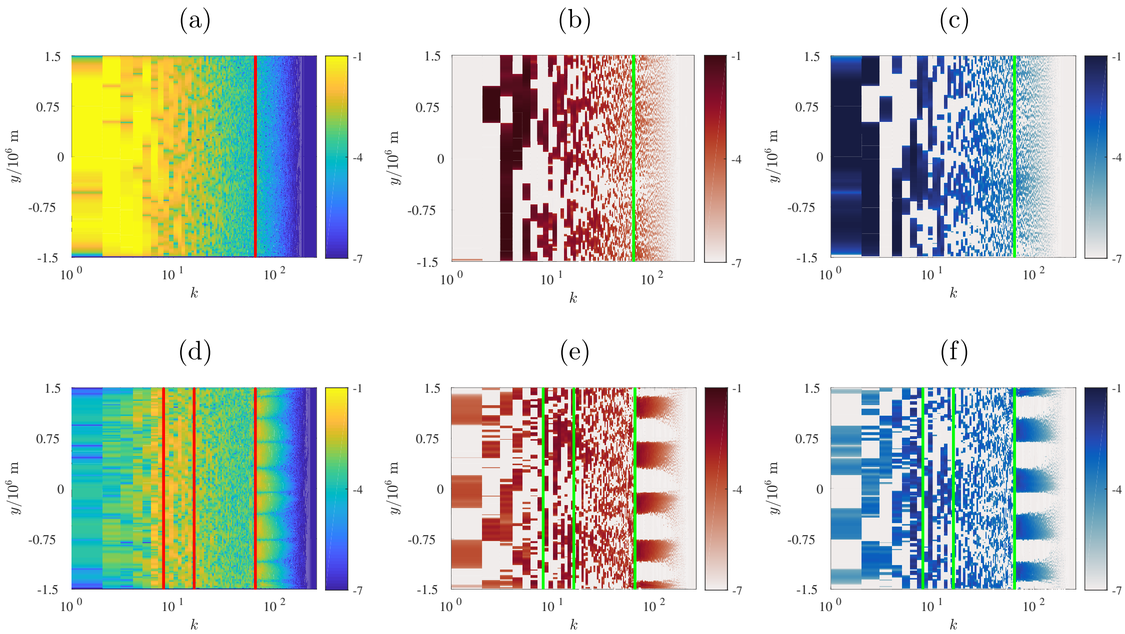

Figure 6.4.5: $N(k, y_c)$ for runs A_1 and C_1 respectively, plotted as its absolute value $|N(k, y_c)|$ (a) and (d); its positive components $N(k, y_c) > 0$ (b) and (e) and, its negative components $|-N(k, y_c)| > 0$ (c) and (f), for runs A_1 (top row) and C_1 (bottom row). The solid vertical line in plots for run A_1 is k_f. From left to right, the vertical lines for run C_1 are characteristic scales k_{eq}, k_β and k_f.

the scales responsible for supporting the jet structure. There is a low wavenumber alternating pattern in the shear stress that is not correlated with the jet structure, that may be attributed to the statistically insignificant temporal variations we have observed in the Hovmöller plots of $N(y_c)$ in §5.5. The most striking feature is a distinctive banded pattern, that alternates positive and negative, appearing at scale $k > k_f$. This signal is consistent with that observed in Fig. 6.4.1. We have noted in §5.4 that as β increases, the spike of energy at the forcing scale appears to inherent the harmonics from the Rhines spectrum. We see this in $E'(k_x, k_y)$ plotted in Fig. 6.4.2 as the forcing scale appearing smear in the k_y-direction. Since we know that these harmonics are associated with the jet spectrum, it is conceivable then that these forcing scale harmonics will demonstrate a correlation with the jet pattern. However we have seen that the spectrum tensor formulation does not capture low wavenumbers correctly and produces negative energy densities in these ranges. Though it is unclear what the origin of the small-scale signal in Fig. 6.4.5 is, it is useful to demonstrate power of this tool to filter at different radial scales and extract geometric eddy ellipse information. In Fig. 5.5.4 we saw that a high-pass zonal filter allowed us to calculate a tilt angle that is consistent with the jet structure.

In Fig. 6.4.6 we calculate the eddy ellipse tilt angle associated with eddy velocity

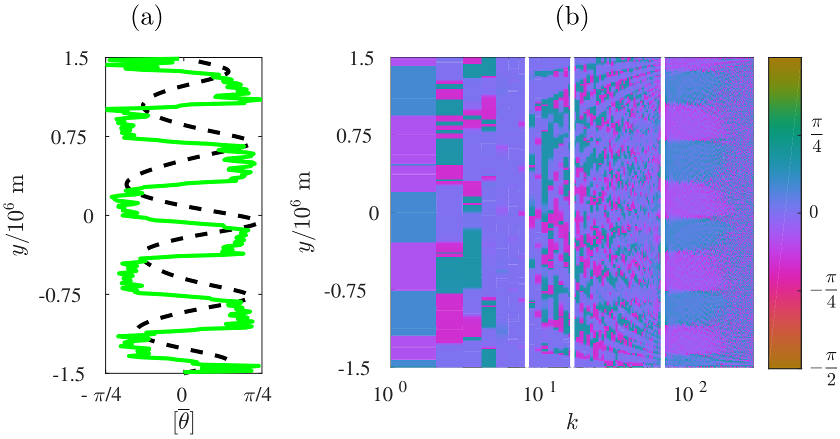

Figure 6.4.6: $[\theta(k, y_c)]$ (solid green) (a) calculated using a high-pass radial filter retaining wavenumbers $k = 50 - 85$ for run A_1 averaged over a 20,000 hrs equilibration period. The shape of $[\overline{u}]$ (dotted black) is included for comparison. The tilt angle spectrum $\theta(k, y_c)$ (b) calculated using Eq. (6.3.14). The vertical white solid lines, from left to right, are characteristic scales k_{eq}, k_β and k_f respectively.

correlations between $k = 50 - 85$, where the shear-stress demonstrates a pattern that correlates with the zonal structure. These tilts have the correct sign, however they do not show the fine structure that we observed using the zonal filter, of a saw-tooth pattern that produces a sharp eastward, broad westward jet pattern. We also include the full spectrum of $\theta(k, y_c)$ calculated using Eq. (6.3.14) which in addition to the high-wavenumber signal, demonstrates some a low-wavenumber tilting patterns that could be associated with the low-wavenumber time-dependent processes we have observed when using a low-pass zonal filter in §5.5.

6.5 Conclusion

We have developed a formulation for calculating the inhomogeneous analogue of the spectrum tensor, the latter of which is widely used in the study of two-dimensional turbulence. We have provided its decomposition on angular modes to describe the anisotropy in the spectra following Herring (1975). We have found that the anisotropic decomposition can be used to extract information about the Reynolds stresses directly from the energy spectrum. The energy spectrum is composed of a superposition of an infinite number of even angular modes but only the f_0 and f_2 components survive when calculating single point statistics. The f_0 component provides information about all the velocity correlations as a function of scale that contribute to the total energy. The f_2 component contains information about all the velocity correlations, as a function of scale, that contribute to the eddy stress tensor quantities M and N, given by the real and imaginary parts of f_2 respectively.

We have seen some results using this formulation. We see a strong signal in the enstrophy cascade of the shear stress spectrum however we suspect that this is not providing the correct correlations as function of scale because the inhomogeneous energy spectrum we have calculated does not obey the symmetry properties Eq. (6.2.12). This leads to there being parts of the inhomogeneous energy spectrum that are negative. We expect that the low-wavenumbers are mostly affected because we have derived the inhomogeneous spectrum tensor assuming periodicity in x and y whereas our domain is bounded in y. We have circumvented this issue using the equivalence between a Fourier transform on periodic domains and sine or cosine transforms on bounded domains however we have not considered how even or odd symmetries in y are reflected in the symmetries of the spectrum tensor. This may be the source of the low-wavenumber negative energies. Deriving the inhomogeneous spectrum tensor, considering the symmetries imposed by thesis a subject of future work.

Whilst we have been unable to calculate $E\left(y_c, k_x, k_y\right)$ directly for this thesis, we have still been able to better understand the connection between the eddy stress tensor quantities $M\left(y\right)$ and $N\left(y\right)$ and their relationship with the energy spectrum. One important point is that the eddies close to the Rhines spectrum cannot be the eddies responsible for supporting the jet structure since the Rhines spectrum develops along the zonal axis. The imaginary part of the f_2 component, we have seen, is weighted towards the diagonal regions of the energy spectrum. These regions of the energy spectrum are far less energetic.

7

Conclusions and Future Work

The broad aim of this thesis has been to understand the role of eddy momentum fluxes in creating and maintaining jets that are associated with geostrophic turbulence. Using a zonal filter we have seen that eddy fields of equilibrium jets are dominated by large-scale eddies that give rise to large momentum fluxes. These momentum fluxes are statistically insignificant over longer time-periods and mask the underlying momentum fluxes from intermediate scales, which are responsible for supporting the jet structures. We have calculated the eddy ellipse tilts associated with the intermediate-scale momentum fluxes and shown that they correlate well with the jet structures. We have further have developed a tool with which to filter velocity correlations by radial wavenumber. In this chapter we will broadly discuss extensions that could be made to the work presented and summarise the findings of each chapter.

7.1 Exploration of the Parameter Space

The advantage of using a simple model in these studies is the ability to finely tune parameters. We have employed a stochastic forcing term that allows us to choose the energy injection rate *a priori* and predict the characteristic scales associated with jet formation in geostrophic turbulence. In two-dimensional isotropic turbulence, the 512×257 grids points we have used are sufficient to resolve the important scales of motion and to allow the inertial ranges to develop over several decades of wavenumbers. In geostrophic turbulence, the picture is far more complicated where there are several important characteristic scales that should ideally be well separated according to the inequality given by Eq. (5.4.6). However we note that flows in nature often do not demonstrate a good scale-separation, but studying flows which do provides a simplified situation to help develop a better understanding. Flows with well separated anisotropic wavenumber k_β and equilibrium wavenumber k_{eq} will develop several harmonics along the Rhines spectrum. This produces the rich superposition of harmonics necessary to obtain the idealised sharpened eastward jets and broad westward jet pattern. There must also be a sufficient number of cascade steps in the isotropic portion of the flow field between the forcing scale k_f and k_β to avoid the forcing scale acquiring harmonics from the Rhines spectrum. Also, the final destination of the energy front at k_{eq} should not be influenced by the domain scale. With all these considerations, there is a very little room in the parameter space for ideal jets to form. In §5 we presented results from eight model runs of β-plane turbulence, with different rotation rates, four of which were equilibrated under Rayleigh friction. Only one of our equilibriated runs had demonstrated a good scale separation and so our subsequent analysis using the geometric eddy ellipse decomposition had been limited to only this simulation. Since we are interested in the role of these characteristic scales in the arrangement of eddy momentum fluxes, it is important to conduct a wider exploration of the parameter space. These studies would benefit greatly then from using a domain with higher resolution to resolve the important scales of motion.

In §5 we have found that the scale-selective biharmonic diffusion does not remove energy sharply at the smallest scales and removes significant amounts of energy at the forcing scale. This has lead to some differences between the characteristic scales predicted and those which are observed. These systems would benefit from more scale-selective, higher-order diffusions such as the $\nabla^{16}\zeta$ hyperviscosity term used by Chekhlov et al. (1996).

The calculation of the biharmonic in finite differences suffers a heavy loss in precision when compared to using spectral methods for the same number of grid points. Increasing the order of the diffusion would lead to a heavier loss of precision and would render the use of finite differences for this calculation untennable. Unfortunately, the use of mixed boundary conditions precludes the employment of a conventional pseudo-spectral method. This is because the non-linear terms in the barotropic vorticity equation would produce zonal modes that require an infinite number of basis functions to be represented. This would lead to Gibbs phenomena (Vallis, 1985). Dirichlet boundary conditions however present no such restriction as they may be solved pseudo-spectrally without introducing modes that cannot be represented using a finite Fourier series. A future exploration of the parameter space would benefit then from employing Dirichlet boundary conditions, using pseudo-spectral methods and a high-order hyperviscosity for sharp, small scale energy dissipation.

An outstanding question from this thesis and previous works (Huang and Robinson, 1998) is the role of the dominant, short frequency momentum fluxes that are produced by eddies near the Rhines scale. One way to elucidate their role would be understanding how different eddy scales flux momentum during jet formation.

A more realistic scenario in which to study jet formation in geostrophic turbulence is using a baroclinic model with multiple layers. Literature on these models demonstrate some basic observations from barotropic theory, such as meridional scaling of jets with the Rhines scale and that jets are supported by a divergence of momentum flux rather than buoyancy fluxes (Berloff et al., 2009a; Panetta, 1993). In these models eddies are generated by baroclinic instability rather than parameterised using stochastic forcing as we have done in the present work. We have seen that using stochastic forcing allows us to control characteristic flow scales. It would be interesting to see if these characteristic scales are important in the formation of zonal jets in baroclinically unstable systems.

7.2 Thesis Summary

In §2 we developed a mathematical model for the barotropic vorticity equation on a periodic, laterally bounded channel given by Eq. (2.2.1) that would form the basis of our numerical experiments. We examined this model for two sets of commonly employed boundary conditions that lead to unique solutions. We found that the application of Dirichlet boundary conditions on ζ leads to momentum conservation but in most domain geometries, a consistency condition must be solved to ensure that Eq. (2.2.1) is consistent with the shallow water momentum equations, from which they are derived. We found that for a channel model, this condition is automatically satisfied by imposing mass conservation given by Eq. (2.1.53). Another commonly employed set of conditions are a mixture of Neumann boundary conditions on the zonal mean modes $\overline{\zeta}$ and Dirichlet conditions on the non-mean modes ζ'. These conserve circulation and automatically satisfy the consistency relation. These are the boundary conditions we have employed for the numerical studies we have pursued in this thesis. We presented the numerical discretisation of the model in §3 in which the model was marched in time using a leapfrog algorithm and derivatives were calculated using finite differences and we used a mixure of finite differences and spectral methods for inverting the streamfunction.

In §4 we introduced a formulation with which to visualise eddy velocity correlations as variance ellipses and applied this forumation to shear instabilities on a zonal jet, following analysis presented in Tamarin et al. (2016). When we ran the model allowing for more turbulent dynamics, we were able to filter the eddy velocities and obtain the most unstable mode. We were then able to recover the eddy ellipses distributions that correlated with the first jet weakening event.

In §5 we examined jet formation in geostrophic turbulence from a number of complimentary perspectives. We saw how jets develop into persistent structures, with sharp eastward and broad westward components that coincide with strong and weak PV-gradients respectively (Dritschel and McIntyre, 2008). We understood jet formation in terms of the propagation of a time-dependent energy front in wavenumber space k_{min}. For flows reaching steady-state, jets formed in a region between k_β, the anisotropy wavenumber (Maltrud and Vallis, 1991; Sukoriansky et al., 2007) and $k_{\mathrm{eq}} \equiv k_R$, the final position of the energy front along the steep Rhines spectrum. We then sought to apply the geometric eddy ellipse formulation introduced in §4 to spontaneous jet formation in geostrophic turbulence. We found that Hövmoller plots of the shear stress were dominated by a streaking, time-dependent pattern. A time average over this revealed an underlying pattern that correlated with the jet structure. We filtered the eddy velocities at low pass and high pass to separate low and intermediate wavenumber contributions to the the eddy stress quantities $M(y)$ and $N(y)$. In doing so, we were able to visualise the underlying, regular momentum flux patterns that support the jets. The eddy tilt angle of the eddy ellipse associated with the high-pass filter revealed a saw-tooth patten that correlated with the sharp eastward and broad westward jet pattern.

Our analysis in §5, did not reveal an obvious link between the characteristic scales in the energy spectra and the scales we needed to filter to reveal the underlying eddy tilt pattern. Though broadly, we found that the less energetic scales, in which $k > k_\beta$, contained this signal. We reasoned that since the eddy stresses $N(y)$ and $M(y)$ are meridionally inhomogeneous, we need to find the inhomogeneous analogue of the 2D energy spectrum $E(k_x, k_y)$. In §6, we developed a formulation with which to calculate terms of an inhomogeneous spectrum tensor. We found that we only needed to calculate the inhomogeneous energy spectrum to recover the other tensor components. Following an angular decomposition introduced by Herring (1975), we found that the angular mean component f_0 contained all the velocity correlations that give the meridional distribution of eddy energy $K(y)$. We found that the f_2 component contained all the velocity correlations that gave the Reynolds stresses $M(y)$ and $N(y)$, given by the real and imaginary parts of f_2 respectively. We derived the inhomogeneous energy spectrum assuming a doubly periodic domain. We need to revisit this formulation considering symmetries imposed by the lateral boundaries. Without these considerations, our analysis reveals some spurious results such as negative energy and a momentum flux signal in the enstrophy cascade of the shear stress. Resolving problems with calculating the inhomogeneous energy spectrum is a subject of future work. If these issues can be resolved, this will be useful tool for studying eddy-mean flow interactions in turbulent systems.

Bibliography

Basdevant, C., Legras, B., Sadourny, R., and Béland, M. (1981). A study of barotropic model flows: Intermittency, waves and predictability. *Journal of the Atmospheric Sciences*, 38(11):2305–2326.

Batchelor, G. K. (1953). *The Theory of Homogeneous Turbulence*. Cambridge Univ Press.

Batchelor, G. K. (1969). Computation of the energy spectrum in homogeneous two-dimensional turbulence. *Physics of Fluids (1958-1988)*, 12(12):II–233.

Berloff, P. (2005). On rectification of randomly forced flows. *J. Mar. Res.*, 63:497–527.

Berloff, P., Kamenkovich, I., and Pedlosky, J. (2009a). A mechanism of formation of multiple zonal jets in the oceans. *Journal of Fluid Mechanics*, 628:395–425.

Berloff, P., Kamenkovich, I., and Pedlosky, J. (2009b). A model of multiple zonal jets in the oceans: Dynamical and kinematical analysis. *Journal of Physical Oceanography*, 39(11):2711–2734.

Boffetta, G. and Ecke, R. E. (2012). Two-dimensional turbulence. *Annual Review of Fluid Mechanics*, 44(1):427–451.

Brachet, M., Meneguzzi, M., Politano, H., and Sulem, P. (1988). The dynamics of freely decaying two-dimensional turbulence. *Journal of Fluid Mechanics*, 194:333–349.

Bretherton, F. P. (1966). Critical layer instability in baroclinic flows. *Quarterly Journal of the Royal Meteorological Society*, 92(393):325–334.

Charney, J. G. (1971). Geostrophic turbulence. *Journal of the Atmospheric Sciences*, 28:1087.

Chekhlov, A., Orszag, S. A., Sukoriansky, S., Galperin, B., and Staroselsky, I. (1996). The effect of small-scale forcing on large-scale structures in two-dimensional flows. *Physica D: Nonlinear Phenomena*, 98(2):321–334.

Choi, D. S. and Showman, A. P. (2011). Power spectral analysis of jupiter's clouds and kinetic energy from cassini. *Icarus*, 216(2):597 – 609.

Cravatte, S., Kessler, W. S., and Marin, F. (2012). Intermediate zonal jets in the tropical pacific ocean observed by argo floats. *Journal of Physical Oceanography*, 42(9):1475–1485.

Cushman-Roisin, B. and Beckers, J.-M. (2011). *Introduction to Geophysical Fluid Dynamics*, volume 101. Elsevier, 2nd edition.

Danilov, S. and Gurarie, D. (2004). Scaling, spectra and zonal jets in beta-plane turbulence. *Physics of Fluids*, 16(7):2592–2603.

Davidson, P. A. (2004). *Two-dimensional turbulence*, volume 1, chapter 10, pages 569–617. Oxford University Press, USA.

Dritschel, D. and McIntyre, M. (2008). Multiple jets as pv staircases: the phillips effect and the resilience of eddy-transport barriers. *Journal of the Atmospheric Sciences*, 65(3):855–874.

Eden, C. (2010). Parameterising meso-scale eddy momentum fluxes based on potential vorticity mixing and a gauge term. *Ocean Modelling*, 32(1):58 – 71. The magic of modelling: A special volume commemorating the contributions of Peter D. Killworth - Part I.

Esler, J. G. (2008). The turbulent equilibration of an unstable baroclinic jet. *Journal of Fluid Mechanics*, 599:241–268.

Farrell, B. F. and Ioannou, P. J. (2009). Emergence of jets from turbulence in the shallow-water equations on an equatorial beta plane. *Journal of the Atmospheric Sciences*, 66(10):3197–3207.

Fjørtoft, R. (1953). On the changes in the spectral distribution of kinetic energy for twodimensional, nondivergent flow. *Tellus A*, 5(3).

Galperin, B., Sukoriansky, S., Dikovskaya, N., Read, P. L., Yamazaki, Y. H., and Wordsworth, R. (2006). Anisotropic turbulence and zonal jets in rotating flows with a β-effect. *Nonlinear Processes in Geophysics*, 13(1):83–98.

Galperin, B., Sukoriansky, S., and Huang, H.-P. (2001). Universal n^5 spectrum of zonal flows on giant planets. *Physics of Fluids*, 13(6):1545–1548.

Galperin, B., Young, R. M., Sukoriansky, S., Dikovskaya, N., Read, P. L., Lancaster, A. J., and Armstrong, D. (2014). Cassini observations reveal a regime of zonostrophic macroturbulence on jupiter. *Icarus*, 229:295 – 320.

Gent, P. R. and Mcwilliams, J. C. (1990). Isopycnal mixing in ocean circulation models. *Journal of Physical Oceanography*, 20(1):150–155.

Graef, F. and Müller, P. (1996). Uniqueness of solutions and conservation laws for the quasigeostrophic model. *Dynamics of Atmospheres and Oceans*, 25(2):109 – 132.

Griffies, S. M. and Hallberg, R. W. (2000). Biharmonic friction with a smagorinsky-like viscosity for use in large-scale eddy-permitting ocean models. *Monthly Weather Review*, 128(8):2935–2946.

Hallberg, R. and Gnanadesikan, A. (2006). The role of eddies in determining the structure and response of the wind-driven southern hemisphere overturning: Results from the modeling eddies in the southern ocean (meso) project. *Journal of Physical Oceanography*, 36(12):2232–2252.

Heifetz, E., Bishop, C. H., and Alpert, P. (1999). Counter-propagating rossby waves in the barotropic rayleigh model of shear instability. *Quarterly Journal of the Royal Meteorological Society*, 125(560):2835–2853.

Herring, J. (1975). Theory of two-dimensional anisotropic turbulence. *Journal of the Atmospheric Sciences*, 32(12):2254–2271.

Holloway, G. and Hendershott, M. C. (1977). Stochastic closure for nonlinear rossby waves. *Journal of Fluid Mechanics*, 82:747–765.

Hoskins, B. J., James, I. N., and White, G. H. (1983). The shape, propagation and mean-flow interaction of large-scale weather systems. *Journal of the Atmospheric Sciences*, 40(7):1595–1612.

Huang, H.-P., Galperin, B., and Sukoriansky, S. (2001). Anisotropic spectra in two-dimensional turbulence on the surface of a rotating sphere. *Physics of Fluids (1994-present)*, 13(1):225–240.

Huang, H.-P. and Robinson, W. A. (1998). Two-dimensional turbulence and persistent zonal jets in a global barotropic model. *Journal of the atmospheric sciences*, 55(4):611–632.

Kolmogorov, A. (1941). The Local Structure of Turbulence in Incompressible Viscous Fluid for Very Large Reynolds' Numbers. *Akademiia Nauk SSSR Doklady*, 30:301–305.

Kraichnan, R. H. (1967). Inertial Ranges in Two-Dimensional Turbulence. *Physics of Fluids*, 10:1417–1423.

Kraichnan, R. H. (1971). Inertial-range transfer in two- and three-dimensional turbulence. *Journal of Fluid Mechanics*, 47(3):525–535.

Kramer, W., van Buren, M. G., Clercx, H. J. H., and van Heijst, G. J. F. (2006). -plane turbulence in a basin with no-slip boundaries. *Physics of Fluids*, 18(2):026603.

Lee, A. I. and Hill, J. M. (1983). On the solution of boundary value problems for fourth order diffusion. *Acta Mechanica*, 46(1):23–35.

Lilly, D. K. (1969). Numerical simulation of two-dimensional turbulence. *The Physics of Fluids*, 12(12):II–240–II–249.

Maddison, J. R. and Marshall, D. P. (2013). The eliassen–palm flux tensor. *Journal of Fluid Mechanics*, 729:69–102.

Maltrud, M. and Vallis, G. (1991). Energy spectra and coherent structures in forced two-dimensional and beta-plane turbulence. *Journal of Fluid Mechanics*, 228:321–342.

Marshall, D. P., Maddison, J. R., and Berloff, P. S. (2012). A framework for parameterizing eddy potential vorticity fluxes. *Journal of Physical Oceanography*, 42(4):539–557.

Marshall, J., Shuckburgh, E., Jones, H., and Hill, C. (2006). Estimates and implications of surface eddy diffusivity in the southern ocean derived from tracer transport. *Journal of Physical Oceanography*, 36(9):1806–1821.

Maximenko, N. A., Bang, B., and Sasaki, H. (2005). Observational evidence of alternating zonal jets in the world ocean. *Geophysical Research Letters*, 32(12).

McWilliams, J. C. (1977). A note on a consistent quasigeostrophic model in a multiply connected domain. *Dynamics of Atmospheres and Oceans*, 1(5):427 – 441.

McWilliams, J. C. (1984). The emergence of isolated coherent vortices in turbulent flow. *Journal of Fluid Mechanics*, 146:21–43.

Milliff, R. F. and McWilliams, J. C. (1994). The evolution of boundary pressure in ocean basins. *Journal of Physical Oceanography*, 24(6):1317–1338.

Nadiga, B. and Straub, D. (2010). Alternating zonal jets and energy fluxes in barotropic wind-driven gyres. *Ocean Modelling*, 33(3–4):257–269.

Nadiga, B. T. (2006). On zonal jets in oceans. *Geophysical research letters*, 33(10).

Nakano, H. and Hasumi, H. (2005). A series of zonal jets embedded in the broad zonal flows in the pacific obtained in eddy-permitting ocean general circulation models. *Journal of Physical Oceanography*, 35(4):474–488.

NASA, JPL-Caltech, SwRI, and MSSS (2017). Jupiter's stunning southern hemisphere. https://www.jpl.nasa.gov/spaceimages/details.php?id=PIA21970. Accessed: 09-05-2019.

Nastrom, G. D. and Gage, K. S. (1983). A first look at wavenumber spectra from gasp data. *Tellus A*, 35A(5):383–388.

Panetta, R. L. (1993). Zonal jets in wide baroclinically unstable regions: Persistence and scale selection. *Journal of the atmospheric sciences*, 50(14):2073–2106.

Pedlosky, J. (1987a). *Geophysical fluid dynamics*. Springer, second edition.

Pedlosky, J. (1987b). *Inviscid Shallow Water Theory*, chapter 3, pages 65–67. In Pedlosky (1987a), second edition.

Plumb, R. A. (1986). Three-dimensional propagation of transient quasi-geostrophic eddies and its relationship with the eddy forcing of the time—mean flow. *Journal of the Atmospheric Sciences*, 43(16):1657–1678.

Preisendorfer, R. W. (1988). *Principle Component Analysis in Meteorology and Oceanography*, volume 17. Elsevier.

Proudman, J. and Lamb, H. (1916). On the motion of solids in a liquid possessing vorticity. *Proceedings of the Royal Society of London. Series A, Containing Papers of a Mathematical and Physical Character*, 92(642):408–424.

Reynolds, O. (1895). Iv. on the dynamical theory of incompressible viscous fluids and the determination of the criterion. *Philosophical Transactions of the Royal Society of London A: Mathematical, Physical and Engineering Sciences*, 186:123–164.

Rhines, P. B. (1975). Waves and turbulence on a beta-plane. *Journal of Fluid Mechanics*, 69:417–443.

Rhines, P. B. (1994). Jets. *Chaos: An Interdisciplinary Journal of Nonlinear Science*, 4(2):313–339.

Rintoul, S. R. (2018). The global influence of localized dynamics in the southern ocean. *Nature*, 558(7709):209–218.

Rintoul, S. R. and Garabato, A. C. N. (2013). *Dynamics of the Southern Ocean Circulation*, volume 103, chapter 18, pages 471–518. Academic Press, Oxford, UK, 2 edition.

Salmon, R. (1980). Baroclinic instability and geostrophic turbulence. *Geophysical & Astrophysical Fluid Dynamics*, 15(1):167–211.

Salmon, R. (1998a). *Lectures on geophysical fluid dynamics*, volume 1. Oxford University Press, Oxford.

Salmon, R. (1998b). *Vorticity and Turbulence*, chapter 4, pages 197–231. Volume 1 of Salmon (1998a).

Scott, R. and Dritschel, D. (2013). Halting scale and energy equilibration in two-dimensional quasigeostrophic turbulence. *Journal of Fluid Mechanics*, 721:R4–1.

Scott, R. B. and Wang, F. (2005). Direct evidence of an oceanic inverse kinetic energy cascade from satellite altimetry. *Journal of Physical Oceanography*, 35(9):1650–1666.

Shepherd, T. G. (1987a). Rossby waves and two-dimensional turbulence in a large-scale zonal jet. *Journal of Fluid Mechanics*, 183:467–509.

Shepherd, T. G. (1987b). A spectral view of nonlinear fluxes and stationary-transient interaction in the atmosphere. *Journal of the Atmospheric Sciences*, 44(8):1166–1179.

Starr, V. P. (1968). *Physics of Negative Viscosity Phenomena*. McGraw-Hill, New York, 1st edition.

Sukoriansky, S., Dikovskaya, N., and Galperin, B. (2007). On the arrest of inverse energy cascade and the rhines scale. *Journal of the Atmospheric Sciences*, 64(9):3312–3327.

Sukoriansky, S., Dikovskaya, N., and Galperin, B. (2008). Nonlinear waves in zonostrophic turbulence. *Physical review letters*, 101 17:178501.

Sukoriansky, S. and Galperin, B. (2005). *Subgrid- and supergrid-scale parameterization of turbulence in quasi-two-dimensional barotropic flows and the* *phenomenon of negative viscosity*, chapter 55, page 445. Cambridge University Press, 1st edition.

Sukoriansky, S., Galperin, B., and Dikovskaya, N. (2002). Universal spectrum of two-dimensional turbulence on a rotating sphere and some basic features of atmospheric circulation on giant planets. *Phys. Rev. Lett.*, 89:124501.

Tamarin, T., Maddison, J. R., Heifetz, E., and Marshall, D. P. (2016). A geometric interpretation of eddy reynolds stresses in barotropic ocean jets. *Journal of Physical Oceanography*, 46(8):2285–2307.

Taylor, G. I. (1915). I. eddy motion in the atmosphere. *Philosophical Transactions of the Royal Society of London A: Mathematical, Physical and Engineering Sciences*, 215(523-537):1–26.

Taylor, G. I. (1923). Experiments on the motion of solid bodies in rotating fluids. *Proceedings of the Royal Society of London. Series A, Containing Papers of a Mathematical and Physical Character*, 104(725):213–218.

Thompson, A. F. (2008). The atmospheric ocean: eddies and jets in the antarctic circumpolar current. *Philosophical Transactions of the Royal Society of London A: Mathematical, Physical and Engineering Sciences*, 366(1885):4529–4541.

Thompson, A. F. and Young, W. R. (2007). Two-layer baroclinic eddy heat fluxes: Zonal flows and energy balance. *Journal of the Atmospheric Sciences*, 64(9):3214–3231.

Tran, C. V. and Bowman, J. C. (2003). On the dual cascade in two-dimensional turbulence. *Physica D: Nonlinear Phenomena*, 176(3):242 – 255.

Treguier, A. M., Hogg, N. G., Maltrud, M., Speer, K., and Thierry, V. (2003). The origin of deep zonal flows in the brazil basin. *Journal of Physical Oceanography*, 33(3):580–599.

Treguier, A. M. and Panetta, R. L. (1994). Multiple zonal jets in a quasigeostrophic model of the antarctic circumpolar current. *Journal of Physical Oceanography*, 24(11):2263–2277.

Vallis, G. K. (1985). On the spectral integration of the quasi-geostrophic equations for doubly-periodic and channel flow. *Journal of the Atmospheric Sciences*, 42(1):95–99.

Vallis, G. K. and Maltrud, M. E. (1993). Generation of mean flows and jets on a beta plane and over topography. *Journal of physical oceanography*, 23:1346–1346.

Wardle, R. and Marshall, J. (2000). Representation of eddies in primitive equation models by a pv flux. *Journal of Physical Oceanography*, 30(10):2481–2503.

Waterman, S. and Hoskins, B. J. (2013). Eddy shape, orientation, propagation, and mean flow feedback in western boundary current jets. *Journal of Physical Oceanography*, 43(8):1666–1690.

Waterman, S. and Lilly, J. M. (2015). Geometric decomposition of eddy feedbacks in barotropic systems. *Journal of Physical Oceanography*, 45(4):1009–1024.

Wilkin, J. and Morrow, R. (1994). Eddy kinetic energy and momentum flux in the southern ocean: Comparison of a global eddy-resolving model with altimeter, drifter, and current-meter data. *Journal of Geophysical Research: Oceans*, 99:7903–7916.

Williams, G. (1978). Planetary circulations: 1. barotropic representation of jovian and terrestrial turbulence. *J. Atmos. Sci.; (United States)*, 35.

Williams, P. D., Haine, T. W. N., Read, P. L., Lewis, S. R., and Yamazaki, Y. H. (2009). Quagmire v1.3: a quasi-geostrophic model for investigating rotating fluids experiments. *Geoscientific Model Development*, 2(1):13–32.